2022

A Flexible 3D Architecture for Cooling Future Generation Devices

Khan Mohammad Rabbi
University of Central Florida, khan.rabbi@Knights.ucf.edu

A FLEXIBLE 3D ARCHITECTURE FOR COOLING FUTURE GENERATION DEVICES

by

KHAN MOHAMMAD RABBI
B.S., Bangladesh University of Engineering and Technology, 2016

A dissertation submitted in partial fulfilment of the requirements
for the degree of Doctor of Philosophy
in the Department of Mechanical and Aerospace Engineering
in the College of Engineering and Computer Science
at the University of Central Florida
Orlando, Florida

Summer Term
2022

Major Professor: Shawn A. Putnam

ABSTRACT

Systems that consume and convert energy produce thermal energy as a byproduct. This generation of thermal energy, if not dissipated properly, contributes to the significant temperature rise of the overall system. This temperature rise can lead to reduced efficiency and system-level failure. Future technologies will continue to face such thermal challenges. In fact, next-gen devices will demand flexible thermal management architectures for high-performance operation. To tackle these challenges, innovative liquid cooling technologies and high-speed thermal diagnostic systems must be developed simultaneously.

Active and passive pulsation-liquid-cooling techniques are currently an attractive thermal management solution. In an active cooling mode, the influence of pulsation on heat transfer enhancement using liquid jets is understood, fairly well both theoretically and experimentally. However, the thermal diagnostic systems for characterizing these cooling methods fall short for many reasons including that the conventional thermal cameras have limited temporal and spatial resolutions. To solve this problem and capture high thermal transients, a low-cost thermal mapping technique using Quantum-dots is developed. In parallel to active cooling solutions, passive cooling technologies have come a long way due to their capability of hot spot mitigation. However, challenges remain in thermal diagnostics and the fabrication methodologies – especially for the next-gen of flexible and 3D electronic packages. To solve these problems, firstly, research efforts are pursued to come up with i) a fabrication process that is easy, cheap and repeatable and ii) an innovative design with modular features that makes it suitable for double-sided cooling configuration. Secondly, experimental testing is pursued to reveal the flow and thermal kinetics for different condensation conditions. This work identified many design, fabrication, and thermal performance limitations tied to planar, flexible and stacked-3D pulsating heat pipes that can also incorporate multi-phase coolants such as the combination of paraffin wax and water-ethanol fluid mixtures.

To my baby boy, Khan Mohammad Razeen

ACKNOWLEDGMENTS

This completion has become possible because Almighty Allah has always been on my side. He tested my patience; I always thought better days would come if I strongly believed in Him. I feel blessed since Allah listened to all my prayers and words of faith. I will pray even harder now to be an even better Muslim and practice Islam in every aspect of my life.

I acknowledge the consistent support my wife (Dr. Tafannum Noshin) and my parents (Mr. Khan Mohammad Rafee and Mrs. Fahmida Afrin) provided in these years. Thank you Baba, Maa, for always putting education first. Baba, you left the precious governmental job to ensure I could move to the capital of Bangladesh, Dhaka, from a remote southern part of the country. You made sure I got the highest quality of education. All those sleepless nights that you two spent beside me so that I could study well and felt confident about every exam I had ever taken through high school education. All those tiny little steps have resulted in this. I always pray to Allah that He blesses you and Maa with sound health. I also wish my paternal uncle (Boro Chacha), Prof. Khan Towhid Osman, Ph.D. could live a little longer to see another Ph.D. in the family, the sixth one. May Allah grant him Jannah. This Ph.D. would not be a Ph.D. if my beautiful wife Tafannum Noshin is not there beside me. I got frustrated, depressed, and tired at times, but Noshin, you are always there, providing me with the bigger picture and teaching me to chin up to do what I is supposed to do. I never had to worry about what would be my next meal as it is always ready. You are a life partner, a friend, a mentor. May Allah ease the path for you and give you everything you cherish in your life. You showed great courage and patience all the time. Leaving your extended family behind and leaving a long-cherished Dentist position back in Bangladesh showed how sacrificing you were. Given my very little income through financial stipends, you always prioritize the needs but not the wants. However, you made this choice because of me, because of us. You gave me the greatest gift, a boy, my beloved papa, Khan Mohammad Razeen, and all this in the middle of

the COVID-19 pandemic. When you gave birth to our beloved son with such excruciating pain while wearing the mask, I immediately realized that nothing could beat the level of sacrifices you had made for our family. I also want to thank my brother, Shohan, for always being my partner-in-crime. Being raised alongside you is a privilege as I got the chance to follow you. May Allah keep you safe and sound. I thank my father-in-law Mr. Mobinul Islam Mollah, my mother-in-law Mrs. Nazmun Naher, and my brother Mobashir Zahin for always encouraging us through my Ph.D. journey. Thank you, Nanu (Mrs. Alam Ara Khan) for always keeping me in your prayers.

I acknowledge the constant support and supervision that my Ph.D. advisor Prof. Shawn A. Putnam, Ph.D. gave me over the years. The most important thing, in my opinion, a Ph.D. supervisor can give to his/her graduate student is to put trust in them. Thank you, Dr. Putnam, for keeping faith in me and giving me the freedom and opportunity to conduct research in the cutting-edge research laboratory. Thank you for criticizing me at times which helped me reach my goal and helped me grasp the underlying mechanism and think about the scientific rationale behind every problem I faced in the laboratory. You mentored me with great care that shaped me professionally and personally. I wish the best for you and your family.

I want to thank my extraordinary colleagues of Interfacial Transport Laboratory at UCF, especially, Tanvir Ahmed Chowdhury, Ph.D., Thomas Germain, Ph.D., Chance Brewer, Nicholas Morgan, Damian Hundley, Fernando Sopriano, Christopher Borden, Jake Carter, Juan Sanchez, Jordan Bennett, Jonathan Ramirez for providing my consistent support and constructive feedback. I also want to thank Dr. Raffaele Amalfi Luca (Bell Labs), Dr. Todd Salamon (Bell Labs), Mr. Bhaskar Bhatnagar (ASML), Mr. Greg Wilson (ASML) for gracious mentorship and supervision during my internships that helped me grow professionally and personally. I also want to thank my dissertation committee members, journal editors, anonymous reviewers and judges who took the time to critique my research which led to publications in journal, conference proceedings and poster/seminar presentations.

TABLE OF CONTENTS

LIST OF FIGURES

LIST OF TABLES

CHAPTER 1: INTRODUCTION

The Problem

Heat generation is one of the major problems hindering high-performance operations of mechanical systems or electronic devices. Without efficiently mitigating the heat, the optimum operation will not be achieved, which is valid for any ground and space-based technologies. Researchers worldwide have worked tirelessly to innovate and create novel solid-state or microfluidic cooling technologies for futuristic applications. Solid-state cooling provided good thermal management, showed fundamental limits and is limited by material properties. In contrast, liquid cooling technologies are expected to revolutionize because of their high heat flux mitigation capability. It is essential because conventional air cooling technologies are falling short due to their high pumping power requirements, low Coefficient of Performance (COP), and noise generation. Moreover, the free stream (unpulsed) liquid cooling techniques also underperform because of their over-utilization of coolant and suppression of two-phase events (e.g., nucleate boiling). Also, the flexible nature of future electronic systems makes the cooling process even more challenging due to reliability concerns. Moreover, the 3D packaging technologies also demand high interfacial cooling of each layer/stack. Additionally, existing thermal diagnostic systems are failing because of their limited resolutions, which is crucial for quantifying the thermal performance of innovative pulsated liquid cooling technologies. Therefore, a novel thermal mapping technique must be developed to quantify local and average thermal performance accurately.

The Solution

A pulsated liquid cooling method (both in the active and passive domain) is proposed. Actively pulsated liquid cooling requires an external form of energy and has a specific duty cycle. For example, pulsated liquid jets are large trains of droplets and liquid slugs moving through the air that eventually impact the surface and transfer the heat from the surface. In contrast, passive pulsated cooling technology relies on interfacial forces to drag the liquid from one location to another, thus not requiring any external energy demand. High-speed thermal imaging quantifies how effectively active liquid jets and passive 3D-stacked-PHPs can cool a hot component. In parallel, the design constraints, manufacturing challenges, and fabrication methodologies are needed to be understood. Additionally, a numerical-analytical model is proposed to quantify the heat transfer contributions by nanoscale suspensions. Furthermore, a high-speed thermal diagnostic system based on the principle of Photoluminescence is proposed, which can map the thermal performance of both active (e.g., droplet impingement) and passive (e.g., wicking) cooling technologies.

Outline

In this dissertation, the solutions to these problems are proposed, discussed, and detailed from Chapters 2 to Chapter 6. An actively pulsed jet impingement cooling process and related findings are shown in Chapter 2. Specifically, jet impingement flow loop, heater/sensor fabrication, high-speed imaging, and thermal mapping, methodology, experimental conditions, uncertainty/error propagation analysis, and results related to the influence of pulsation frequency on heat transfer performance (both experimental findings and theoretical model predictions) and fundamental limit based on flow instability criteria are discussed. The development of thermal mapping technology using the principle of Photoluminescence (PL) is described in Chapter 3. The high-speed laser

scanner, micromachining, surface processing, high-speed visualization, calibration, PL spectra extraction with applications in pulsed jet impingement cooling, droplet evaporation, and hemi-wicking flow kinetics are discussed. The combined role of conduction, convection, and radiation for heat transfer enhancement in nanoparticle suspension is shown in Chapter 4. The thermal conductivity prediction via Effective Medium Theory (EMT), the thermal/convective boundary layer thickness prediction via simulations, the radiation enhancement via view factors, the sensitivity analysis and the enhancement in thermal conduction, and the heat transfer coefficient as a function of solid volume fraction of the nanoparticle are discussed. The fabrication methodologies and startup quantification of dual stack PHP assembly are illustrated in Chapter 5. The design criterion of the PHPs, fabrication, fundamental operation principles, embedded heater fabrication, testing results in terms of thermal/flow performance, design/integration challenges faced, and IR thermal transients are detailed in this chapter. All quantifiable findings are concluded, and future recommendations are made in Chapter 6.

CHAPTER 2: PULSED LIQUID JET IMPINGEMENT COOLING

This chapter is from the publication below by Rabbi, Carter, and Putnam (2020):
Khan Md Rabbi, Jake Carter, and Shawn A Putnam. Understanding pulsed jet impingement cooling by instantaneous heat flux matching at solid-liquid interfaces. Physical Review Fluids, 5(9):094003, 2020 [4].

Literature Review

Innovations in thermal management for current and future mechanical, optical, and microelectronic devices is getting extremely challenging. This is in large part a side product of the demand for efficient, high-power density devices - e.g., such tiny, powerful gadgets challenge not only on our theoretical understandings of local and highly transient heat and mass transfer, but also the conceptual design and practical implementation of a new cooling configuration.

Currently there are many different cooling technologies to manage this high-power density problem. Among them, pool boiling, microchannel flow boiling, spray cooling, and jet impingement cooling provide the best cooling performance metrics for high heat-density applications.[5, 6, 7, 8, 9] With this said – how do you get the cooling fluid in and out of nano-/micro-channels with appreciable mass fluxes? Nevertheless, among these cooling techniques, jet impingement cooling shows the best performance for cooling local hot-spots in terms of its correspondingly high heat transfer coefficient, surface temperature control, directional fluid flow-fields, and capability for cooling with reduced liquid coolant inventories.[10, 11] However, jet impingement cooling with steady and free-stream jets has several thermophysical limits for optimal heat transfer at the solid-liquid interface. For example, at high mass flow rates, liquid flooding effects can lead to cooling instabilities

and reductions in the liquid-to-vapor (phase-change) cooling efficiency – which effectively cap the overall heat transfer coefficient to lower limit values. Likewise, jet impingement cooling at lower mass flow rates can also result in heat transfer coefficient reductions due to wall dry-out (and/or critical heat flux conditions). Therefore, an intermediate and tunable flow-field regime is desired to both avoid such instabilities and enhance the overall coefficient of performance (COP) of the thermal management system. Ideally, pulsed jets with tunable flow-fields are desired – facilitating real-time thermal management control at the optimal length- and time-scales for high heat flux removal.

In recent years, many thermal engineers and scientists have been interested in the unsteady thermo-physical behavior of pulsating jets. Much of this work has been inspired by the pioneering research of [12]. For instance, [13] studied pulsed jet cooling for different heating and flow-field conditions. For small nozzle-to-surface distance (H/d $\approx$ 2), they observed that heat transfer increased if the jet pulsation frequency is high ($f_p >$ 175 Hz) and on the same order of turbulence time-scales. Moreover, using synthetic single-phase jets, [14] observed 180% heat transfer enhancement by increasing the Reynolds number (Re) from 1150 to 4180. More recently, [15] studied pulsed jets on semicircular heated surfaces with pulsation frequencies and nozzle-to-surface distance ratios ranging from 0 Hz $< f_p <$ 25 Hz and $1 < H/d < 8$, respectively. They observed that pulsed jets outperformed steady jets for $H/d > 6$. [16] numerically investigated sinusoidally pulsed jets at pulsation frequencies of 40-160 Hz finding 2-8% enhancements in the Nusselt number (Nu). Moreover, [17] experimentally measured the effects of a pulsed turbulent jet. They observed that the jet pulsation frequency had significant influence on both the size and the formation process of the turbulent vortex structures. Therein, the size and number of these vortices in the shearing layer are the key contributors to the wall heat transfer rate.

Despite the many recent advancements in pulsed jet cooling,[18, 19, 20, 21, 22, 23, 24, 25, 26] to our knowledge, so far no theoretical progress has been made for predicting the heat trans-

fer coefficient in terms of the jet pulsation frequency. This chapter reports a simple theoretical model based on instantaneous heat flux matching at the solid-liquid interface. Correspondingly, a coupled Kapitza and Rayleigh-Taylor instability prediction is used to estimate the optimum pulsation frequency of the jet. These findings are based on transient thermal mapping and flow-field visualization experiments using Infrared (IR) thermography and high-speed visible videography, respectively. Bubble growth, bubble collapse, dry-out zone formation, and re-wetting events during the jet impingement boiling process are discussed in terms of the corresponding length- and time-scales of the pulsed jet cooling process. Finally, a validation effort, between our experimental results and analytic predictions are made for subsequent predictions of the maximum heat transfer performance.

Experimental Setup

Jet Impingement Flow Loop

Fig. 2.1 shows the pulsed jet cooling apparatus used for this work. A continuous, steady jet is generated by a two-phase flow pump developed by RINI technologies.[27] A stainless-steel syringe needle (D_{jet} = 406 μm) is used to generate the steady jet stream. This steady jet is then mechanically chopped with a rotating filter wheel - facilitating jet pulsation frequencies and jet duty-cycles ranging from 3-410 Hz and 20-100%, respectively (please see the Supplementary Material for the details). The spray/jet chamber houses an adjustable sample holder for electrical connections, sealing, and flow-loop connectors. The jet chamber can be moved relative to the jet nozzle and chopper wheel assembly to adjust both jet impingement point and the relative distance between jet source and the heated sample surface (e.g., H). This study focused on small diameter, low frequency pulsed jets (7-25 Hz) at 50% duty-cycle and mass flux of G =795 kg/m^{2}s - corresponding to $H/D \approx 195$, Re$\approx$ 970, and St$\approx$ 0.003.

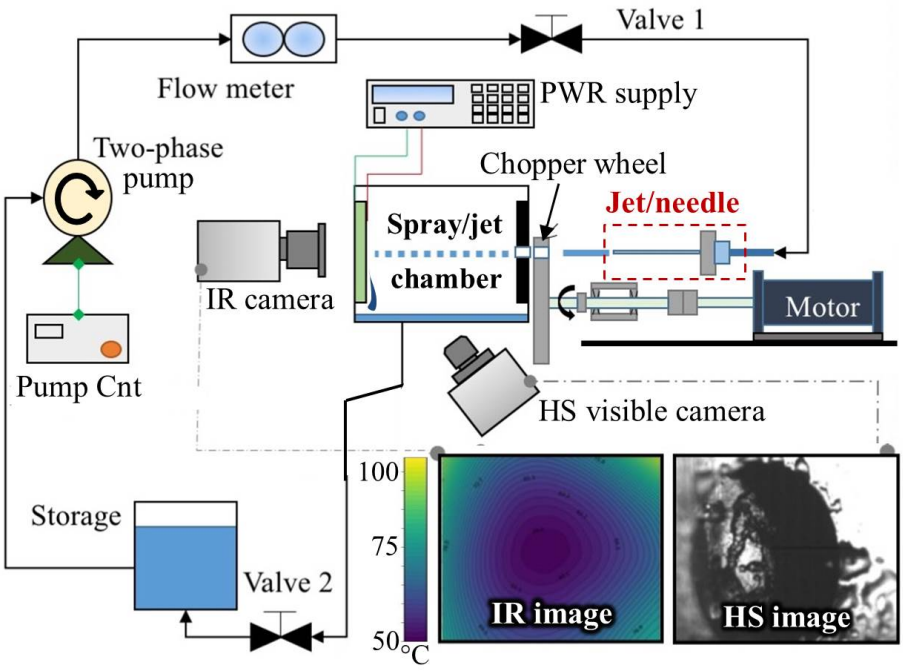

Figure 2.1: Schematic diagram of the apparatus and flow-loop for pulsed jet impingement studies.

Heater Fabrication

Fig. 2.2 illustrates the heater/thermometer fabrication process. The Titanium (Ti) thin film (50 Ω sheet resistance) is deposited on a fused silica (FS) glass substrate by dc magnetron sputtering. To maximize the adhesion of the Ti heater/thermometer to the glass substrate I first pre-sputtered 10 nm of Ti on the glass substrate. Then, this Ti-coated glass substrate is heat-treated on a hot plate in air at 400 °C for 2-3 min, followed by a rapid thermal quenching to room-temperature on a Cu cold plate. This process facilitates a durable and strong bond Ti/glass bond. Then, a polyamide mask is applied (Fig.2.2b), facilitating Ti deposition onto only a selected portion of the glass substrate for a 'band-aid' shaped heater/thermometer geometry. Then, the primary Ti (heater/thermometer) deposition is conducted for 20 min at constant power (33 W) in Argon(8.3 mTorr pressure). The corresponding Ti deposition rate is 2 nm/min and the base pressure prior to deposition is 4×10^{-9}

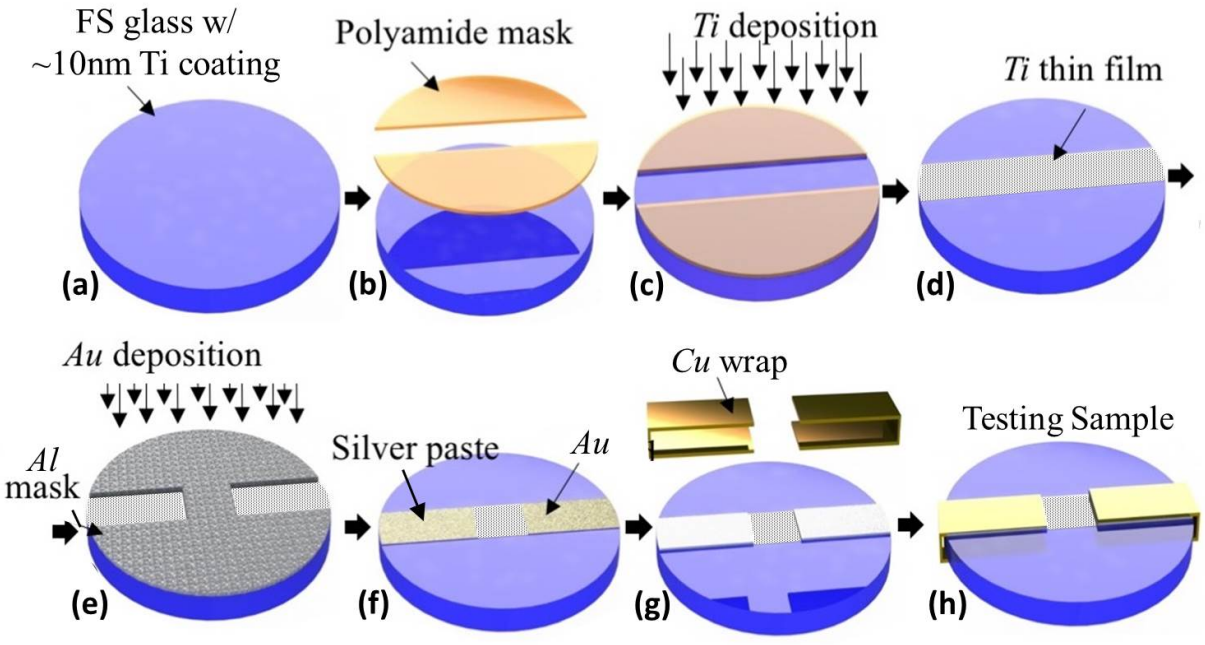

Figure 2.2: Fabrication steps for the 1cm x 1cm Ti thin-film heater/thermometer. (a) Ultrasonically cleaned substrate with pre-sputtered, heat treated Ti/TiO_2 adhesion coating ($\approx$10 nm). (b) polyamide mask application. (c) Primary, Ti thin-film deposition ($\approx$100 nm). (d) Polyamide mask removal. (e) Al mask application for subsequent Au deposition ('band-aid' Ti heater/thermometer). (f) Electrically conductive Ag paste application on Au busbars. (g) application of Cu foil/busbar wraps. (h) final heater configuration for loading into spray/jet chamber.

Torr (please see the Supplementary Material for the details).

To create the heater/thermometer busbars, Au is deposited at a deposition rate of 1.5 nm/min for 30 min at 33 W and 8.3 mTorr Ar. Electrically conductive silver paste (electrical resistivity, σ = 0.0004 Ω-cm) is applied on the Au busbars. In addition, a Cu foil wrapping is used for durable and improved electrical connections. Finally, the heater (Fig. 2.2h) is mounted in a Teflon-made sample stage holder with a machined stainless steel (SS) viewport cover. The SS cover has an O-ring groove outside the viewport area, where this whole assembly uses viton O-rings to prevent leaks and electrical shorting. A thin Polyamide mask layer is also used on the top edges of Ti

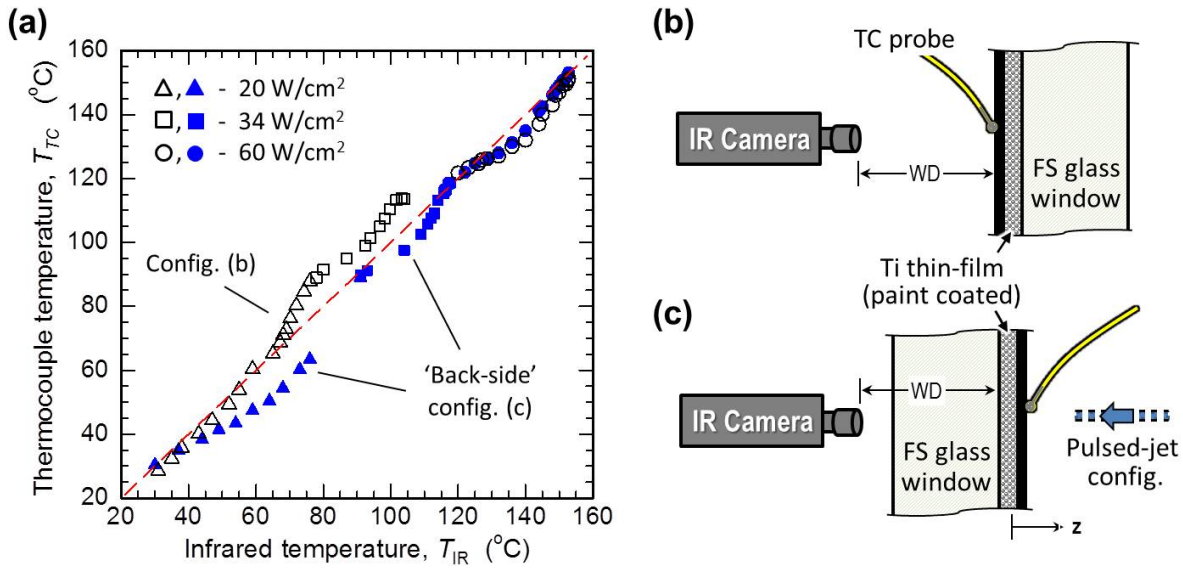

Figure 2.3: (a) Comparison between the temperatures measured using IR (T_{IR}) and thermocouple (T_{TC}) thermometry. Data is provided for three different heat flux configurations and two different measurement configurations. The curvature in the data is due to transient heating effects (i.e., steady-state conditions are only applicable at $T_{\mathrm{IR}} \approx 90$, 120, and 153°C. (b) Schematic depiction of the 'front-side' measurement configuration (not-to-scale). The open-symbol data in (a) are acquired for this 'front-side' configuration. (c) Schematic depiction of the 'back-side' measurement configuration (not-to-scale). This 'back-side' schematic depicts an impinging jet; however, no jets are used during the data acquisition for the temperature data provided in (a). As illustrated in (b) and (c), the working distance (WD) is the same for both measurement configurations. Also, the emissive black paint coating on the Ti heater/thermometer is removed after these temperature cycling experiments.

heater/thermometer surface (i.e., the region of O-ring contact) for extra mechanical protection from the o-ring seal during the required temperature cycling and pulsed jet cooling studies. The Ti heater is ohmically heated using an AC/DC power supply (Agilent HP 6813A, 300 Vrms, 1.75 kW). Four spring-loaded gold pins (mounted in the Teflon sample holder) provide electrical connections between the power supply and the thin-film heater assembly.

Visible Imaging and Temperature Mapping

To visualize the fluid flow-field and map the surface temperature on the heater surface, both the high-speed visible camera (Phantom V12.1, 640 $\times$ 480 pixels, resolution = 44 μm/pixel) and FLIR IR thermal camera (FLIR SC7650, 640$\times$512 pixels, resolution = 14.15 μm/pixel) are used, respectively. For our pulsed jet cooling studies, the IR camera is configured for pixel binning, facilitating IR recordings at 870 frames-per-second (integration time: 0.435 ms, binned window size: 160$\times$128 pixels, binned resolution = 56.6 μm/pixel). As shown in both Fig.2.1 and Fig.2.3c, the testing sample is orientated in the jet/spray chamber with the 'back-side' surface of the IR transparent glass substrate facing towards the IR camera and the 'front-side' surface coated with the Ti heater/thermometer facing the impinging jet. As shown in Fig.2.1, the high-speed visible camera is orientated for side viewing through a chamber port window. The thin-film Ti heater/thermometer is 99% opaque in thermal camera's sensitivity region, facilitating transient pixel-by-pixel local temperature measurements (please see the Supplementary Material for the details).

To estimate the emissivity of the Ti thin-film and corresponding the temperature measurement error via IR thermometry, validation experiments are conducted using the IR camera and a K-type thermocouple in contact with the surface of the Ti heater/thermometer. Fig. 2.3a provides the raw data from these experiments. To facilitate this temperature assessment process, emissive black paint is spray-coated on the Ti thin-film. The black paint is removed by toluene washing. The first test run corresponds to the open-triangle data in Fig.2.3a, indicating the transient increase in the black paint's surface temperature (starting from $\approx 30^{\circ}$C) measured by both the thermocouple and the IR camera for a constant applied heat flux of $q^{''} = 20 \pm 0.6$ W/cm^2. Fig.2.3b is a schematic illustration of the 'front-side' measurement configuration for this test, where the IR camera's image plane coincides with the paint/air interface. The recorded thermocouple temperature (T_{TC}) is the local contact temperature in the center of the sample, while the IR camera temperature (T_{IR}) is

an area-average temperature around the thermocouple's probe tip (view-area: ≈1 mm^2), using the default FLIR ResearchIR MAX software emissivity ($\epsilon = 1$) for the black paint. The second test run is indicated by the open-square data in Fig.2.3a; thus, the same measurement configuration as the first test (open-triangles), but at a higher applied heat flux of $q'' \approx 34$ W/cm^2. After data acquisition from this second test (open-squares), the sample stage is allowed to heat to a steady-state temperature of ≈ 120°C (via $q'' \approx 34$ W/cm^2). Then, the heat flux is increased to the constant value of $q'' \approx 60$ W/cm^2 (open-circle data). Thus, the open-circle data in Fig.2.3a shows the temporal evolution of $T_{\rm IR}$ and $T_{\rm TC}$ (starting at ≈ 120°C). For the subsequent tests (filled-symbol data), first the sample stage is cooled to room temperature (via ambient convection and conduction) and then rotated for 'back-side' measurements. This back-side configuration depicted in Fig.2.3c is the same configuration used for the pulsed jet experiments (i.e., IR imaging through the glass substrate with an imaging plane at the Ti/glass interface). For these back-side tests the IR emissivity setting is changed to $\epsilon = 0.45$ for Ti; yet, the thermocouple tip is still in contact with the black paint on the Ti thin-film (heater/thermometer). As shown in Fig.2.3a, $T_{\rm TC} \leqslant T_{\rm IR}$ holds for nearly all data (other than the first two 'front-side' tests up to ≈ 110°C). This temporal lag is attributed in $T_{\rm TC}$ relative to $T_{\rm IR}$ to imperfect thermocouple contact. The anomalous results for the first two 'front-side' trials are attributed to temperature annealing of the emmissivity of the black paint coating. In support, the relative deviation between $T_{\rm IR}$ and $T_{\rm TC}$ is at most ≈ 3°C at steady-state temperatures (i.e., at ≈30, 90, 120, and 150°C). Yet, because our jet cooling studies are spatiotemporal in nature with $T_{\rm IR}$ of the Ti/glass interface varying spatially from ≈40 to ≈150°C, the average temperature error is observed for each applied heat flux in the pulsed jet ('back-side') experimental configuration. From this data in Fig.2.3a, an IR temperature accuracy of $\delta T_{\rm IR} \approx \pm$ 6.6, ± 4.5, and ± 4.2°C for $q'' \approx$ 20, 34, and 60 W/cm^2 are estimated, respectively. These temperature error estimates are accounted for in all subsequent heat transfer analysis.

Methodology and Experimental Conditions

The procedure for pulsed jet cooling experiments require several initiation steps, including flow-loop leakage inspection, flow-line evacuation testing, and water charging through the flow-loop. After flow-loop inspections, the open-line configuration is tested using the syringe needle and chopper wheel for pulsed jet cooling studies. For all jet cooling experiments, the distance between the heater surface and syringe needle outlet is kept constant at $H = 80$ mm. This work used three (3) different jet pulsation setpoint frequencies with corresponding Strouhal numbers (St = $f_p D_{\text{jet}}/U_{\text{flow}}$) ranging from 0.002 to 0.0045 at a constant Reynolds number (Re = $\rho_w U_{\text{flow}}/\mu_w$) of Re $\approx$ 970. The jet pulsation frequency, f_p is defined as the number of jet ON/OFF cycles per second. These ON/OFF states of the jet are controlled by physically chopping a steady jet stream using a custom Al mechanical chopper wheel attached to the shaft of a DC motor (please see the Supplementary Material for the details).

The wall heat flux is generated by joule heating the Ti thin-film using the voltage-current monitoring power supply operated in a DC mode. All experiments are performed at ambient conditions ($T_{\text{amb}} \approx$ 22.5°C and $RH \approx 60\%$). The transient local heat flux generated by the Ti thin-film heater/thermometer takes into account the conductive losses into the FS glass substrate via

$$q"(x,y,t) = \frac{I^2 R_{\text{Ti}}}{A} - (\frac{T_s(x,y,t) - T_z}{\Delta})k_{\text{FS}}, \tag{2.1}$$

where k_{FS} is the thermal conductivity of the FS substrate, I is the applied current, R_{Ti} is the temperature dependent electrical resistance of the Ti thin-film, and A is the surface area of the Ti thin-film.

The IR camera is aligned and focused on the Ti surface, where the surface roughness and imperfections in the Ti thin-film allow for easy alignment. The thermal camera directly measures

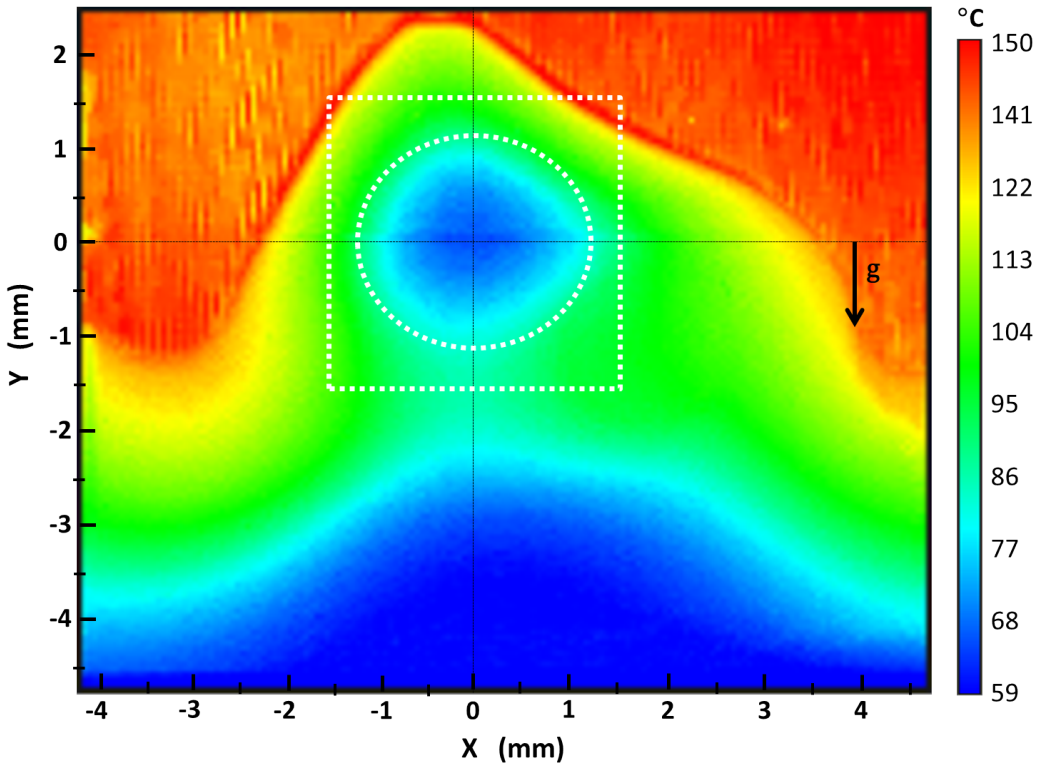

Figure 2.4: Infrared (IR) temperature map for pulsed jet cooling. The image dimensions are centered to the jet stagnation point [(X,Y)=(0,0)mm]. The circle and square overlays correspond to the jet impingement zone (JIZ) and radial-flow zone (RFZ) for subsequent analysis (Areas: $A_{\mathrm{JIZ}} \approx 4.2\mathrm{mm}^2$, $A_{\mathrm{RFZ}} \approx 9.7\mathrm{mm}^2$). Experimental details: $t \approx 0.936$ s (relative to the start of IR data acquisition), $q'' = 60 \pm 2$ W/cm^2, $f_p = 14.95 \pm 0.97$ Hz, $G \approx 795$ kg/m^{2}s, Re$\approx$ 970, St $\approx$ 0.003, $D \approx 410$ μm, $H/D \approx 200$, and $z > 0$ into the page/image.

the Ti surface/interface temperature because the Ti thin-film is opaque in IR region (please see the Supplementary Material for the details). The thickness of the Ti heater/thermometer is very thin ($\approx$100 nm). Therefore, the conduction resistances (normal to the plane) in the Ti are negligible compared to the convective resistance and 1D conduction corrections are not necessary [28]. Moreover, thermal inertia is neglected because the Ti thin-film is only $\approx$100 nm thick (please see the Supplementary Material for the details). Pixel-by-pixel IR thermal imaging data is recorded for steady-state wall heat flux conditions using the ResearchIR MAX software, where a Python

code handles: i) pixel-by-pixel temperature ($T_s(x, y, t)$), ii) fluid temperature (T_f), and iii) the local heat flux ($q^{''}(x, y, t)$). Thus, pixel-by-pixel heat transfer coefficients are generated at different heat flux and pulsed jet impingement conditions. The heat transfer coefficient in this subcooled jet impingement cooling regime can be simply calculated with

$$h(x, y, t) = \frac{q"(x, y, t)}{T_s(x, y, t) - T_f}. \tag{2.2}$$

Uncertainty Analysis

Heat flux errors are found to be in the range of $\pm 3\%$ (please see the Supplementary Material for the details). As discussed previously, the accuracy of our IR temperature measurements are estimated to be within δT_{IR} ≈4.2-6.6°C. The influence of the working distance of the IR camera on accuracy of temperature measurements is also discussed in Supplementary Material. Although not necessary, Gaussian filters are employed in the Python code to get smooth thermal and heat transfer coefficient (HTC) contours (please see the Supplementary Material for the details). The corresponding error in our HTC measurements are expected to range within 25 to 28% due to our large δT_{IR} estimates. All error bars in the subsequent data are based on these uncertainty estimates.

Results and Discussion

Spatiotemporal HTC Characterization for Pulsed Jet Cooling

Fig.2.4 shows a typical infrared temperature map acquired during a pulsed jet impingement experiment. The data in Fig.2.4 is for an applied heat flux of $q^{''} \approx 60$ W/cm^2 and a jet pulsation frequency of $f_p \approx 15$ Hz. The spatiotemporal nature of this pulsed jet cooling process is further depicted in

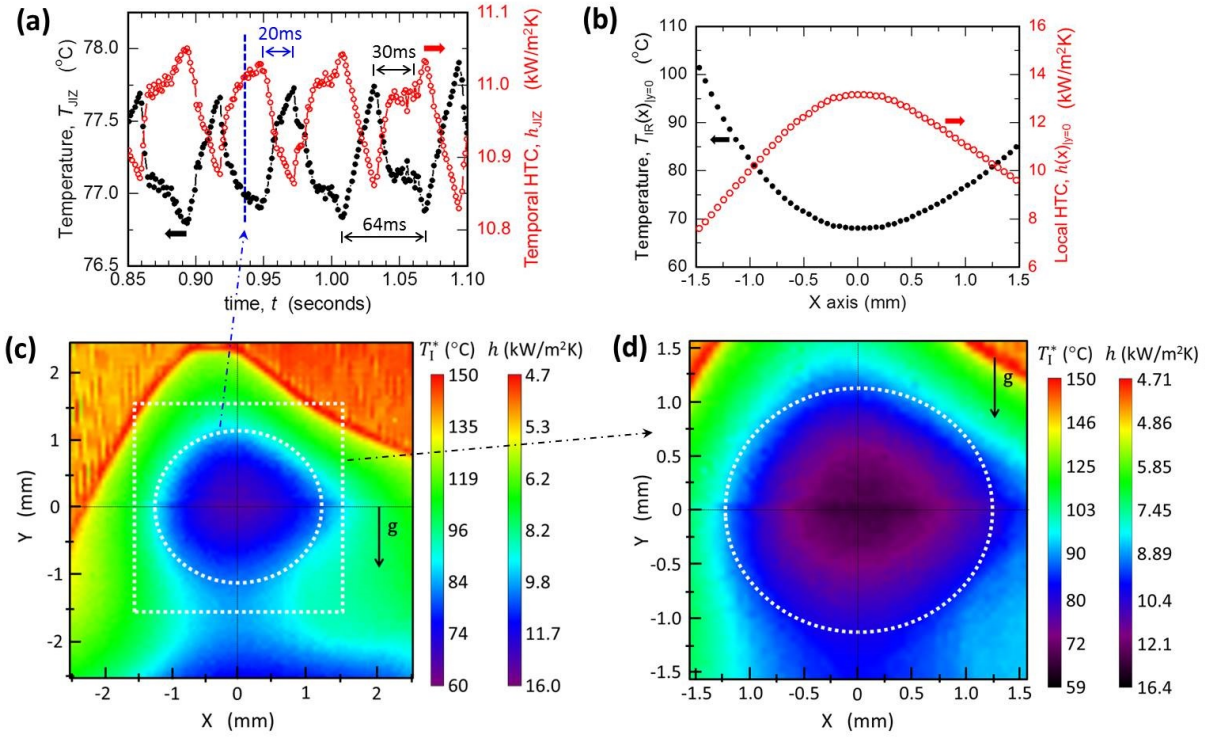

Figure 2.5: Overview of key spatiotemporal temperature and HTC data for pulsed jet cooling using IR thermography. (a) Temporal Ti thin-film (wall/interface) temperature [left-axis] and HTC [right-axis]. The data corresponds to area-averaged values within the jet impingement zone (JIZ). (b) Spatial temperature [left-axis] and HTC [right-axis] profiles across the jet stagnation point [(X,Y)=(0,0)mm]. (c) IR temperature map and corresponding HTC distribution at $t \approx 0.936$ seconds. (d) Zoom-view of the radial-flow-zone (RFZ) and corresponding jet impingement zone (JIZ) within it. Experimental details: $t \approx 0.936$ s (relative to the start of IR data acquisition), $q'' = 60 \pm 2$ W/cm^2, $f_p = 14.95 \pm 0.97$ Hz, $T_{jet} \approx 22.5$°C, $D_{jet} \approx 410\mu$m, $G \approx 795$ kg/m^{2}s, Re ≈ 970, St ≈ 0.003, $H/D \approx 200$, and $z > 0$ into the page/images.

Fig.2.5. Fig.2.5a provides the area-averaged, temporal response for both the measured Ti thin-film temperature (left-axis) and the calculated HTC (right-axis) within the jet impingement zone (JIZ). I point out that the area-averaged Ti interface/wall temperature fluctuates at the expected time-scale for pulsed jet cooling (i.e., $\delta t \approx 1/f_p$ Fig.2.5b highlights the spatial distribution of the wall temperature (left-axis) and HTC (right-axis) across the jet stagnation point within the radial-flow zone (RFZ). The zoomed-view temperature maps in Figs.2.5c and 2.5d also provide the corresponding

HTC distributions calculated via Eq.2.2, where $T_s = T_I^*$ is the Ti thin-film interface/wall temperature. As expected, the minimum wall temperatures are observed at the jet stagnation point (i.e., at [X,Y]=[0,0]mm in Figs.2.5c,d). Supplementary Material provide analogous surface temperature and HTC mapping data for all the pulsed jet cooling configurations studied in this work.

The pulsating nature of the jet induces slight oscillations in the calculated, area-averaged HTC values. These HTC (and surface temperature) oscillations are repeatable with an oscillation frequency matching the jet pulsation frequency. For example, with respect to the 'jet impingement zone' data (Fig.2.5a), the HTC increases from ≈10.85 kW/m^{2}K to ≈10.97 kW/m^{2}K within ≈15 ms after initiation of the 'jet-ON' state (or jet-cooling state). Then, this average 'jet zone' HTC commonly has a plateau for ≈10-15 ms, followed by a further increase in ≈5-10 ms to the local peak HTC value of ≈11.04 kW/m^{2}K. However, during the 'jet-OFF state (or wall-heating state) the HTC decreases from ≈11.04 kW/m^{2}K to ≈10.85 kW/m^{2}K within ≈15-20 ms. The temporal time-scales are nearly identical for local, maximum HTC data at the stagnation point (or a reduced area around the stagnation point - please see the Supplementary Material for the details). However, the magnitude of these HTC (or wall temperature) oscillations are amplified at the stagnation point. Correspondingly, maximum heat transfer coefficients (or minimum surface temperatures) are observed at the center of jet impingement zone (JIZ). This is a universal trend observed for all f_p and q'' configurations studied in this work.

While the area-averaged temperature and HTC results are temporally consistent with the jet pulsation frequency (f_p), the corresponding IR temperature maps (i.e., IR image snapshots) are not spatially uniform. The asymmetric nature in the temperature profile is due to the falling-film behavior of the fluid flow-field. This is clearly illustrated all the IR imagery data. In addition, the IR imagery data in Figs.2.5c and 2.5d show that the HTC (or surface temperature) contours within the jet impingement zone keep rather parallel to each other - signifying uniform thermal diffusion within the jet impingement zone. However, at larger length-scales (e.g., outside the jet impinge-

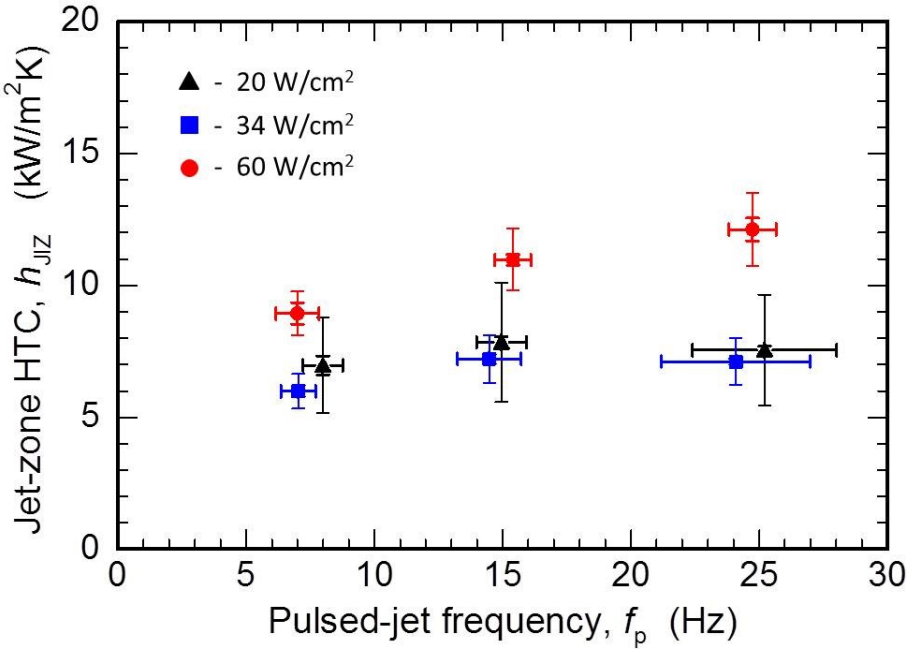

Figure 2.6: HTC data as a function of jet pulsation frequency and applied heat flux. The HTC values are based on area-averaged wall/interface temperatures within the jet impingement zone (JIZ). The relative error in f_p is based on temporal analysis of the acquired $T_{\rm JIZ}$ data, where $T_{\rm JIZ}$ is the average spatiotemporal wall temperature recorded within the jet impingement zone during an IR acquisition period of ≈5 seconds. The relative error in $h_{\rm JIZ}$ is provided based error propagation using the standard deviation in the applied heat flux ($\delta q''$) combined with either i) $\delta T_{\rm IR}$ ('larger error-bar data') estimated from the temperature cycling studies or ii) $\delta T_{\rm JIZ}$ ('smaller error-bar data') due to temporal drift in $T_{\rm JIZ}$ measured throughout an entire ≈5 second IR data acquisition. Experimental details: $T_{jet} \approx 22.5$°C, $D_{jet} \approx 410\mu$m, $G \approx 795$ kg/m^{2}s, Re ≈ 970, St ≈ 0.003, $H/D \approx 200$, $q'' = 20 \pm 0.6$, 34±1, and 60±1.8 W/cm^2, $f_p = 7.99$±0.77, 14.95±0.97, and 25.21±2.81 Hz.

ment zone) the HTC maps are distorted - especially at the bottom of the radial-flow zone due to falling-film cooling effects. Supplementary Material provides additional data of the spatial HTC and wall temperature distributions around the stagnation point.

Fig. 2.6 provides an overview of the HTC measured as a function of the jet pulsation frequency (f_p) for the different heat flux configurations studied in this work. The enhancement of the heat transfer coefficient with increasing pulsation frequency is potentially due to interfacial waves and

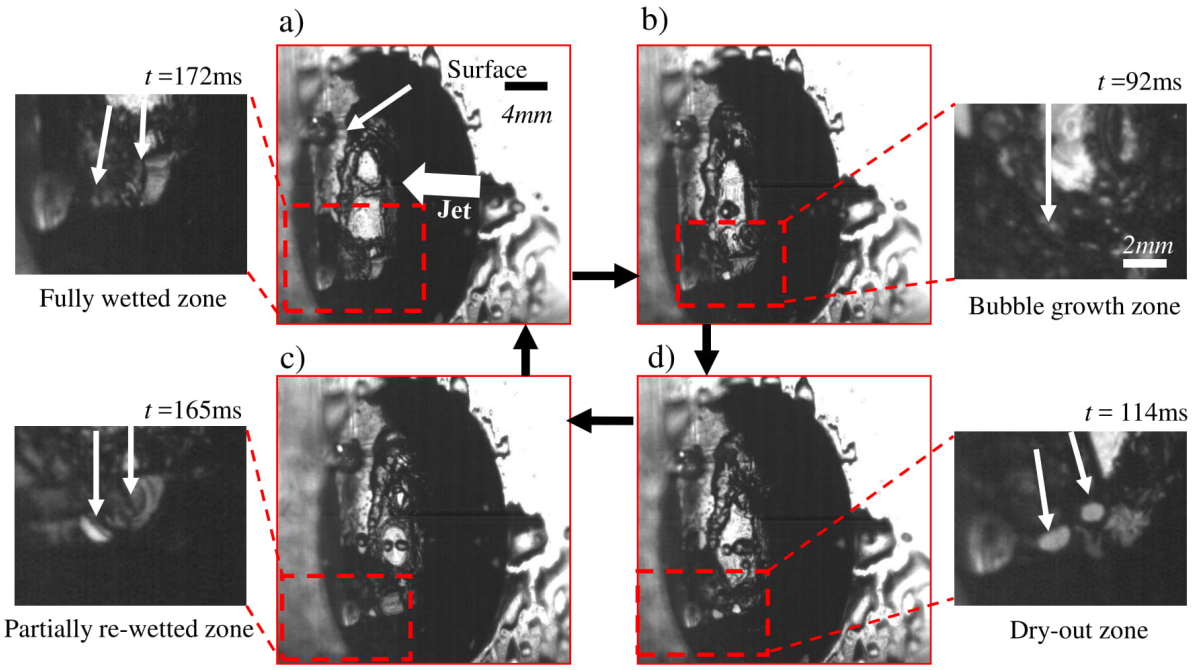

Figure 2.7: High-speed visible imagery data for the jet impingement and falling thin-film boiling cycles ($f_p \approx 15$ Hz, $q'' \approx 60$ W/cm^2, $G \approx 795$ kg/m^{2}s, Re ≈ 970). (a) Image of bubbles starting to appear at a radial location from center of the impinging jet. (b) Visual representation of dry-out zones as the bubbles tend to grow and collapse. (c) Image showing that the surrounding water coolant tends to wet the dry-out zones with the appearance of partially re-wetted zones. (d) Imagery of the fully-wetted zones as the next jet/droplet pulse of liquid starts to impact the heated wall.

boiling events. No boiling events are observed for $q'' = 20 \pm 2$ W/cm^2. Interfacial waves increase the effective interfacial area causing the mean film thickness to drop at the radial locations from the stagnation point of the impinging jet. Moreover, boiling events appear between radial-flow waves that are observed at the highest heat flux condition studied ($q'' \approx 60$ W/cm^2). This potentially reduces the overall thermal resistance at the edge of the jet impingement zone. For such heat and mass transfer conditions, the overall heat transfer performance is enhanced.[29]

Pulsed Jet Boiling Events

Fig. 2.7 illustrates the cyclic events that occur during pulsed jet impingement cooling for a heat flux condition of $q^{''} \approx 60$ W/cm^2). Bubble nucleation is clearly visible at different locations on the Ti heater/thermometer surface – especially near the edge of the jet impingement zone. Fig. 2.7a shows bubble nucleation at $t \approx 92$ ms. The subsequent images (i.e., 2.7b, 2.7c, and 2.7d) show that within ≈18 ms the vapor bubbles have completely collapsed to a millimeter-sized dry-out region. In fact, the vapor bubbles collapse in $\approx 1-2$ ms. For example, Fig. 2.7b shows the fully developed dry-out region at $t \approx 114$ ms. Moreover, after a complete dry-out event (2.7a→2.7b), the heater surface is partially re-wetted (2.7c). Then, a full re-wetting of the surrounding water jet/droplets occurs (2.7d). This development of a fully re-wetted zone occurs via a coexistence of both a thin-film fluid layer and a newly impinging jet. The occurrence of these cyclic boiling, dry-out, and re-wetting events is observed to be very random; however, the corresponding time duration of each event tended to be rather universal. As previously illustrated in the spatiotemporal IR data in Fig. 2.5, these major cyclic events occur on the heater surface with highly radial thermal gradients and at relatively low local wall subcooling temperatures. Thus, the maximum HTCs are observed at the center of the jet impingement zone. A potential mechanism for these cyclic boiling events during pulsed jet cooling is further discussed in Supplementary Material.

Falling Film Instability Criterion

To further investigate the role of the pulsed jet in terms of a critical pulsation frequency, the instability associated with falling liquid-film under gravity must be understood. This falling liquid film encounters interfacial instabilities because of pressure difference at liquid-air interface.[30]. These instabilities caused by a pulsating jet are mainly due to the imbalance in the inertia and thermocapillary forces (due to surface tension gradients in the liquid film and tangential shear stress

at the solid-liquid interface).[31, 32, 33, 34] The dominance of the inertia force due to the unsteady (pulsating) nature of the jet can be described by Strouhal number [35]. These instabilities are fueled by thermocapillary breakdown when a pulsed liquid jet comes into contact with heated surface (please see the Supplementary Material for the details). During this modulated (unsteady) two-phase cooling process, the boiling events at radial locations of the impinging jet appear in cycles. The oscillating nature provides rigorous vapor formation at high thermal loads. Such pulsed perturbations assist the formation of an unsteady vapor blanket that exerts a tangential shear stress on the radially flowing and oscillating liquid thin-film. The change in the film thickness from the wave-crest to the wave-trough causes potentially additional perturbations in gravity-induced flow rate. Moreover, the tangential stress opposes this gravity effect and subsequently decreases the overall flow-rate perturbations within the liquid-film region. Thus, the tangential stresses reduce the inertia-driven radial flow rate, which further suppresses the Kapitza instability.[36, 37]

An empirical correlation is beneficial to predict critical Marangoni number for wide range of Reynolds numbers [38]. The following relation can be used to correlate the Maragoni (Ma), Prandtl (Pr), and Reynolds (Re) numbers for a falling liquid-film:

$$\frac{\mathrm{Ma}}{\mathrm{Pr}} = 0.115\mathrm{Re}^{0.65}, \tag{2.3}$$

where Ma = $\partial\gamma/\partial T \times \delta\Delta T/\mu\alpha$, Pr=$\nu/\alpha$, γ is the surface tension, δ is film thickness, and $\alpha = k/\rho c_p$ and $\nu = \mu/\rho$ are the thermal and momentum diffusivity, respectively. During boundary layer formation, the falling film velocity is similar to that of the jet impingement velocity. Thus, the falling film is not influenced by the heater's surface roughness but is influenced by the gravitational body force. And, for a gravity-induced falling film, asymmetric large waves (preceded by small ripples) form due to Kapitza instability.[39]

The critical wavelength of the ripples in this falling film can be described via the Rayleigh-Taylor instability wavelength:[40]

$$\lambda_o = 2\pi\sqrt{\frac{\gamma}{g(\rho_l - \rho_a)}}, \tag{2.4}$$

where ρ_l and ρ_a are density of liquid and air, respectively.

[41] modeled the thermo-capillary breakdown of these larger waves (i.e., waves with $\lambda >> \lambda_o$) due to perturbation of liquid film on a heated surface. This work yielded an instability criterion in terms of a non-dimensional Kapitza number (Ka). Neglecting the friction at the water-air interface, the instability criterion can be expressed as

$$\frac{\mathrm{Ma}}{\mathrm{PrKa}} = 0.093\frac{U_r}{U_w}, \tag{2.5}$$

where $\mathrm{Ka} = (f_w\lambda_o/\nu^{1/3}g^{1/3})^2$. Moreover, U_r,U_w,f_w signify residual layer velocity, wave velocity and perturbation frequency, respectively. Ambrosini et al. [42] provided an experimental evidence for heated water as to how these wave velocity (U_w) and residual layer velocity (U_r) can be scaled with Reynolds numbers. From their investigation, the ratio of wave velocity to residual layer velocity is found to be between 2 and 2.2 for warm water (70°C). Thus, Eqns. 3-5 can be used to predict a dominant (or critical) perturbation frequency for heat and mass transfer in a falling liquid-film. During our pulsed jet cooling experiments, this perturbation is induced by the impact of the pulsed jet on the heated substrate. Therefore, the dominant perturbation frequency, $f_{\mathrm{Ka}} = (\mathrm{Ka}\nu^{1/3}g^{1/3}/\lambda_o)^{0.5}$ can be potentially used to determine the optimum pulsation frequency, f_p (please see the Supplementary Material for the details). The Re $\approx$ 970 and the mass flux are fixed at $G \approx$ 795 kg/m^{2}s. Nevertheless, a critical jet pulsation frequency (via Eqns. 3-5) of $f_p = f_{\mathrm{Ka}} \approx$ 18.9 Hz -19.8 Hz is expected in this work. As a result, a roll-off (decrease) in the thermal cooling performance is anticipated for pulsed jets with $f_p > f_{\mathrm{Ka}}$. However, no clear connection between f_p and f_{Ka} is observed for augmenting the overall heat transfer performance.

It is important to note that the absence of the Kapitza number (Ka) in the equation makes it difficult to directly couple two equations. Ideally, a predictive correlation for thermocapillary breakdown in the falling-film configuration should be dictated by the Reynolds number (Re), Prandtl number (Pr), Marangoni number (Ma), Kapitza number (Ka), and Boiling number (Bg). The boiling number is important during multi-phase cooling because interfacial heat transfer depends on both the local heat flux and vapor quality. To produce a more robust and compatible empirical or semi-empirical model, more experiments are needed with a broad range of heat fluxes and working fluids. This would also lead to better predictions of the cut-off frequency.

Instantaneous Heat Flux Matching

To further understand the influence of the jet pulsation frequency on the cooling performance (i.e., the HTC) this cooling process is dictated by several thermofluid transients must be acknowledged. The heat flux for all transient thermal transport processes must be matched at the interface between two dissimilar materials (e.g., at the FS/Ti and Ti/jet interfaces). A transient heat source is commonly described in terms of its thermal penetration depth (l_{th}). The thermal penetration depth for a modulated heat source can be given by $l_{th} = \sqrt{2\alpha/\omega}$, where $\omega = 2\pi f_p$ is the angular modulation frequency of the heat source. An impinging jet on a heated surface also leads to either a fully-developed or developing thermal boundary layer (depending on the transient nature of thermofluid dynamics). The average thickness of the thermal boundary layer (for both steady and unsteady conditions) can be expressed as $\delta_{th} = k/h_\omega$, where k is the thermal conductivity of the fluid and h_ω is the frequency dependent heat transfer coefficient.[43] This transient HTC is dictated by both the thermal effusivity of the fluid and the transient time-scales of the thermal transport process – i.e., $h_\omega \propto e_{th}\sqrt{\omega}$, where for steady-state conditions either (i) $\omega \to 0$ or (ii) $\omega \to \infty$. The latter applies to only ultra-high frequency situations when the magnitude of the perturbation amplitudes are negligible. In regards to the former, $h_{\omega\to 0}$ is the traditionally reported

heat transfer coefficient (HTC) for macroscale thermal transport.[43] Thus, for transient heat and mass transfer in a thin liquid film, δ_{th} can be of the same order as l_{th} for relatively low-frequency temperature (or flow-field) oscillations. For example, $l_{th} \gtrsim \delta_{th}$ when $f_p \lesssim 50$ Hz – based on typical thermofluid characteristics of a water cooling process ($k = 0.6$ W/m·K, $\alpha = 0.15 \times 10^{-6}$ m^2/s, $h \approx 20$ kW/m^2·K). Nevertheless, the transient thermal boundary layer thickness scales with the thermal penetration depth as $l_{th} = \sqrt{2}\delta_{th}$, which leads to the following:

$$\frac{k_{\text{jet}}}{h_{\max}} = \sqrt{\frac{\alpha_{\text{jet}}}{2\pi f_p}}. \tag{2.6}$$

Rewritting Eq.2.6 in terms of the thermofluid perturbation frequency leads to the following relation for a critical frequency at a solid-liquid interface:

$$f_p^* = (\frac{h_{\max}}{\epsilon_{th}})^2 \frac{1}{2\pi}, \tag{2.7}$$

where $e_{th} = \sqrt{k\rho c}$ is thermal effusivity of the working fluid. Assuming that the contact resistance between solid heater wall and liquid jet is negligible, the solid/liquid interface temperature (T_{I^*}) must be constant (temporally invariant) for time-scales less than that required for steady heat transport (i.e., T_{I^*} is a constant for $t \leqslant 1/f_p^*$).

Although the temperature profile inside the two bodies in contact will be evolving in time, during this transient pulsed jet cooling process the instantaneous heat flux across the wall interface must be continuous (i.e., a balance between solid-to-wall and wall-to-jet heat flux - $q''_{s\to Ti} = q''_{Ti\to jet}$). This requirement for instantaneous heat flux matching yields a unique wall/interface temperature,

$$T_{I^*} = \frac{T_s e_{th,s} + T_{jet} e_{th,jet}}{e_{th,s} + e_{th,jet}}, \tag{2.8}$$

where $e_{th,s}$ and $e_{th,jet}$ are the thermal effusivities of the solid FS substrate and pulsed water jet (re-

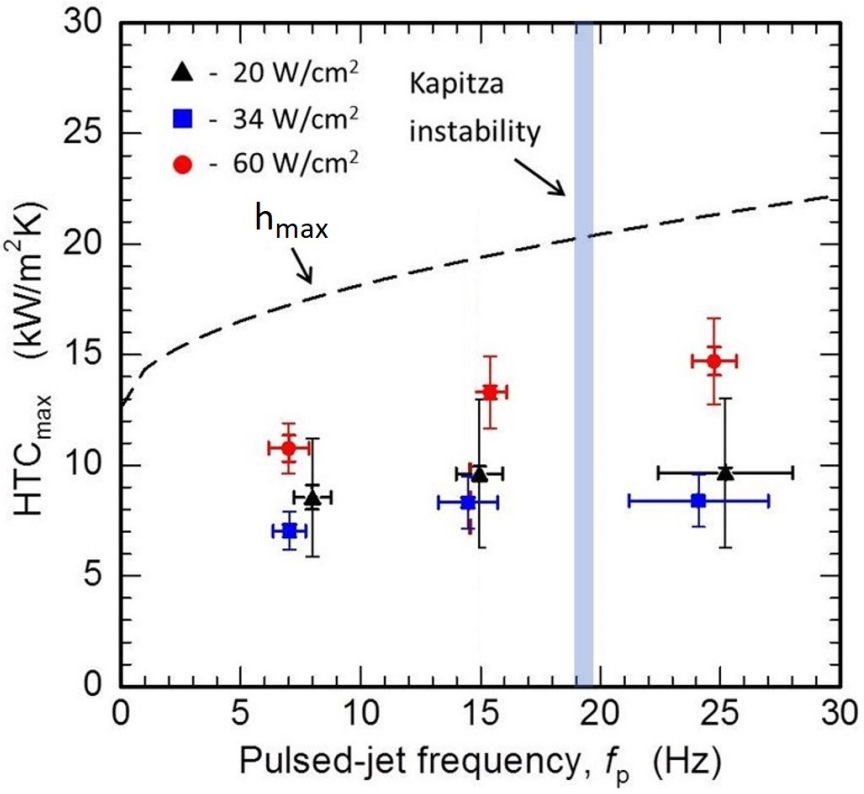

Figure 2.8: Impact of the jet pulsation frequency on the maximum heat transfer coefficient measured (symbols) and predicted (dashed-lines) in this work. The HTC values correspond to the maximum values measured at the jet stagnation point. The error-bars for the HTC data are derived based on the same methodology addressed in Fig. 2.6. The predicted HTC is based on h_{max}: Eq. 2.10. The vertical dashed line is predicted frequency for Kapitza instability criterion (f_{Ka} via Eqns 3-5).

spectively) and T_s and T_{jet} are the steady-state substrate and jet temperatures outside the thermal boundary layer ($|z| > \delta_{th}$).[44]. However, because the pulsed jet induces spatiotemporal convection heat transfer from the heater wall/interface, an effective thermal effusivity of the pulsed jet should be used to accurately represent the experimentally observed thermal response at the wall/jet interface. In this regard, Eq.2.8 can be rewriten as

$$e^{\mathrm{eff}}_{th,jet} = \epsilon_{th,s} \frac{T_s - T_{I^*}}{T_{I^*} - T_{jet}}, \tag{2.9}$$

where now the unique wall/jet interface temperature (T_{I^*}) is directly correlated to the measured Ti heater/thermometer surface temperature (i.e., $T_{I^*} \approx T_{\mathrm{Ti}}$ via measurement by IR thermometry).

For jet impingement cooling with a steady laminar jet, the local heat transfer coefficient is of the form: $h_0 = (k/L_c)\mathrm{Nu}$, where L_c is a critical length-scale for this forced convection cooling process and the Nusselt number can be expressed as $\mathrm{Nu} = 0.332\mathrm{Pr}^{1/3}\mathrm{Re}^{1/2}$. Nu is commonly expressed with coefficients > 0.332 and different powers for Pr and Re;[45, 46] however, to (i) avoid data fitting and (ii) conserve first-principle derivations thereof, 0.332, $\mathrm{Pr}^{1/3}$, and $\mathrm{Re}^{1/2}$ are used. Notwithstanding the functional form for this steady, dimensionless HTC (Nu), the heat transfer coefficient for pulsed jet cooling can be now predicted by augmenting the 'steady laminar jet' HTC with that from Eqns.2.7-2.9 - i.e., $h = h_0 + h_\omega$. The maximum heat transfer coefficient expected for pulsed jet cooling is

$$h_{\max} = 0.332\frac{k_{\mathrm{jet}}}{\sqrt{2}D_{\mathrm{jet}}}\mathrm{Pr}^{1/3}\mathrm{Re}^{1/2} + e_{th}^{\mathrm{eff}}\sqrt{\frac{2f_p}{\pi}}, \tag{2.10}$$

where $L_c = \sqrt{2}D_{\mathrm{jet}}$ to account for expansion, $k_{jet} = k_{water} = 0.6$ W/mK, and $e_{th,jet}^{\mathrm{eff}} = 2.2 \pm 0.3$ kWs$^{1/2}$/m^{2}K is that calculated via Eq. 2.9 using $e_{th,s} = 1.48$ kWs$^{1/2}$/m^{2}K for FS and T_I^* measured in this work. For reference, the steady jet contribution to the HTC (first-term, Eq.2.10) is $h_0 \approx 12.6$kW/m^{2}K. It is noted that the $1/\sqrt{\pi}$ factor in the pulsed jet HTC contribution (second-term, Eq.2.10, in comparison to that obtained via rewritting Eq.2.7) is based on derivation using Newton's law of cooling, the finite superposition solution for $T(z,t)$,[44] and comparative analysis of the analytic solution for the wall heat flux (i.e., $-k\partial T(z,t)/\partial z$ evaluated at the wall ($z = 0$) and at a time-scale of $t = 1/f_p$).

Fig.2.8 compares our predicted and measured heat transfer coefficients (HTCs) for sub-cooled pulsed jet cooling in a falling liquid-film configuration. Both the measured and predicted data represent the local HTC values at the jet stagnation point. It is noted that the maximum HTCs (or min-

imum surface temperatures) are observed at the jet stagnation point – e.g., at $(X, Y) = (0, 0)$mm in Figs. 4 and 5. As illustrated in Fig.2.8 fair agreement is observed between the experimental data and the theoretical predictions of heat transfer coefficient. The use of other correlations for the steady laminar jet contribution[45] yield comparable values for h_0 (i.e., $h_0 \approx 2 - 20$ kW/m^{2}K); yet, those correlations are not validated for the $H/D \approx 200$ used in this work. Also, our predictions based on instantaneous heat flux matching did not account for the temperature discontinuity at the liquid-vapor interfaces and flow-field instabilities. Therefore, if the estimates of eth^{eff} do not indirectly account for such effects, then the theoretical model should be an overestimate the heat transfer coefficient. As discussed previously, for a jet pulsation frequency greater than the critical pulsation frequency (f_p^*), these instabilities are well-suppressed which reduces the rate of enhancement in heat transfer coefficient. With this said, HTC suppression is not evident in our experimental data set. A better correlation between experiment and theory is expected given derivation of an analytic solution that can also account for the frequency dependence of the amplitude of the surface temperature oscillations. The magnitude of such surface/wall temperature oscillations (Fig.2.5a) are observed to scale directly with the applied heat flux and indirectly with pulsed jet frequency. Also provided in Fig.2.8 is the predicted Kapitza instability cut-off frequency (via Eqns. 3-5). For reference, the impact of the jet Reynolds number (Re) on this predicted cut-off frequency (f_{Ka}) is illustrated in Supplementary Material. A roll-off (or plateauing) in the measured HTC is expected for jet pulsation frequencies $>>$ f_{Ka} because a high-frequency pulsed jet will represent a turbulent jet. Moreover, at large heat fluxes and $f_p >>$ f_{Ka} the spatiotemporal surface temperature fluctuations will be driven by chaotic boiling events. However, the current data set does not show any augmentation to the HTC other than the predicted $\sqrt{2f_p/\pi}$ dependence.

Summary

IR thermography is shown to be a useful technique for mapping/visualizing spatiotemporal surface temperature (T_S) and heat transfer coefficient (HTC) during pulsed jet impingement cooling on Ti coated glass window. This investigation uses such data to understand two-phase thermofluid transients at the solid/liquid interface using the cooling rate and flow-field perturbations from pulsed jets. This work illustrates the important interdependence between the spatiotemporal cooling performance (i.e., the transient HTC distribution) and jet pulsation frequency. This interdependence is reinforced via analysis based on an instantaneous heat flux matching at the heat-source and heat-sink interface (glass/Ti and Ti/jet interfaces, respectively). Experimentally, it is observed that the HTC in the jet impingement zone increase in magnitude by ≈13-17% by increasing the jet pulsation frequency from ≈7 to ≈25 Hz. Moreover, using in-situ high-speed visible videography, conjugate and cyclic boiling dynamics are captured in concert with the pulsed jet impingement process (e.g., visualizations of the cyclic bubble growth, bubble collapse, wall dry-out, partial re-wetting, and then full re-wetting process). It is observed from this cyclic boiling process that the jet pulsation frequency matches well the frequency associated with bubble release and wall dry-out. In addition to these findings, our maximum HTC predictions match well with our jet pulsation experiments. However, to capture the impact of pulsation at high transient settings, the conventional thermal imaging camera fall short because of limited resolutions (both spatial and temporal). To solve this problem, a quantum-dot-based thermal mapping technique with a higher temporal and spatial resolution is introduced and detailed in Chapter 3.

CHAPTER 3: LASER INDUCED THERMAL MAPPING USING QUANTUM DOTS

This chapter is from the publications below by Rabbi, Borden, and Putnam (2020) and Rabbi, Carter, Sanchez, and Putnam (2019):

Khan Md Rabbi, Christopher Borden, and Shawn A Putnam. A novel thermal mapping technique using nano-confinement assisted quantum dots for transient cooling applications.In 2020 19th IEEE Intersociety Conference on Thermal and Thermomechanical Phenomena in Electronic Systems (ITherm), pages 926–931. IEEE, 2020. [47]

Khan Md Rabbi, Jake Carter, Juan Sanchez, and Shawn A Putnam. Laser-scanning fluorescence thermography for thermofluid heat transfer. In 2nd Pacific Rim Thermal Engineering Conference, 2019.[48]

Literature Review

With the ever-growing demand for more powerful, faster, and smaller electronic processing comes the need for increased cooling efficiency and new, creative exploitation of natural phenomena to extract as much heat wicking possible. In order to implement these new pioneering methods of nanoscale thermal cooling, technologies must be developed to quickly and efficaciously investigate, study, and document under a wide variety of applications.

For example, in two-phase liquid cooling, bubble dynamics, rewetting events can be really transient phenomena [49, 50]. To generate understanding of thermal evolution during these unsteady and random events, highly spatio-temporal imaging technologies must be deployed which are highly expensive, complex to calibrate. Some methods have already been developed showing the capac-

ity to conduct ultrafast imaging [51] utilizing quantum dot processing. Refining these technologies into a reusable and low-cost process would be an invaluable asset to interfacial research. Equipment has been developed utilizing quantum dot technology by employing Cadmium-Telluride (CdTe) and Cadmium-Selenide (CdSe) based structures because of their great temperature sensitivity and considerably better luminescence [52, 53, 54, 55]. Other more specific photodetectors have been designed to detect mid-range light emissions, called mid-wavelength infrared detectors (MWIR), utilizing compounds such as Indium antimonide (InSb) and Mercury Cadmium Telluride (HgCdTe) [56] for their proven track record in other imaging technologies. Others use quantum dot technology to measure temperature changes in individual cells of tissue [57]. Very promising technologies have arisen as a result of quantum dot methodology, and extended research promises the possibility of ultrafast, sensitive and low-cost quantum dot alternatives to image processing [58]; creating a standard method of operation to construct a high resolution thermal diagnostic technique.

This chapter reports such an inexpensive but effective technique to perform thermal mapping accurately at the solid-fluid interface. The photoluminiscence of differently sized quantum dots are utilized to get accurate thermal information. To achieve uniform coating, QDs are trapped into nanomembranes or everyday use paper by in-house dip-coating or drop-casting technique. With proper calibrations, the technique is then applied to micro-droplet impingement cooling and hemi-wicking flows to showcase spatio-temporal benefits in temperature measurements.

Methodology

Fig. 3.1 showcases the experimental setup used in this investigation. Dip coating and drop-casting techniques are employed to trap quantum dots inside nanopores (d = 20-30 nm) of ceramic membranes and inexpensive paper. For this purpose, quantum dots-toluene solution of 20 mg/ml con-

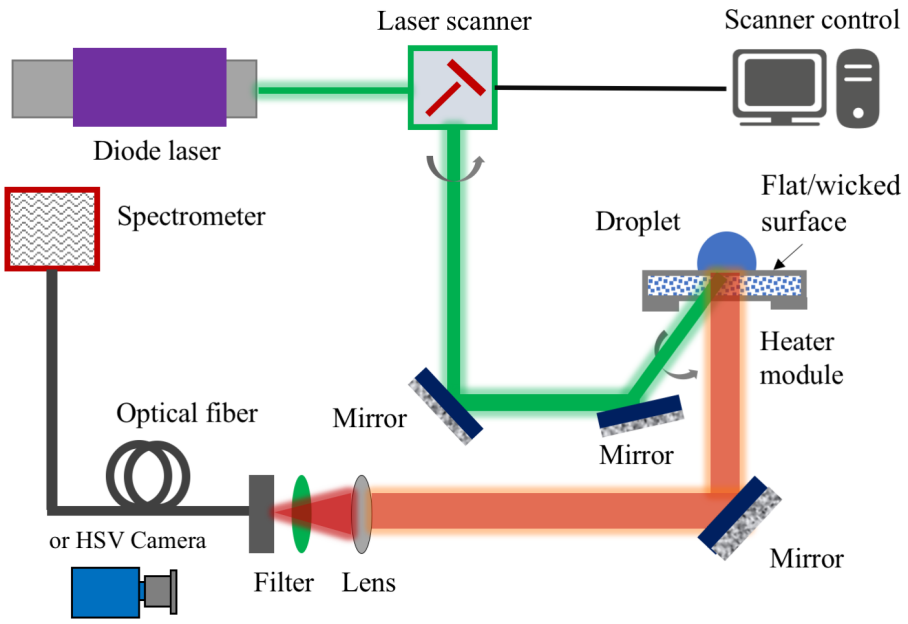

Figure 3.1: Experimental scheme: High speed LASER scanner with an amplitudes of A_x, A_y = 100 mm, 80 mm and frequencies of f_x = 133 Hz, f_y = 533 Hz is employed to scan whole Region of Interest (ROI) to capture fluorescence from uniformly heated Quantum Dot (QD)-coated flat/hemiwicking surface

centration is made. In this regard, non-toxic $CuInS_2$/ZnS quantum dots of size, d = 5nm and peak emission at 550 nm and 750 nm are chosen. This solution is undergone several ultrasonication baths to avoid settling of the nanoparticle inside the solution.

Once the quantum dot nanoparticles are well suspended inside the toluene solvent, the suspension is transferred to the cuvette which acts as a dip-coating reservoir. A Teflon-made-holder holds the nanomembrane flake which is carefully aligned with the cuvette. During dip coating, three important features are tuned to achieve very uniform thin film of quantum dots. These features are the dipping velocity (5mm/s), waiting time (1s) and withdrawal velocity (0.05mm/s). During dip coating, due to capillary forces and surface wetting phenomenon, the quantum dots suspension wets the nanomembrane and thus nanoparticles tend to get trapped inside the nanopores. Once

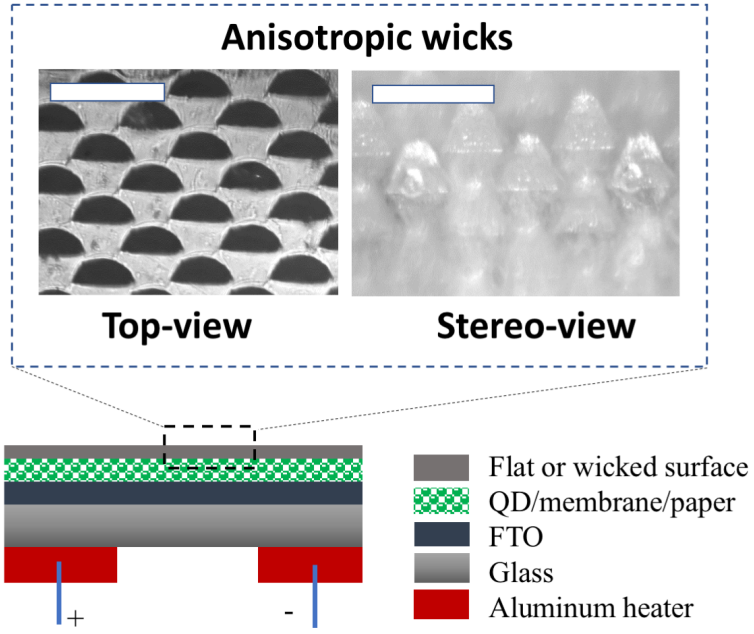

Figure 3.2: Heater module: QD loaded nanomembrane/paper is attached onto Fluorine Tin Oxide (FTO) coated soda lime based glass substrate (thickness of 1.1 mm) using Norland Optical Adhesive (NOA). Here, the white line represents a length scale of 60μm.

the withdrawal starts, the toluene solvent begins to evaporate off and all the quantum dots remain trapped after full withdrawal. Moreover, the drop-casting is performed at elevated temperature so that solvents get the chance to evaporate quickly without creating a "coffee-ring" effect on the paper. Once the uniform thin film of quantum dots is achieved, the saturated nanomembrane/paper is placed on ultrasonically cleaned Fluorine Tin Oxide (FTO) coated Boro-Silicate based glass substrate (see Fig. 3.2). To keep the nanomembrane/paper in place with the sample, the optically transparent epoxy (Norland Optical Adhesive 61) is used and cured inside a UV chamber. The sample is then attached with a resistive heater using highly conductive (k = 403 W/m-K) copper foils. Fig. 3.3 shows detailed fabrication steps to have hemiwicking surface. As shown in the illustration, a microscale drill bit pokes holes on a acrylic plastic window. A heating LASER (405nm of wavelength) heats locally and melts the drilling location before the poking happens.

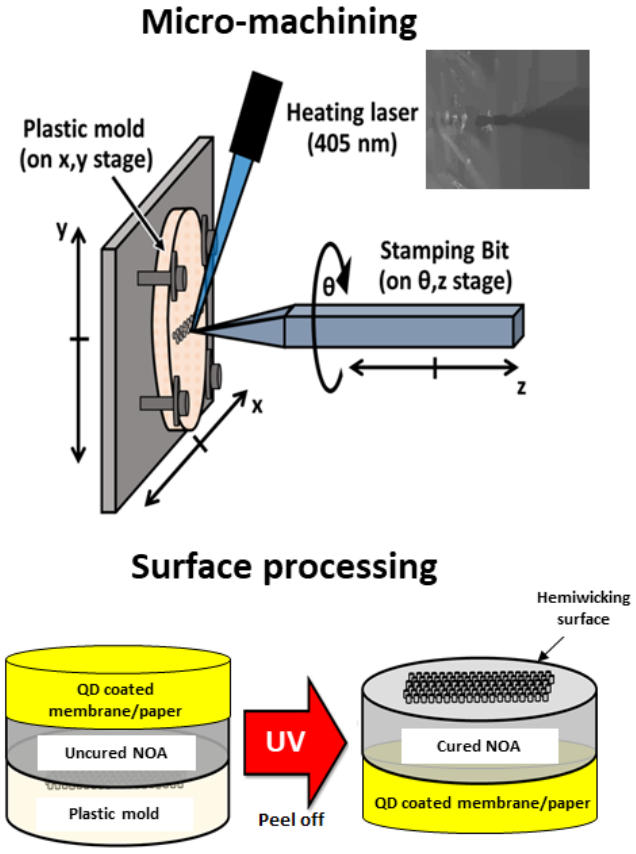

Figure 3.3: Fabrication: hemiwicking surface using microstamped plastic mold [1]

Thus, a pattern of microscale holes are found on the plastic sample. Later, NOA is poured into the plastic mold and Quantum Dot (QD) coated nanomembrane or paper is attached on the top. After 30 min of UV curing, the QD dot coated hemiwicking surface is found by peeling the layer off from the plastic mold.

As shown in Fig. 3.1, to excite the quantum dots with external means, high power diode laser (4W at 440nm) is used. A high speed laser scanner (galvanomirror), controlled by a LABVIEW program, scans the quantum dot coated region (1cm x 1cm) at frequencies, f_x, f_y = 133 Hz, 533 Hz and amplitude, A_x, A_y = 100 mm, 80 mm. The spectral information (e.g. photoluminescence) from

the quantum-dot coated thin film is captured using an OceanOptics spectrometer at an integration time of 500 ms and sample rate of 6. It is to be noted that, a 500 nm filter is installed to filter out the contribution coming from the excitation laser.

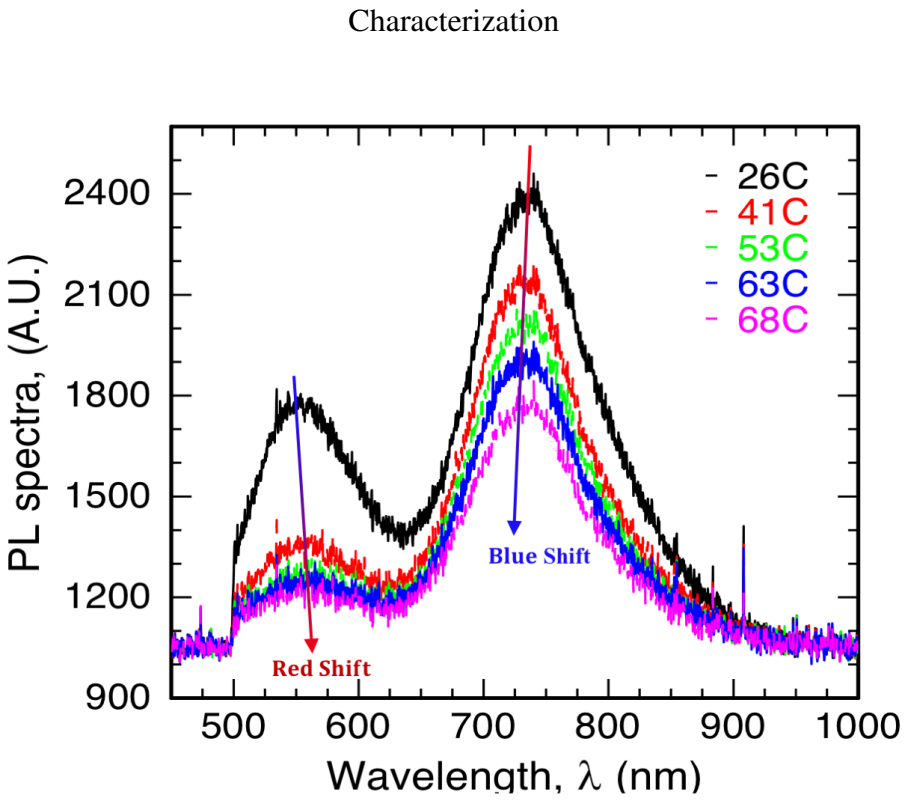

Figure 3.4: Photoluminescence (PL) spectra profile as a function of wavelength for dual quantum dotted sample at P_{laser} = 3.5W for temperature levels from 26°C to 68°C

Fig. 3.4 illustrates the photoluminescence distribution over wavelength at excitation laser power of 3.5W. Intensity of the QDs at different temperature levels can be characterized by energy band configurations. A dual quantum dot coating (750nm and 550nm) is chosen as it serves better PL intensity range and significant blue/red-shifts. At high temperature level, the probability of radiation conversion decreases which leads to lower quantum yield. Additionally, as the temperature

increases, exciton-optical phonon coupling and exciton-acoustic phonon coupling correspond to higher non-radiative recombination [59].

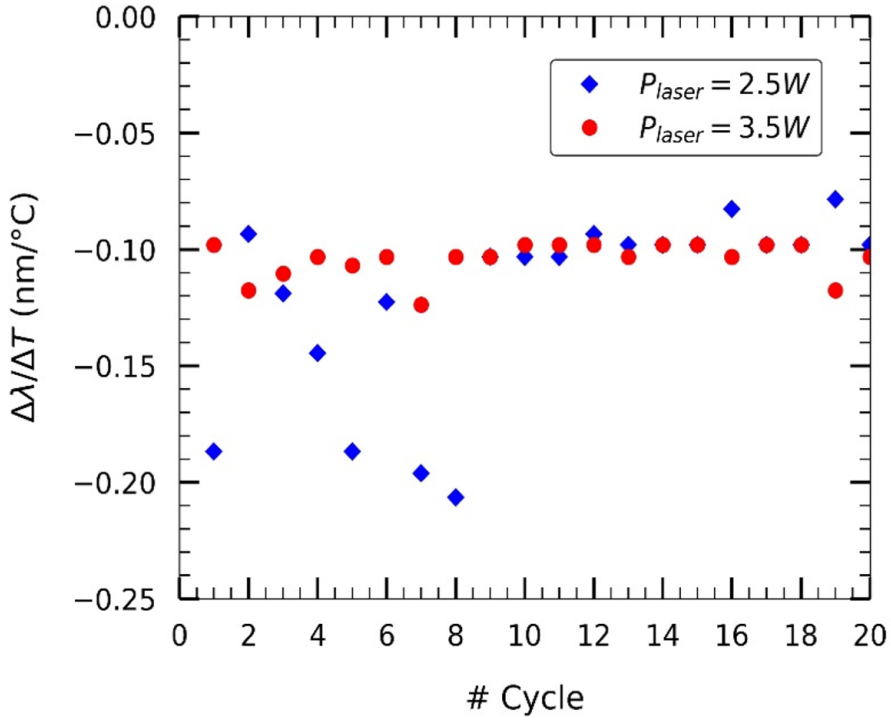

Figure 3.5: The influence of heating-cooling cycle number on thermal fluorescence coefficient is provided in terms of wavelength shift gradient for excitation laser power of 2.5W and 3.5W. Thermal fluorescence coefficients ($\Delta\lambda/\Delta$T) is derived from spectra counts (A.U.) from spectrometer. For 20 different heating-cooling cycles spanning over 30 days, uniform thermal fluorescence coefficient of -0.1 nm/°C is observed. Spectral intensity gradient regains after relaxation time of 48hrs at 10th thermal cycle.

These recombinations are enhanced by atom's same-direction vibration (optical phonon) and opposite-direction-vibration (acoustic phonon) in the unit cell. Because of these lower quantum yield and higher non-radiation recombination, the peak photoluminescence intensity of the 750nm QDs tends to decrease (from 2350 A.U. to 1650 A.U.) with a temperature increase from 26.0°C to 68°C (see Fig. 3.4). Moreover, it is evident from the same illustration that the peak emission intensity (for 750nm QDs) moves toward lower wavelength (blue-shift). This is mainly because of the interesting

Table 3.1: Influence of surface temperature on Photoluminescence (PL) peak intensity for dual quantum dot

$T_s(^\circ C)$	Intensity (750nm QD)	Intensity (550nm QD)
26	2350	1800
41	2100	1350
53	1940	1250
63	1800	1200
68	1650	1180

interplay between electron-phonon-renormalizations and thermal expansion. For all the semiconductors, the thermal expansion effect is assumed to be negligible and all the theoretical models are developed based on simplistic approach of electron-phonon interaction and that is how they show decreasing relationship of energy band with higher temperature (like Varshni's equation (Eq.3.1)) [60].

$$E_g = E_{g,o} - \frac{\alpha T^2}{T + \beta} \tag{3.1}$$

Here, α, β are the correlation constants. In contrast, in non-semiconductors, the thermal expansion has significant contribution to the phonon density of states. These phonon-density of states can be determined from corresponding vibration frequency (for example in our case, 'Cu-like, In-like, S-like' vibrations. Dey et al. investigates some using PbS nanocrystals (and mentioned about 'Pb-like', 'S-like' vibrations). They come up with a model that combines effect of thermal expansion and electron-phonon-renormalization on energy band gap. Surprisingly they found increasing trend of energy band gap (blue-shift) with higher temperatures for non-semiconductor nanocrystals which justifies our reasoning as well. Such blue-shift is quantified for twenty different thermal quenching cycles. Thermal photoluminescence co-efficient ($\frac{\Delta\lambda}{\Delta T}$) is from the peak intensity shift (blue-shift) and plotted against quenching cycles in Fig. 3.5. It is evident from Fig. 3.5 that the

system is highly stable since the photoluminescence coefficient remains uniform even at very high number of heating-cooling cycle. Thus these red/blue shifts play a significant role in determining this fluorescence technique's sustainability.

Applications

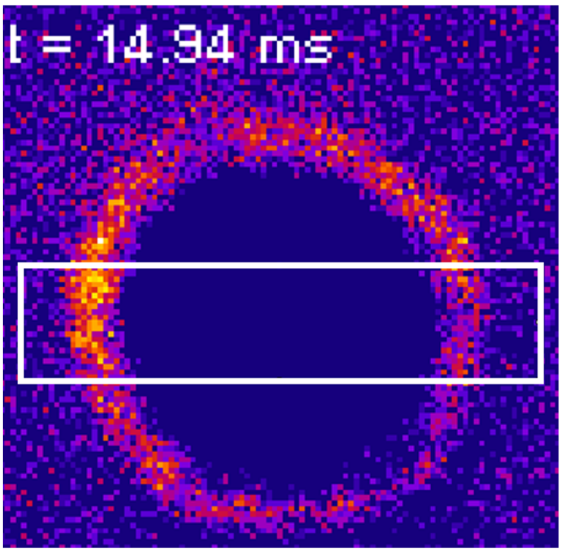

Figure 3.6: Applications of the thermal mapping technique: Surface temperature measurements during droplet impingement cooling at t = 14.94ms

Once the photoluminescence characterization is completed, the Phantom high speed camera replaces the optical fiber and captures the scanned Region of Interest (ROI) at 3000 fps and 23 μs shutter time. Greyscale values (GSV) from visible imagery from the HSV is further analyzed for different temperature levels (23°C to 101°C). During the calibration phase, the GSV information is only captured for heating and nature convection air-cooling. The QD coated paper is attached with the FTO/glass substrate (FTO side) (see Fig. 3.2). The FTO glass is ohmically heated until the global surface temperature (measured by thermocouple) reaches the steady state at 100°C. First, the temperature calibration is performed against PL intensity values. From the data extracted at

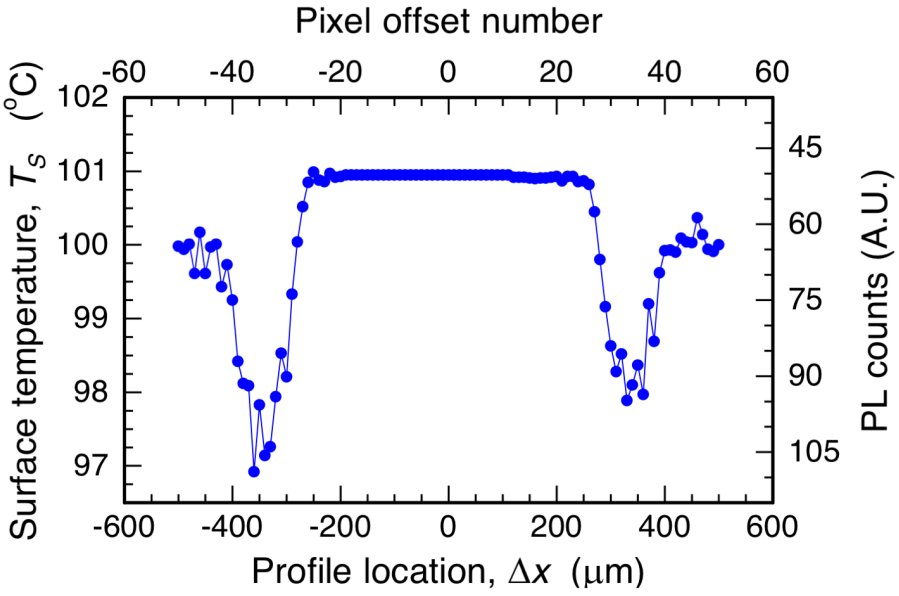

Figure 3.7: Local Photo Luminescence (PL) intensity and temperature profile through the midline (rectangular ROI in Fig. 3.6) of the water droplet

different temperature levels (see Table.1), a trend line is formed. Later, GSV values from the high speed camera is extracted for different surface temperature levels. Grey scale values are averaged over the number of pixels (inside the Region of Interest) for a corresponding temperature.

After the calibration is done, experiments are conducted on two different surfaces such as i) flat (for droplet impinging experiment), and ii) micropillared (for hemiwicking experiment) to test this mapping technique. Keeping the laser scanner and high speed camera 'ON', a micro droplet is dispensed on the QD coated paper (flat and micro pillared surfaces, separately). HSV captures the moments (from transient to steady) and data are post-processed to convert pixel-by-pixel GSV to pixel-by-pixel temperature values using calibration trend line (found from Fig. 3.4, and Table 1). As mentioned, to test this thermography technique, surface temperature during water droplet impingement cooling on a heated substrate (100°C) is captured and shown in Fig. 3.6 at t = 14.94ms. It is observed from the local temperature profile (in Fig. 3.7) through the midline of the droplet

that there is a 3°C interface cooling at the edge of the droplet with a relatively hotter temperature (101°C) at the core of the droplet.

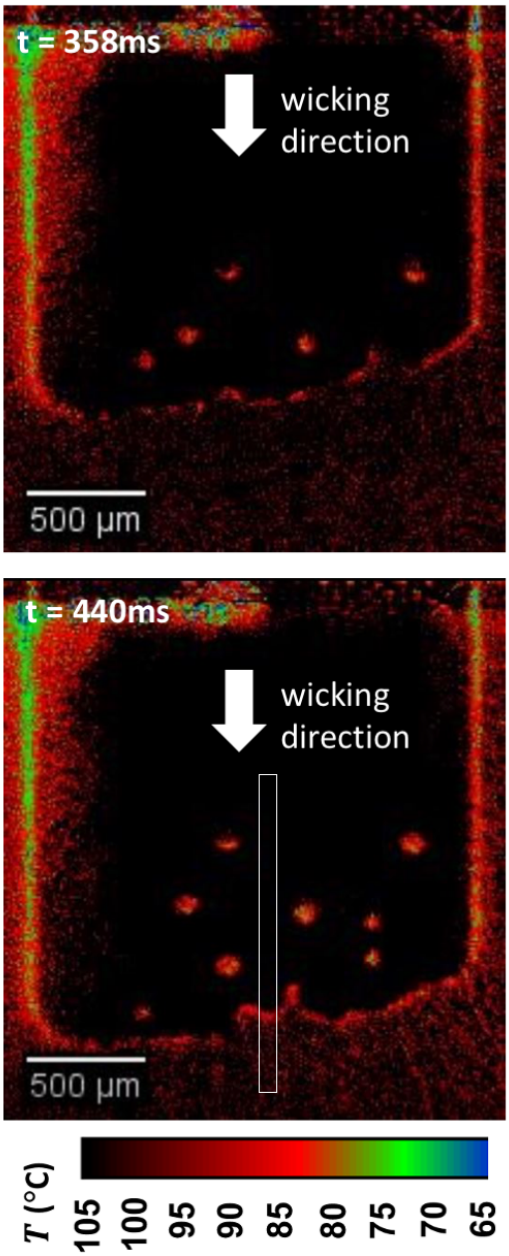

Figure 3.8: Applications of low-cost thermal mapping technique: temperature evaloution of the hemiwicking front at t= 358 ms and 440 ms

To further test the ability of this thermography technique to capture transient phenomena, thermal evolution during hemiwicking flows through anisotropic micro-pillared wicks is measured and shown in Fig. 3.8. Microstamping mechanism shown in Fig. 3.3 [1] is employed to create a plastic mold with micron scale holes. NOA is poured onto the holes and before starting the curing process inside UV chamber, QD-saturated paper is attached. Later, the NOA coated paper is peeled off from the mold carefully. Thus the anisotropic wicks are achieved which are shown as top-view in and stereo-view in Fig. 3.3. To facilitate the hemiwicking experiment, isopropanol droplet (25°C) is casted at the edge of the heated wicks (105°C). Due to gradient caused by the capillary force, the isopropanol film starts to propagate. Figure shows that hemiwicking front generates enormous cooling effect (105°C to 70°C) during such propagation on the heated substrate (105°C) at t = 358 ms and 440 ms. It is to be noted the non-uniforimty in thermal maps in left portions of both droplet impingement and hemiwicking are because of the non-uniform distribution of intensity.

This transient temperature changes very interestingly as it wicks the surface. Fig. 3.9 shows local surface temperature profile and PL counts at midline of the hemiwicking surface (along the wicking direction). This pixel-by-pixel thermal information can be used to get wicking front speed by implementing the thermal and momentum diffusion at the solid-liquid interface. On dynamics of hemiwicking, Kim [61] provided a scaling relation stated below-

$$L\alpha\sqrt{\frac{\gamma\eta ht}{\mu}} \tag{3.2}$$

Here, L, γ, η, h, t, μ are wicking front distance, surface tension, generalized coefficient, wicking micro-pillar height, and time-elapsed, respectively. Whereas, Choi et al. [62] provided insights about fluid refreshing through these hemiwicking surface can augment Critical Heat Flux (CHF) by 100%. Therefore, the transient thermal information of hemiwicking surface, given by this

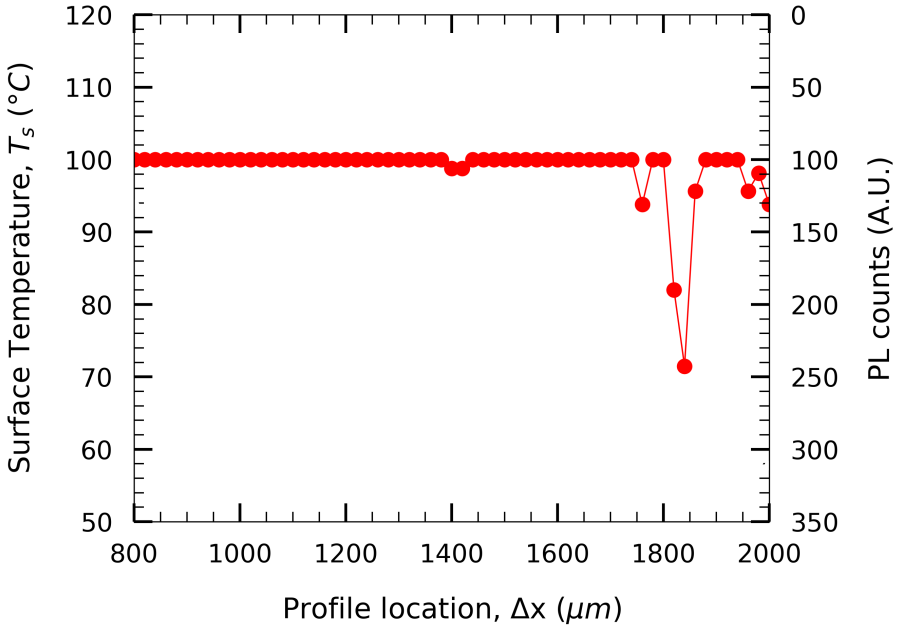

Figure 3.9: Local Photo Luminescence (PL) intensity and temperature profile through the midline (rectangular ROI in Fig. 3.8) of the hemiwicking surface

novel thermal mapping technique, will provide important design guidelines (geometry and fluid properties) to fabricate future generation thermal management technologies such that it can handle high heat fluxes.

Summary

This chapter introduces a novel technique to design and fabricate a thermal sensor using $CuInS_2$/ZnS quantum dots (5-10nm, in diameters) loaded ceramic nanoporous membrane or everyday use paper. A low-cost and effective dip-coating and/or drop casting technique is employed to achieve uniform thin film of quantum dots. Spectral information is captured while a excitation laser scans the quantum dotted interface at frequencies of 133 Hz (axial) and 533 Hz (longitudinal). Thermal characterization experiments reveal the sensor's capability to capture thermal information with

a sustained thermo-photoluminescence coefficent of -0.1nm/°C. Moreover, the thermal quenching trials ensure higher order stability of such interface even at higher number of thermal cycles with intermittent thermal relaxation events. Finally, this thermal mapping technique is employed to perform thermal mesurements during droplet impingement cooling and hemiwicking flows on anisotropic micropillared surface. With such spatio-temporal benefits, this low-cost mapping technique can be used to capture useful thermal information during transient cooling in micron-sized and even nano-sized electronic devices, especially at high thermal loads. But, in such nanoscale systems, capturing heat transfer enhancements can be difficult as it needs rigorous fundamental understanding. To generate such understanding, a coupled analytical-numerical model is proposed in Chapter 4 to predict the effect of conduction, convection, and radiation of heat transfer enhancements in nanoparticle suspensions.

CHAPTER 4: NANOSCALE HEAT TRANSFER ENHANCEMENTS

This chapter is from the publication (in-preparation) below by Rabbi and Putnam (2021):
Khan Md. Rabbi and Shawn A Putnam. Combined roles of conduction, convection and radiation for heat transfer enhancements in nanoparticle suspension.

Literature Review

The inclusion of nanoparticles in conventional liquids and solids has inspired noteworthy attention in a broad range of scientific disciplines. In particular, nanofluids (e.g., a suspension of nanoparticles in a fluid) have stirred much debate and excitement in the last two decades. Can one simply replace a conventional fluid/coolant with a stable nanofluid to enhance the cooling performance of a heat exchanger? Before this question is addressed, let us first consider that in the last decade alone, thousands of numerical and experimental investigations have been conducted to identify effects of adding nanoparticles to a fluid/coolant for effectively increasing the fluid's thermal properties – as indicated in the recent benchmark studies [63]. In general, many of these studies suggest quite promising results. For example, Heris et al. [64] experimentally showed that significant heat transfer enhancements could be achieved with CuO and Al_2O_3 nanofluids in the laminar flow heat transfer regime. And Fotukian et al. [65] experimentally observed a 25% heat transfer enhancement by sacrificing a 20% increase in pressure drop with CuO nanofluids in a turbulent flow heat transfer regime. Moreover, Arani et al. [66] experimentally showed that better thermal performance with comparatively less pressure drop is possible with 20 nm in diameter TiO_2 nanofluids. Thus, based on these results and many others[67, 68, 69, 70, 71], nanofluid suspensions – if stable – could potentially outperform their non-nanoparticle counterparts. With this said, no known, commercially available, single- or two-phase heat exchanger currently takes advantage of the po-

tentially enhanced thermal properties of a nanofluid.

Numerous articles [67, 68, 69, 70, 71] are available that review the 'thermal' benefits of nanofluids. However, there is still much controversy on nanofluids - especially from an industrial perspective.[72] For example, from a practical point of view, it is arguably impossible to synthesize stable nanofluids at high concentrations because of the irreversible effects coupled with particle settling, flocculation, and erosion. Moreover, even if moderately stable and resilient nanofluids can be synthesized, such nanofluids will induce more frequent system maintenance and the need for increased pumping powers in a cooling cycle. In principle, such a stable and resilient nanofluid could have technical benefits in a thermal transport system – analogous to the established nonlinear optical effects via nanoparticles and nanostructures in photonics devices based on metamaterial designs, near-field radiation, and enhanced plasmonic effects. With this said, from a thermal transport theory perspective, the roles of micro-/nano-convection, interfacial conductance, and radiative heat transfer in a nanofluid are far from being established. Of particular interests are the potentially overlooked thermal contributions due to near-field radiation.[73] Recently Domingues et al. [74] numerically investigated heat transfer between two spherical nanoparticles in a near-field configuration. Using a Molecular Dynamics (MD) technique, a thermal conductance model is developed to estimate the enhanced heat transfer rate between nanoparticles at nanometer to micrometer distances. Volz et al. [75] also recently studied the near-field interactions in a composite system including nanoparticles. It is found that even at very low nanoparticle concentrations (ϕ = 0.033), radiation contribution to effective thermal conductivity showed to be significantly large (e.g. thermal conductivity enhancements up to 35% at loadings of only 1% by volume).

This chapter reports a traditional theory-based calculation of the radiation contribution to heat transfer of Al_2O_3 nanoparticles dispersed in water. The approach also incorporates both the interfacial thermal resistance at the fluid-particle interface and the potential for micro-/nano-convection. Using similarity theory based on traditional hydrodynamic and thermal boundary layer approxi-

mations, the resulting radiative enhancements are encapsulated in terms of both the effective enhancement in the thermal conductivity and the effective enhancement in the heat transfer coefficient (HTC) with nanoparticle loadings up to $\phi = 0.05$ (5 vol%).

Discussion

Heat transfer characteristics of nanoparticle suspensions can be effected by different factors. Researchers have developed different thermal conductivity models to capture the effects of Brownian motion [76, 77], nanoclustering [78, 79], monolayering [80, 81] etc. Among all these models, Maxwell's classical model [82] based on Effective Medium Theory showed promise because of its proven applicability.

Effective Medium Theory

In the light of small nanoparticles, the interface between a nanoparticle and the base fluid plays a vital role in controlling the overall thermal transport. The intrinsic interfacial thermal resistance (or finite interfacial thermal conductance) at the particle-fluid interface can be accounted for effective medium theory.[83] Eq. 4.1 shows the predicted thermal conductivity of a nanofluid (k_ϕ) for a sufficiently small nanoparticle loading ($\phi << 1\%$) and a finite interfacial thermal conductance at the particle-fluid interface:

$$k_\phi = k_0 \left[1 + 3\phi \frac{k_p(\gamma - 1) - \gamma k_0}{k_p(\gamma + 2) + 2\gamma k_0}\right], \tag{4.1}$$

where k_0 is the thermal conductivity of the base fluid, k_p is the thermal conductivity of the nanoparticle, $\gamma = rG/k_0$, r is the radius of the solid nanoparticle, and G is the interfacial thermal conductance at the particle-fluid interface. In the support of the applicability of Eq. 4.1, past studies [83]

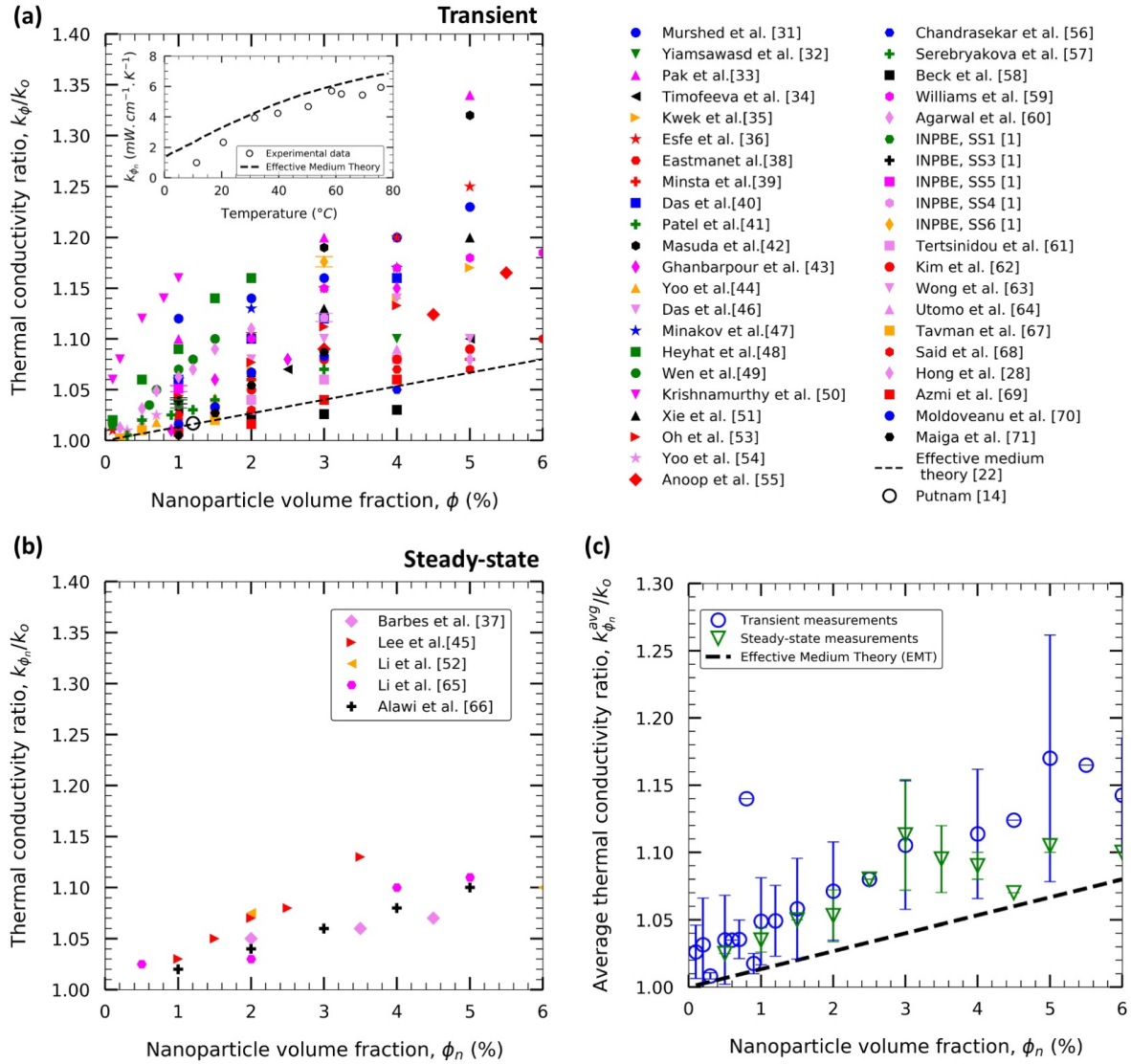

Figure 4.1: Thermal conductivity enhancement ratio (k_ϕ/k_0) for Al_2O_3 nanoparticle suspensions as a function of loading fraction, where the symbols represent data from the literature and the dashed line is that predicted by Effective Medium Theory (EMT) assuming $k_p/k_0 >> 1000$ and interfacial conductance $G \to \infty$ measured by a) transient and b) steady state techniques; c) average thermal conductivity values using these two measurement techniques and comparison with predictions by Effective Medium Theory (EMT). The inset figure shows the comparison between the measured [2] and predicted thermal conductivity of a Al_2O_3 nanofluid as a function of temperature ($\phi \approx 1.1$ vol%).

showed that the thermal conductivity of solid-solid nanocomposite (k_c) is very sensitive to both G and the particle size (r), where k_c would increase or decrease relative to k_0 for $r > 7$ nm and $r < 7$ nm, respectively.

Fig. 4.1 summarizes the particle loading trends and variations in experimental data for the thermal conductivity of Al_2O_3 nanofluids. As shown in Fig. 4.1 the inclusion of Al_2O_3 nanoparticles is frequently reported to enhance the thermal conductivity of a nanofluid – in fact, in some cases by as much as 25% at a nanoparticle loading of only 5 vol%. Also, included in Fig. 4.1 are the upper-limit predictions of effective medium theory (EMT) - i.e., the dashed lines are EMT predictions assuming that Al_2O_3 nanoparticles have an average thermal conductivity greater than diamond ($k_p >> 1000$ W/m·K) and that the interfacial thermal resistance (R_{int}) at the particle-fluid interface is effectively zero ($1/R_{int} = G \rightarrow \infty$). As depicted in Fig. 4.1, nearly all the experimental results are in complete disagreement with EMT – even with EMT predictions using exaggerated nanoparticle thermal conductivities ($k_p/k_0 >> 1000$) and interfacial thermal conductances ($G \rightarrow \infty$). Additionally, the influence of temperature on thermal conductivity, measured experimentally, is presented in Fig. 4.1a (inset) for $\phi \approx 1.1$ vol%. Essentially, here Fig. 4.1a and Fig. 4.1b show experimental thermal conductivity measurements for transient and steady-state cases, respectively. Transient measurements are very common for thermal conductivity measurements for metallic nanoparticle suspensions, hence more data are available for this case and the number of experiments conducted using steady-state methods has remained conserved. However, questions arise whether convective current and thermal wave effect of hyperbolic heat conduction have any effect in larger thermal conductivity values for Alumina nanoparticle suspension in transient case. For these reasons, steady-state thermal conductivity measurements with reasonable uncertainty values are considered for this investigation. In fact, the experimental data for thermal conductivity measurement contain uncertainty levels ranging from 1.23% to 5%. For a better understanding, the uncertainty values in thermal conductivity measurements (both transient and

Table 4.1: Uncertainties of thermal conductivity measurements

Methods	**References**	**Claimed uncertainty (%)**
Transient (Hot wire)	31-36, 38-39, 42, 44, 47-49, 51, 54 - 64, 68, 70-71	1.23 - 5
Transient (Temperature oscillation)	40-41, 46	3 - 5
Transient (Place source)	43	2.5
Transient (3 Omega)	14, 53, 67	2 - 3
Steady-state (Coaxial cylinder)	37, 52, 65, 67	1.5 - 3

steady-state) are mentioned in the Table 4.1 with appropriate references. It is important to understand how the thermal conductivity values measured by two techniques correlates with Effective Medium Theory (EMT) predictions. As seen in Fig. 4.1c, the average thermal conductivity values found from the literature are inclined to EMT predictions where measurements by steady-state techniques show a better match compared to data using transient techniques.

Boundary Layer Approximation

To predict the heat transfer enhancements in terms of the heat transfer coefficient (HTC) of a nanofluid (h_ϕ) both the thermal conductivity of the nanofluid (k_ϕ) and the thermal boundary layer thickness (δ_{th}) must be understood for different nanoparticle loadings. These two thermofluid parameters are important because, in essence, all theory for convective heat transfer phenomenon reduces to a spatiotemporal heat transfer coefficient of the form: $h = k_{\text{eff}}/\delta_{th}$.[50]. The HTC encapsulates the unique coupling between the fluid flow-field and the temperature-field. To investigate this complex heat and mass transfer problem with potential radiation contributions between the nanoparticles, a similarity solution approach is employed for steady-state boundary layer flow. This similarity solution approach allows for simplifying the non-linear Partial Differential Equations (PDEs) for momentum and energy conservation to non-dimensional Ordinary Differential Equations (ODEs). These simplified governing equations for both the flow-field $f(\eta)$ and the

temperature-field $\theta(\eta)$ are

$$f''' + \frac{1}{2} f f'' = 0, \tag{4.2}$$

and

$$\theta'' = -\left[\frac{1}{2}\theta'(f + \eta f') + \xi \frac{\partial q(\tau, \xi)}{\partial \tau}\right] \mathrm{Pr}, \tag{4.3}$$

where $\eta = y(\frac{u_\infty}{\nu_0 x})^{1/2}$ represents the dimensionless similarity variable, y represents spatial displacements normal to the wall (y-axis), $\xi = x\frac{4\varepsilon_\infty \sigma T^3 \alpha}{(\rho c_p)_\phi u_\infty}$ is the nondimensional axial location, $\varepsilon_\infty \approx n^2$ is the dielectric constant of the fluid at optical frequencies, $\mathrm{Pr} = \nu_\phi / D_{th}^\phi$ is the corresponding Prandtl number for the nanofluid, u_∞ is far-field flow velocity, $\nu_\phi = \frac{\mu_\phi}{\rho_\phi}$ and $D_{th}^\phi = \frac{k_\phi}{(\rho c_p)_\phi}$ are the nanofluids' momentum diffusivity and thermal diffusivity, respectively and μ_ϕ and ρ_ϕ are dynamic viscosity and density of the nanofluid, respectively. The term for the dimensionless heat flux gradient $\partial q / \partial \tau$ in temperature-field equation (Eq.4.3) accounts for radiation in the participating nanofluid [84, 85] and can be explicitly written as:

$$\frac{\partial q(\tau, \xi)}{\partial \tau} = \left[(4\theta - 4) + \frac{1}{2}\epsilon(1 - \theta_w^4)\right], \tag{4.4}$$

where θ_w is the dimensionless wall temperature, ϵ is the thermal emissivity and τ is the optical path length. The corresponding boundary conditions for these similarity flow-field (momentum) and thermal-field (energy) conservation equations are

$$f(0) = 0, \quad f'(0) = 0, \quad f'(\infty) = 1, \tag{4.5}$$

and

$$\theta(0) = \theta_w = \frac{T_w}{T_\infty} = 2, \quad \theta(\infty) = 1, \tag{4.6}$$

respectively.[86]

All these boundary layer flow equations are for the limit of a thin thermal boundary layer – both hydrodynamically ($\delta_{th} << \delta_h$) and optically ($\delta_{th} \leq l_\alpha^{\mathrm{IR}}$). Here, δ_{th} ,δ_h and l_α^{IR} signify thermal boundary layer thickness, hydrodynamic boundary layer thickness and skin-depth at infrared frequency, respectively. The corresponding dimensionless optical path length for a thin thermal boundary layer in a participating medium [85] can be approximated as:

$$\tau = 5\sqrt{\xi N_{cr}\mathrm{Pr}}, \quad N_{cr} = \frac{k_\phi \alpha}{4\sigma T_w^3}, \tag{4.7}$$

where $T_w \approx 600$K, and $T_\infty \approx 300$K are the approximated hot-spot wall temperature, and ambient temperature, respectively. $\sigma = 5.67 \times 10^{-8}$ W m^{-2} K^{-4} is Stephan-Boltzmann constant, and $\alpha \approx \frac{4\pi}{\lambda_{\max}}[(1-\phi)\kappa_0 + \phi\kappa_p]$ is the optical absorption coefficient of the nanofluid. It is to be noted that T_w = 600 K temperature is unrealistic and that the effects of other wall temperatures are suggested for future comparative studies. Essentially, a practical wall temperature will be between 20°C-50°C [87, 88, 89] as per actual applications. The corresponding optical extinction coefficients for the base fluid (water: $\kappa_0 \approx 0.04$) and nanoparticles (Al_2O_3: $\kappa_0 \approx 0.08$) reflect literature values at the peak radiation wavelength ($\lambda_{\max} \approx 4.3\mu$m) via Wien's displacement law ($\lambda_{\max} T_w \approx 2900$ μm·K). The N_{cr} parameter in Eq. (4.7) corresponds to the ratio of the mean-free-path for conduction (i.e., $\Lambda_{\mathrm{mfp}}^{(c)} \propto k$) to the mean-free-path for radiation (i.e., $\Lambda_{\mathrm{mfp}}^{(r)} \propto 1/\alpha$), where for $N_{cr} > 10$ the heat-conduction process dominates. In this regard, if the nanofluid is optically opaque between adjacent nanoparticles (i.e., $\alpha d > 1$) or within the thermal boundary layer (i.e., $\alpha\delta_{th} > 1$), then heat transfer by radiation can be neglected. However, for an aqueous Al_2O_3 nanofluid $l_\alpha = \tau/\alpha \approx 1.5$ mm; therefore, both $l_\alpha/d >> 1$ and $l_\alpha/\delta_{th} >> 1$ are satisfied.

To simultaneously solve this set of non-linear ODEs, the numerical shooting method is used with code written in Python. This shooting method uses the following 'flow-shooting' variables (x_1, x_2,

x_3) for the non-dimensional flow-field (Eq.(4.2)):

$$x_1 = f,\ \ x_2 = f',\ \ x_3 = f'',$$
$$x_1' = x_2,\ \ x_2' = x_3,\ \ x_3' = -\tfrac{1}{2}x_1 x_3, \tag{4.8}$$

where the corresponding 'flow-boundary' conditions (Eq.(4.5)) are

$$x_1(0) = 0,\ \ x_1'(0) = 0,\ \ x_1'(\infty) = 1. \tag{4.9}$$

Whereas, the simultaneously solved 'thermal-shooting' variables (y_1, y_2) for the non-dimensional temperature-field (Eq.(4.3)) are

$$y_1 = \theta,\ \ y_2 = \theta',$$
$$y_1' = y_2,\ \ y_2' = -\left[\tfrac{1}{2}y_2(f + \eta f') + \xi\tfrac{\partial q(\tau,\xi)}{\partial \tau}\right]\mathrm{Pr}, \tag{4.10}$$

with corresponding 'thermal-boundary' conditions (Eq.(4.6)) of

$$y_1(\infty) = 1,\ \ y_1(0) = \theta_w = 2. \tag{4.11}$$

Figure 4.2 shows the resulting thermal boundary layer profiles for increasing nanoparticle loadings in the thin thermal boundary layer limit (i.e., $\delta_{th} << \delta_h$ and $\delta_{th} \leq l_{\alpha}^{\mathrm{IR}}$)[85]. As illustrated in Fig. 4.2, increment in nanoparticle concentration (ϕ) induces systematic reductions in the thermal boundary layer thickness (δ_{th}) with the corresponding increases in the wall heat flux ($d\theta(\eta)/d\eta|_{y=0}$). These temperature profiles in Fig. 4.2 are then used to resolve the predicted enhancements in the heat transfer coefficient for different nanoparticle loadings via $h_\phi = k_\phi/\delta_{th}$ with

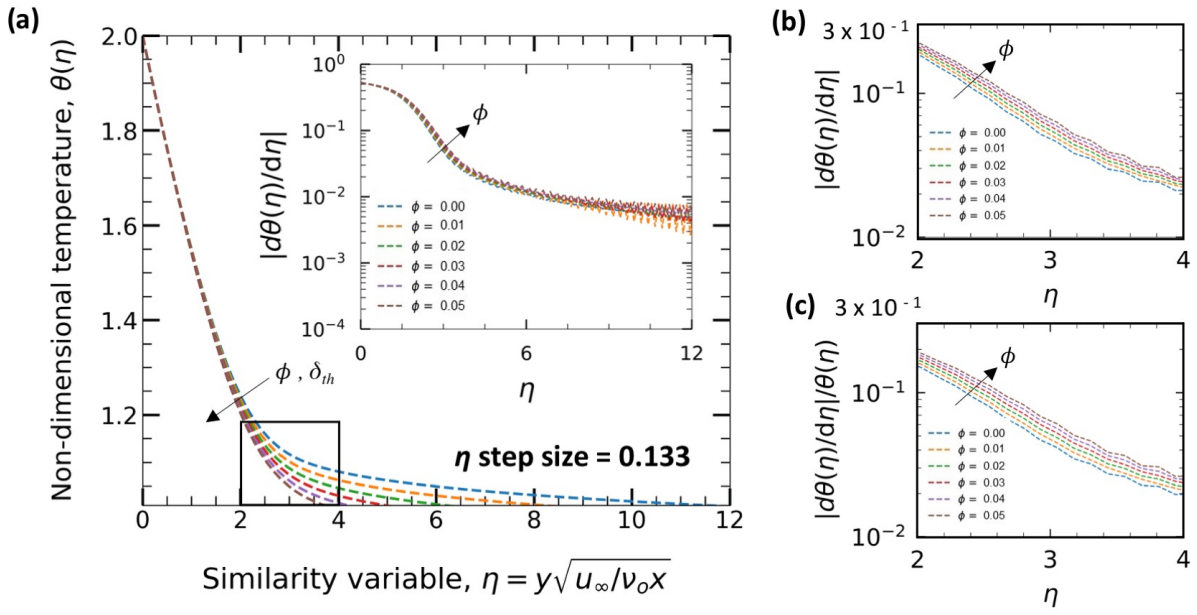

Figure 4.2: a) Variation of thermal profile with nanoparticle loading in optically thin medium, b) change in slope from nanoparticle volume fraction 0% to 5% (for η = 2 - 4) , and c) normalized change in slope from nanoparticle volume fraction 0% to 5% (for η = 2 - 4) at η step size of 0.133. Temperature profile, change in slope and normalized change in slope for η step size of 0.167, 0.14, 0.1307 are shown in supplemental Figs. 1-3, respectively.

k_ϕ calculated with EMT (Eq.4.1) and δ_{th} based on the asymptotic limit of the calculated temperature profiles (i.e., $\delta_{th,\phi} = \eta_\phi/(\frac{u_\infty}{\nu_0 x})^{1/2}$ when $\theta(\eta_\phi) \approx 0.95\ \theta_w$). Temperature profile, change in slope and normalized change in slope for different step sizes of η are illustrated in the appendix.

Radiation Contribution

To better quantify the effects of radiation between the dispersed nanoparticles in the fluid, geometrical view-factors for adjacent spherical nanoparticle are used to estimate the relative enhancements ($\uparrow$) in both the thermal conductivity ($k_\phi^{\text{eff}} = k_0 + k^\uparrow$) and the HTC ($h_\phi^{\text{eff}} = h_0 + h^\uparrow$) of the nanofluid. Although the agglomeration and sedimentation in nanoparticle suspension have effects on the ther-

mal conductivity [90, 91], the ideal, uniform distribution, which mimics a spatiotemporal averaged distribution of a well dispersed / non- flocculating nanoparticle suspension are assumed. Figs. 4.4 illustrates the implemented (idealized) nanoparticle distribution to account for the coupled radiation heat transfer between neighboring 2D planes of spherical nanoparticles, where each plane of nanoparticles has a unique temperature for a 1D thermal gradient. Eq.4.12 is the corresponding view-factor for two adjacent nanoparticles:[92]

$$F_{12} = \left[1 - \sqrt{1 - \left(\frac{1}{\chi + 2}\right)^2}\right]^2 \times (\chi + 2)^2, \tag{4.12}$$

where χ represents the dimensionless edge-to-edge distance between two adjacent nanoparticles. This view-factor is then used to calculate the corresponding multi-particle view-factor for ideal planes of symmetrically distributed nanoparticles (see, Fig. 4.4). Thus, the resultant view-factor for a series of closely-packed nanoparticles per unit volume is

$$F_{12}^{*} = \sum_{j=-a}^{j=a} \sum_{i=-a}^{i=a} \left[1 - \sqrt{1 - \left(\frac{1}{\Gamma_{ij}/Z_{\parallel}}\right)^2}\right]^2 \times \left(\frac{\Gamma_{ij}}{Z_{\parallel}}\right)^2, \tag{4.13}$$

where $Z = 1/d^3$ is the number of nanoparticles per unit volume, $Z_{\parallel} = 1/d$ is the number of planes per unit volume, $a = (\frac{Z}{4Z_{\parallel}})^{1/2}$ is the summation limit over the unit cell, and $\Gamma_{ij}^2 = i^2 + j^2 + 1$ signifies a planar geometric series.

Table 4.2 provides the corresponding view-factors for different nanoparticle loadings. The nanoparticles become more closely packed at increased nanoparticle loadings; thus, as the distance ($d = (3\phi/4\pi r^3)^{-1/3}$) between nanoparticles increases (or ϕ decreases), the total view-factor and radiative heat transfer between nanoparticles decreases. The effective heat transfer coefficient due to radiation is: $h_{rad,F_{12}^{*}}^{\uparrow} = 4\epsilon\sigma T_{avg}^3 \times F_{12}^{*}$.

Table 4.2: Coupling between a nanofluid's volume fraction ϕ, nanoparticle size, r = 5×10^{-9}m, interparticle distance (d) number of nanopartilces per unit volume Z, and idealized view-factor F_{12}^{*} for radiative heat transfer in a transparent media.

$\phi(\%)$	$d(m)$	$\chi = \frac{d}{r}$	$Z(1/m^3)$	F_{12}^{*}
1.0	3.74×10^{-8}	7.48	19098548	0.00279
2.0	2.96×10^{-8}	5.93	38197097	0.00399
3.0	2.59×10^{-8}	5.18	57295645	0.00488
4.0	2.35×10^{-8}	4.71	76394194	0.00560
5.0	2.18×10^{-8}	4.37	95492742	0.00622

Sensitivity analysis

Sensitivity analysis of the numerical solution (Eqns.4.1-4.13) is performed to both (1) define the minimum number grid elements and (2) summarize the sensitivity of the numerical solution due to differential changes in key model variables (and/or thermofluid properties). Fig. 4.3 illustrates the sensitivity (S_β) of the simulated thermal boundary layer thickness (δ_{th}) due to differential changes in $\beta = [\phi, \epsilon, \xi]$ as a function of the simulated grid/step size. The sensitivity analysis is performed on δ_{th} because of its fundamental importance in all thermofluid heat and mass transport phenomena (e.g., $h \propto 1/\delta_{th}$). Fig. 4.3 shows the inconsistency in the numerical solution for grid element numbers less than 1500. However, for grid element numbers $\geq$ 1500 the numerical results are insensitive to increases in the number of grid elements. Most importantly, as shown in Fig. 4.3 for grid elements $\geq$ 1500, the thermal boundary layer thickness (δ_{th}) is most sensitive to changes in nanoparticle loading (ϕ), whereas δ_{th} is rather insensitive to changes in ϵ and ξ. Based on these results, all subsequent discussions of numerical results are based on simulations using a grid element number of 1800 (see, vertical dashed-line in Fig. 4.3).

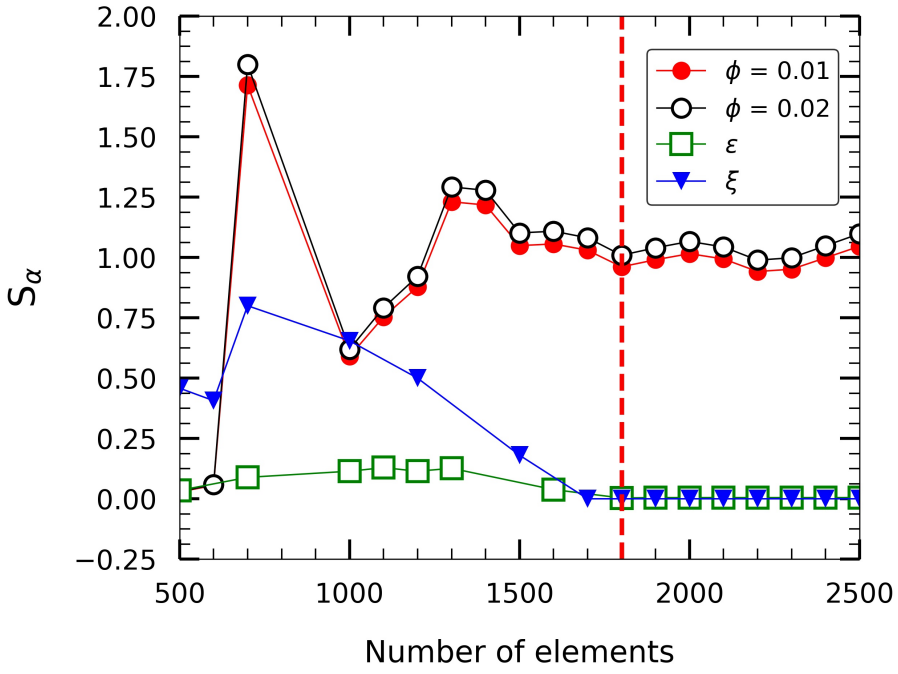

Figure 4.3: Sensitivity of the thermal boundary thickness (δ_{th}) as a function of grid element number: $S_\beta = \frac{\partial \ln \delta_{th}}{\partial \ln \beta} = \frac{\beta}{\delta_{th}} \frac{\partial \delta_{th}}{\partial \beta}$, where $\beta = \phi, \epsilon, \xi$. The dashed-red vertical line indicates the grid element condition used for the analysis.

Thermal Conductivity Analysis

Fig. 4.5 shows that the effective thermal conductivity of the nanofluid increases ≈3% for every 1% increase in nanoparticle loading. The effective medium theory predicts that the largest possible increase in k_ϕ of a nanofluid loaded by a volume fraction $\phi << 1$ of spherical particles will be $3\phi k_0$ (assuming $G \rightarrow \infty$ – rather than the finite interfacial thermal conductance $G = 300$ MW/m^2·K used here). Radiation component ($k^{\uparrow}_{rad}$) is achieved by incorporating $k^{\uparrow}_{rad} = \frac{16}{3} n_r^2 \Lambda^{(r)}_{\text{mfp}} \epsilon \sigma T^3_{avg} F_{12*}$ [93] and adding the component to the thermal conductivity predicted by Effective Medium Theory (k_{EMT}). It is shown that the trend of radiative contribution maintains a linear relationship for variety of nanoparticle loading (1% to 5%, by volume). As it can be seen from the figure, thermal conductivity is enhanced by 2% (for emissivity, ϵ = 0.5), 3.5% (ϵ = 0.6), 5% (ϵ = 0.7) for every

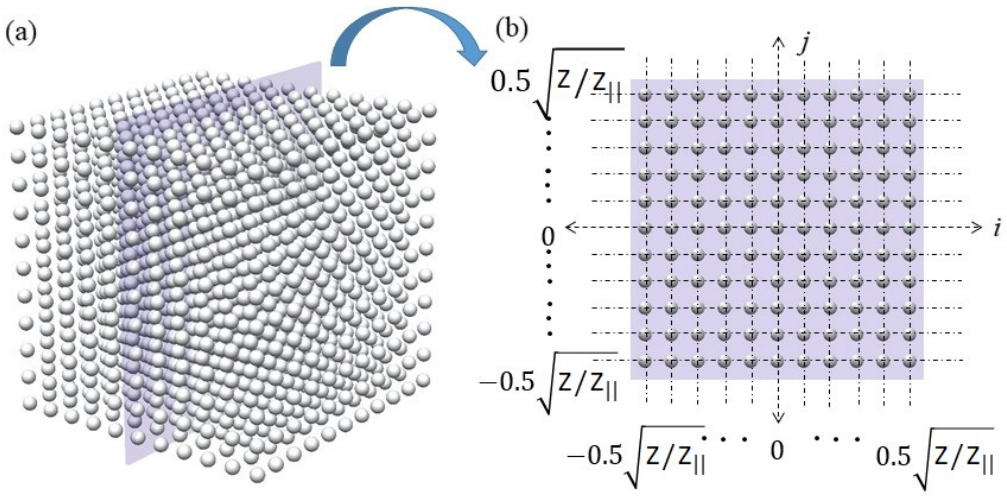

Figure 4.4: Geometrical view-factor configuration for (a) the idealized nanoparticle distribution matrix in 3D, and (b) the corresponding nanoparticle distribution over a plane.

1% (by volume) nanoparticle loading into the system. However, with a realistic wall-temperature (e.g., 20°C-50°C [87, 88, 89]), such radiation contribution to effective thermal conductivity will be close to zero. For instance, if the temperature is set to 50°C (323K), the thermal conductivity will be enhanced by 0.31% (for emissivity, ϵ = 0.5), 0.55% (ϵ = 0.6), 0.78% (ϵ = 0.7) for every 1% (by volume) nanoparticle loading. Yet, as illustrated in Fig.4.5, the predicted trend for the effective thermal conductivity ratio enhancement – accounting for conduction, convection, and radiation (i.e., $k_{\phi}^{eff} = k_{cond}^{EMT} + k_{rad}^{\uparrow}$) correlates surprisingly well with the averaged experimental results from multiple studies of aqueous Al_2O_3 nanofluids [94, 95, 96, 97, 98, 99, 100, 101, 102, 103, 104, 105, 106, 107, 108, 109, 110, 111, 112, 113, 114, 115, 116, 117, 118, 119, 120, 121, 122, 123, 124, 125, 126, 127, 128, 129, 130, 131, 91, 132, 133, 134]. While selecting these experimental data from published and well-cited literature, high-thermal-conductivity enhancement data are also included and the selection criteria is discussed in the supplemental materials. Such anomalous enhancements of thermal conductivity depends on measurement technology and flow conditions during such measurements [135]. For instance, the low thermal enhancement can be due

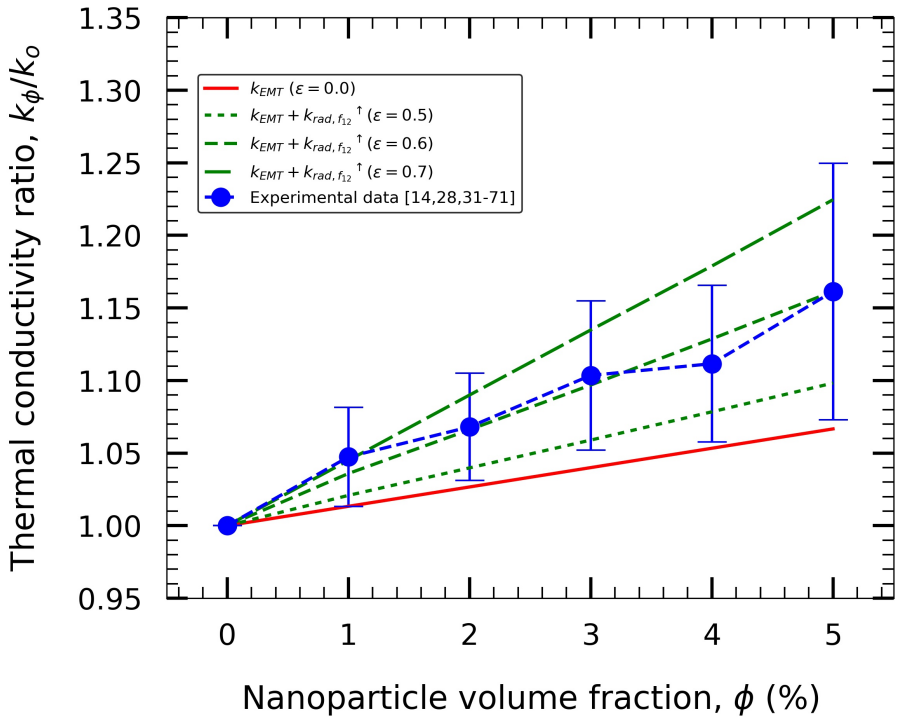

Figure 4.5: Combined roles of conduction, convection, and radiation on enhancement in the thermal conductivity of an aqueous Al_2O_3 nanofluid for different particle loadings. Here,the experimental data, marked by blue circular closed symbols, are the combined data of transient and steady-state measurement cases illustrated in Fig. 4.1c.

to stationary condition of nanosuspension, and higher solid-liquid interfacial thermal resistance. In other words, while measuring the thermal conductivities of nanosuspensions using any transient methods in non-stationary nanofluids, anomalous enhancements in effective thermal conductivity are expected [136, 68].

In more recent work, Hasselman [137] investigated on whether the temperature dependent heat transfer coefficient has any contribution to such anomalous enhancements. While measuring thermal conductivity using most popular measurement technique, transient hot-wire, the investigator concluded that temperature had a positive influence on energy exchange during nanoparticle collisions. This, certainly, resulted in smaller resistances at particle-fluid interface and higher thermal

conductivity values. In a commentary article, Assael et al. [138] agreed that they also observed the influence of temperature discontinuity at the particle-fluid interface but argued whether such anomalous enhancement are due to other mechanism like Brownian motions. However, during forced convections in real-life applications, nanoparticle's velocity is believed to be far greater than the order of magnitude of Brownian motion [139]. Sobamowo [140] recently observed how this temperature of nanofluid can effectively be influenced by thermal radiation and effectively enhance the thermal conductivity [75]. In fact, in this study, the alignment between the experimental thermal conductivity ratio data and the predicted radiative trends (at emissivity of 0.6 and 0.7) justifies such understanding. It is further observed that, even for relatively moderate nanoparticle loading of 3%, the thermal conductivity enhancement increases from 3% to 14%. It is also noteworthy that nanosuspension with lower nanoparticle loading (say, 1%, by volume) can still be benefited by optical transparency and thin thermal boundary layer developed in hot-spot cooling configuration if nanoparticles, loaded in the suspension, are of sufficiently high emissivity ($\epsilon \leq$ 0.7).

Heat Transfer Coefficient Analysis

Fig. 4.6 shows the predicted enhancements in the heat transfer coefficient ratio (h_ϕ/h_0) due to both enhanced thermal conduction ($k_p > k_0$) and radiation ($k^{\uparrow}_{rad,F^*_{12}}$) inside the thermal boundary layer of an advecting nanofluid. Here, h_ϕ and h_0 denote the heat transfer coefficients for nanofluid and basefluid, respectively. And, the h_0 is calculated from $h_0 = k_0/\delta_{th}$ where, the thermal boundary layer thickness (δ_{th}) is found from the simulations discussed in section 2.2. The heat transfer coefficient in accordance with the thermal conductivity predictions by Effective Medium Theory ($h^{\uparrow}_{EMT} = k^{\uparrow}_{EMT}/\delta_{th,q=0}$) increases by 20% for every 1vol% of nanoparticle where $\delta_{th,q=0}$ indicates the thermal boundary layer thickness without radiative transport. Considering radiation heat transfer coupled in boundary layer flow, heat transfer coefficient ($h^{\uparrow}_{rad,q} = k^{\uparrow}_{EMT}/\delta_{th,q\neq 0}$) increases

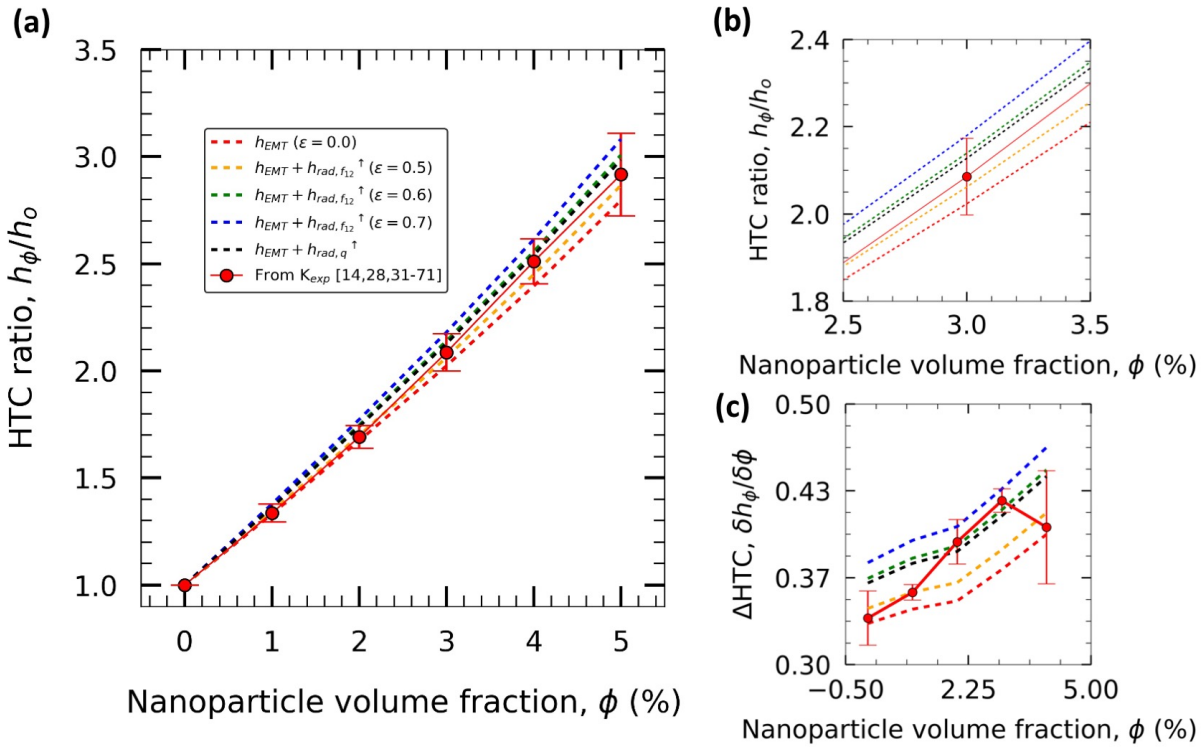

Figure 4.6: Effect of Al_2O_3 nanoparticle volume fraction on heat transfer coefficient (HTC) inside thin thermal boundary layer. Here, the red circular HTC ratio data-points are calculated by K_{exp}/δ_{th}, where K_{exp} and δ_{th} represent experiemental thermal conductivity data from the literature and thermal boundary layer thickness from the simulation, respectively.

by 23% for every 1% of nanoparticle loading, by volume. It is evident that the heat transfer coefficient coupled with radiative enhancement (h_{EMT}+$h^{\uparrow}_{rad,F^{*}_{12}}$) increases by 23% (for emissivity, ϵ = 0.5), 25% (ϵ = 0.6), 28% (ϵ = 0.7) for every 1vol% nanoparticle loading. It is noted that for higher nanoparticle loading of 5%, effective heat transfer coefficient increases from 100% to 140%. It is also observed that heat transfer enhancement derived from experimental thermal conductivity enhancement data matches well with the predicted enhancement for higher emissivity limit ($\epsilon = 0.7$) with impractical wall temperature. It is essential to note that with realistic wall temperature of (20°C-50°C) [87, 88, 89], the radiation contribution to Heat Transfer Coefficient (HTC) enhancement will be zero. The moderate discrepancy between the calculated experimental HTC data and

model prediction is because of the under-prediction of thermal boundary layer thickness caused by truncation error in Eq. 4.4.

In our calculations of the HTCs – via simultaneously solving for the flow-field and temperature-field (Eqns. 4.2-4.11) to extract δ_{th} –a nanoscale axial location (x) and far-field flow velocity (u_∞) based on the Brownian motion of the nanoparticles are assumed. This Brownian motion approximation facilitates the use of specific values for u_∞ and x in our calculations of δ_{th}. Specifically, $x \approx d$ and $u_\infty \approx d\omega_b/4\pi$ are used, where the Brownian rotation/spin frequency for a spherical nanoparticle of diameter (d) is $\omega_b = \frac{2\mathrm{K}_B T}{\pi \mu_o d^3}$ [141] and K_B is the Boltzmann constant. While the approximated flow-field velocity turns out to be a notable *m/s* value, the potential advective enhancement due to Brownian motion is counteracted by the nanometer length-scale of the nanoparticles. In support, the corresponding Reynolds number for Brownian motion scales as: $\mathrm{Re}_B \approx \mathrm{K}_B T/\rho_o \nu_o^2 d$ and is $<< 1$ (i.e., in the limiting Stokes flow regime). Thus, as expected, Brownian motion of the nanoparticles does not enhance the heat transfer coefficient or effective thermal conductivity within the thermal boundary layer. And, as our results in Fig.4.6 support, heat transfer coefficient enhancements by the nanoparticles can only be due thermal conduction and inter-particle radiation within the thermal boundary layer. In this study, the emissivity values plotted in Fig. 4.5 and Fig. 4.6 are for limits beyond that observed by others [142, 143].

Summary

This chapter demonstrates the fundamental approach of analytical calculation to capture overall heat transfer enhancement due to coupled conduction, convection, and radiation in aqueous Al_2O_3 nanofluids. The optically thin thermal boundary layer approximation has been employed to account for the changes in the thermal boundary layer thickness at different nanoparticle loadings. Effective medium theory, incorporating the thermal resistance at the solid particle-liquid inter-

face, shows 1% increase in thermal conductivity for every 1% increase in nanoparticle loading up to 5% by volume. However, including contributions by radiation, the effective thermal conductivity of nanofluid is shown to increase by 5% for every 1% increase in volume fraction at higher limit of emissivity ($\epsilon = 0.7$) with an unrealistic wall-temperature of 600K. However, if the wall-temperature is set to practical values of 20°C-50°C in regards to actual implementations [87, 88, 89], such radiation contribution will be close to zero. For example, if the temperature is set to realistic value of 50°C (323K), the thermal conductivity will be enhanced by 0.31% (for emissivity, ϵ = 0.5), 0.55% (ϵ = 0.6), 0.78% (ϵ = 0.7) for every 1% (by volume) nanoparticle loading into the system. After a survey of the experimental data from many recent thermal transport studies, it is found that the averaged thermal transport data from such experiments turn out to match relatively well with our conjugated conduction-convection-radiation calculations. For example, along with correlation between experiments and our calculations for the effective thermal conductivity enhancements, the heat transfer coefficient is also shown to increase by 25% for every 1% particle loading (by volume) but such contributions will be zero for a practical wall temperature of 20°C-50°C [87, 88, 89]. Since our calculations are not suited to quantify contributions from near-field radiation when the inter-particle separations are comparable to the plasmon length or skin depth at infrared frequencies, the possibility of additional enhancements cannot be excluded at higher nanofluid loadings $\phi >> 0.1$ (10 vol %) with stable and non-flocculating nanoparticles that are well-dispersed in an optically transparent solvent. Now that actively pulsated cooling is understood using experiments and modeling, it is imperative to also look at how this pulsation cooling technique can be implemented in passive setting. To do this, the design, fabrication, and testing of 3D-stacked flexible pulsating heat pipes, suitable for futuristic heterogeneous packages and cascaded systems, are proposed in Chapter 5.

CHAPTER 5: DESIGN, FABRICATION, AND TESTING OF VERTICAL STACKED SYSTEM WITH FLEXIBLE PULSATING HEAT PIPES

Literature Review

High-speed telecommunication, Artificial Intelligence (AI), transportation, CPU/GPU, and cloud-computing are all examples of complex high-performing systems that generate heat while in operation [144, 145, 146]. With innovative technologies, the demand for both active and passive cooling has increased significantly because of this. Though the strengths of active cooling are many, various applications exist where they are not the best option. A passive alternative solution known as Pulsating Heat Pipes (PHPs) [147] offer high heat transfer performance without the need of external power consumption and are suitable for both ground and space cooling applications [148, 149, 150, 151, 152, 153].

PHPs are defined by closed or open loop channels patterned in a serpentine shape. Like traditional heat pipes, the coolant inside the PHP channels transfers thermal energy from the hotspot location via liquid-vapor phase change of the fluid, called liquid slug and vapor plug pulsations. A pressure difference is generated because of the temperature difference between the heat source and the heat sink. Such conditions enable the thermodynamic transport of energy from one side to the other in the form of latent heat transport- dissipating the heat [154].

There have been numerous experimental and theoretical studies of PHP's heat transfer capabilities with its simplistic nature[155]. Recent advancements in this field include improvements in channel path design optimization [156, 157], material flexibility [158, 159] and greater overall dependability[159]. Lim et al. [160] demonstrated an innovative design to outsource heat from local hotspots. Using topology optimization, they demonstrated an overlapped channel orienta-

tion which increases the thermal performance by a factor of two. Although PHPs have a simple wickless design compared to conventional heat pipes, there are still many technical challenges [161, 162, 163]. Two major obstacles facing the implementation of PHPs include the difficulty of creating them with resource-consuming processes and their physical limitations in tackling the demand for embedded 3D electronic cooling packages. Therefore, a heterogeneous package cooling solution for 3D architecture is of great interest. Although double-side cooling has shown promise recently [164], there is very little experimental evidence about the design, fabrication, and testing of two-stack passive cooling technology with a single heat source.

This work demonstrates the fabrication process for creating modular, flexible pulsating heat pipes. Using high-speed videography and micro thermocouple temperature measurements, the performance of two-stack systems are evaluated. Essentially, research efforts are pursued to come up with i) a fabrication process that is easy, cheap, and repeatable and ii) an innovative design with modular features that makes it suitable for double-sided cooling configuration. Secondly, experimental testing is pursued to reveal the flow and thermal kinetics for different condensation conditions. This work identified many designs, fabrication, and thermal performance limitations tied to planar and stacked-3D pulsating heat pipes that can incorporate multi-phase coolants such as water and paraffin wax.

Fundamentals of PHP operation

Pressure difference

The channels inside the PHP are filled with liquid. When the liquid comes in contact with the evaporator/heater and reaches the saturation point, it starts to boil and convert into vapor bubbles. As the temperature rises, the vapor bubble increases in size, trying to push the adjacent liquid

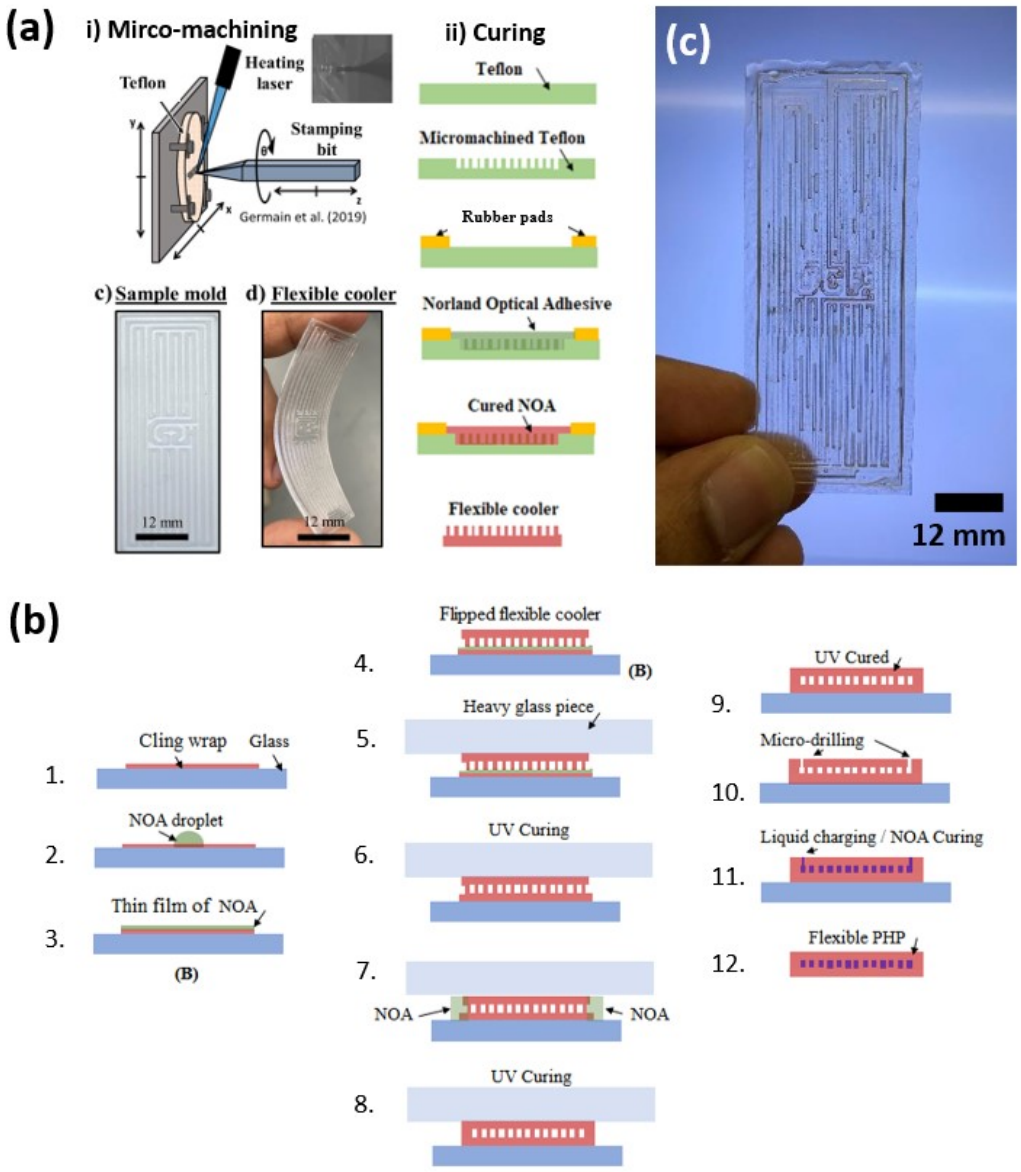

Figure 5.1: Fabrication of flexible pulsating heat pipe. a) Preparation of the mold: Microstamping apparatus is used to create channel walls in bare Teflon slab and Norland Optical Adhesive (NOA) is later poured into the mold and cured to achieve flexible PHP, b) Cling wrap is used with NOA film to cap the open side of the PHP to fabricate self-contained single PHPS, c) Coolant, in our case, water is poured into the pulsating heat pipe using the micro-drilled inlet ports.

slug. Due to this, the evaporator pressure becomes higher. When these vapor bubbles reach the condensers/heat-sink, they reject the heat and become liquid slugs. During this period, the vapor bubbles shrink, and the pressure gets relieved. For this reason, the condenser pressure is lower. This pressure difference between the evaporator and condenser is the driving force of the pulsation motion of liquid slugs inside the PHPs. The evaporator pressure is [165]

$$P_e = P_o e^{(h_{fg}/\mathrm{R})\times((T_e - T_o)/T_e T_o)} \tag{5.1}$$

where, h_{fg} = 2257 kJ/K is the enthalpy of vaporization, R = 8.316 $m^2 kgs^{-2} K^{-1} mol^{-1}$ is molar gas constant, T_e is the evaporator temperature, T_c is the condenser temperature.

The condenser pressure can written as below.

$$P_c = \sum_{i}^{n_v} P_v^i \tag{5.2}$$

where, $P_v = f(\phi, T_v)$ is the vapor plug pressure, ϕ is the filling fraction and T_v is vapor temperature.

Heat transfer

The overall thermal performance of PHP is governed by the heat transfer at the evaporator and the condenser. Each PHP contains one evaporator, two condensers, and four adiabatic sections for this particular setup. In the evaporator zone, three heat transfer modes contribute to the overall heat transfer. They are conduction from solid to liquid, liquid to vapor, and convection from solid to liquid. The convection heat transfer mode can be divided into two parts, i) microscale heat transfer at the thin film meniscus zone and ii) bulk heat transfer during bulk liquid slug motion. The heat

transfer rate in the evaporator zone can be expressed as [154]-

$$Q_e = \sum_{i=1}^{N} 2\pi r K_l (T_e - T_{vi}) \int_0^L \frac{1}{\delta}.dx + \sum_{i=1}^{N} 2\pi r K_l (T_e - T_{vi}) \int_0^{R-\delta} \frac{1}{\delta_m}.dx + \int_0^L \pi D_{crit} h (T_{L_i} - T_w).dx \tag{5.3}$$

And, the condenser heat transfer rate can be expressed as below [154].

$$Q_c = \sum_{i=1}^{N} 2\pi r K_l (T_{vi} - T_c) \int_0^L \frac{1}{\delta}.dx + \sum_{i=1}^{N} 2\pi r K_l (T_{vi} - T_c) \int_0^{R-\delta} \frac{1}{\delta_m}.dx + \int_0^L \pi D_{crit} h (T_w - T_{v_i}).dx \tag{5.4}$$

where, N is the number of vapor bubble, r is the channel radius, δ is the liquid film thickness, $h = h_{mic}$+h_{bulk} is the heat transfer coefficient, T_w is the wall temperature.

Pulsation motion

Vapor bubbles form when the heat is added to the system (evaporator). If the channel diameter is sufficiently small, these vapor bubbles will turn into vapor plugs and start to circulate. Since the PHP used in this study is a closed-loop PHP, this circulating motion of vapor plugs results in oscillatory or pulsating motion. The pulsation motion of the liquid slugs inside the channels can be predicted by the gas-spring model [166] where the vapor plugs are the springs, and liquid slugs are the mass of the vibration system. Therefore, the following equation for forced damped mechanical vibration can be written as-

$$\frac{d^2x}{dt^2} + \frac{c}{m}\frac{dx}{dt} + \frac{K^s}{m}x = \frac{B}{m}(1 + \cos\omega t) \tag{5.5}$$

where, the mass of the liquid slug (m) can be found by-

$$m = A(\rho_l L_l + \rho_v L_v) \tag{5.6}$$

where, ρ_l is the density of the liquid, ρ_v is the density of the vapor and A is the cross-sectional area of the channel. The damping coefficient (c) can be calculated from the following expression.

$$c = A[(f_l.\mathrm{Re_l})(\mu_l L_l/2D_{crit}^2) + (f_v.\mathrm{Re_v})(\mu_v L_v/D_{crit}^2) \tag{5.7}$$

where, f_l is the friction coefficient due to liquid-slug motion, f_v is the friction coefficient due to vapor-plug motion, Re_l is the Reynolds number corresponding to liquid-slug, Re_v is the Reynolds number corresponding to vapor-plug, μ_l is the dynamic viscosity of the liquid, μ_v is dynamic viscosity of the vapor, L_l is the liquid slug length, L_v is the vapor plug length inside the channel. The gas-spring constant can be found from-

$$K^s = \frac{A\rho_v \mathrm{R} T_v}{L_v} \tag{5.8}$$

The magnitude of the driving force, B can be expressed as-

$$B = \frac{Ah_{fg}\rho_v}{T_e}\frac{\Delta T_{max} - \Delta T_{min}}{2} \tag{5.9}$$

where, h_{fg} is the latent heat of vaporization, T_e is the evaporator temperature, T_c is the condenser temperature, ΔT_{max} is the maximum temperature between the evaporator and condenser, ΔT_{min} is the minimum temperature difference between condenser and evaporator. The undamped natural frequency (ω_o) and the damping ratio (ζ) can be found by-

$$\omega_o = \sqrt{K^s/m} \tag{5.10}$$

and,

$$\zeta = \frac{c}{2m\omega_o} \tag{5.11}$$

These set of equations can be solved with initial condition (x = 0, t = 0, dx/dt = 0) and set of boundary conditions. Finally, the exact solution can be obtained via Laplace transformation.

Thermal performance of PHP

The thermal performance of PHP can be determined by estimating heat flux, overall heat transfer coefficient, effective thermal conductivity, and thermal resistance. For 3D-stack configuration (dual layer), the heat flux can be estimated by the following modified equation [167].

$$q" = \frac{nK_l\Delta T}{r_{in}\ln[r_{in}/(r_{in}-\delta)]} \tag{5.12}$$

where, the thermal conductivity of water, K_l = 0.68 W/mK and radius of the channel, $r_{in} = D^m_{crit}/2$, and the number of PHPs in the stack, n = 2. At a power load of 3W, the modified theoretical model shows a superheat (ΔT) value of 0.51K for an assumed liquid film thickness (δ) of 50μm.

The overall heat transfer coefficient can be expressed as-

$$HTC_{avg} = \frac{Q}{A_{evap}(T_w - T_L)} \tag{5.13}$$

where, Q is the input power and A_{evap} is the surface area of the evaporator zone. The thermal resistance can be determined by-

$$R_{th} = \frac{T^{max}_w - T_\infty}{Q} \tag{5.14}$$

The effective thermal conductivity can be expressed as-

$$K_{eff} = \frac{L_{tot}}{A} \frac{Q}{T_w - T_L} \tag{5.15}$$

where, L_{tot} is the total length of the PHP.

Design and Fabrication

Channel diameter

The pulsating heat pipe works based on capillary, frictional, and gravitational forces. When the capillary force inside the channels overcomes the buoyancy force, the coolant encounters a net force due to surface tension that drives the liquid slug. The Bond number is calculated to establish the relative importance of capillary force over gravitational force.

$$Bo = \frac{g(\rho_l - \rho_v)D^2}{\sigma}, \tag{5.16}$$

where, g = 9.81ms^{-2} is the gravitational acceleration, ρ_l = 998 kgm^{-3} is the density of the water, ρ_v = 0.008 kgm^{-3} is the density of the vapor, σ = 72 $\times$ 10^{-3} Nm^{-1} is the surface tension of water, and D is the diameter of the PHP channel. Different studies show that the Bo = 4 [168, 169]. The corresponding criterion of the critical diameter is then

$$D_{crit} = 2\sqrt{\frac{\sigma}{g(\rho_l - \rho_v)}}. \tag{5.17}$$

Eq. **??** is applicable for interfaces of high surface energy. However, the PHP material, Norland Optical Adhesive (NOA), used in this study has low surface energy; therefore, the water droplet's

contact angle becomes an important parameter. Using Young-Laplace relation, the Eq. **??** is reformulated as: [170]-

$$D^m_{crit} = 2\sqrt{\frac{\sigma \cos\theta}{g(\rho_l - \rho_v)}}. \tag{5.18}$$

The contact angle, θ in Eq. **??** is measured experimentally to be 61° as shown in supplementary figure. Using the thermophysical properties of water [170], the critical diameter, D_{crit} is calculated to be 3.9 mm. The hydraulic diameter of the channel (D_H) needs to be smaller than D_{crit} for sustained oscillatory vapor plugs and slug-train formations [159]. For this reason, PHPs with a combination of high channel turn density and sufficiently small channel diameters (D_{crit}= 0.7mm $\pm$ 0.14mm) are fabricated.

Number of turns

The number of channel U-turns is the key PHP design parameter. A high number of channel U-turns are needed to 1) achieve high wall heat flux, 2) ensure the stability of pulsation, and 3) promote two-phase events (onset of nucleate boiling). Kammuang-Lue et al. [171] provided a predictive criterion to quantify the heat flux as a function of the number of channel U-turns.

$$q" = 6.25 h_{fg} \rho_v (g\sigma \frac{\rho_l - \rho_v}{\rho_v^2})^{-0.25} v_{CG}^{0.34} (\frac{D^m_{crit}}{L_e})^{0.91} N^{0.26} \tag{5.19}$$

where, h_{fg} = 2257 kJ/K is the enthalpy of vaporization, v_{CG} = 2.3 $\times$ 10^{-3} m/s is the Critical Gas Velocity, L_e = 2.54$\times$ 10^{-2}m is the length of evaporator, and N is the number of U-turns. Using Eq. **??**, 28 U-turns are needed to have a rectangular PHP to extract 1000 KW of heat from a 1m^2 heater area until it reaches the dryout. However, during experiments, it is expected reach heat fluxes of 12.7 KW per square meter.

Mold preparation and PHP fabrication

A patterned mold for the PHP is fabricated using a computer-controlled micro-milling apparatus [1]. Later, the mold is cleaned by air blow, followed by a gentle rinse in ethanol. The consistency of the channel dimension is inspected by an optical microscope. Then the Teflon mold is put on a smooth aluminum base. Then NOA is poured into the mold, and the air bubbles are removed. A clean glass window/plastic wrap is put on the NOA film. The plastic wrap not only offers easy removal of glass windows after curing but also provides lamination to the PHP base. The open side of the channel wall is attached to an NOA thin film to get a self-contained PHP, as illustrated in Fig. 5.1c.

Experimental set up

Embedded Heater

A metallic foil heater (serpentine in shape) is used to mimic heat generation in processor-scale micro-electronics. The surface area of the serpentine heater is measured to be $2.34 \times 10^{-4}\text{m}^2$. The copper busbar is then connected to the extended portion of the heater. The serpentine heater is then submerged into NOA liquid film and cured under UV light. AC power supply is used to supply current at 333 Hz to the copper busbars, which results in Joule-heating.

Two-stack PHP and charging

Two PHPs are placed on both sides of the embedded heater film and are glued with NOA. It is ensured that the inlet/outlet ports of the PHP are aligned. The coolant (DI water) is charged using a syringe needle until all the channels are partially filled. After filling the channels with desired

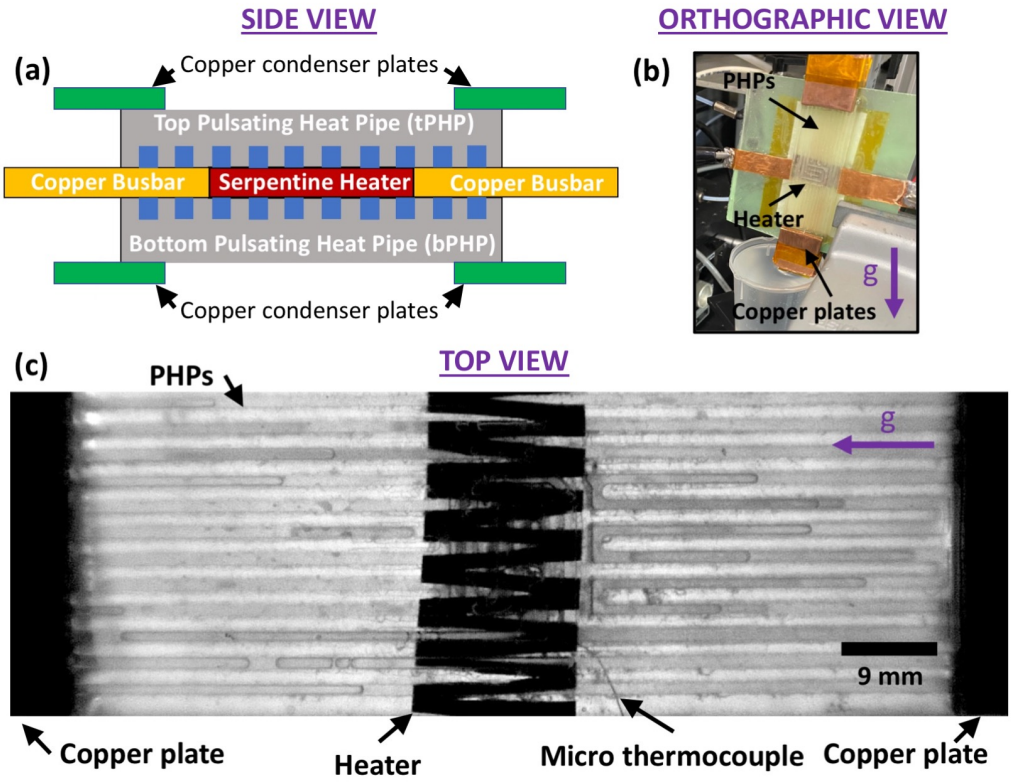

Figure 5.2: Vertically stacked pulsating heat pipe configuration (single-heater): a)Two pulsating heat pipes (PHPs) with embedded heater where PHP channels, filled with water, are facing towards the heater, b) The copper condenser plate is submerged in ambient water to create a distinctive temperature difference between the heat source and the heat sink, c) High-Speed Camera (HSC) view of the testbed with LED backlight for better visualization of liquid slug pulsations inside PHP channels.

volume fraction (60%), inlet and outlet ports are capped.

High speed visualization

A high-speed Phantom camera is used to test the flow performance of the 3D-PHP-stack and record at 1000 frames per second. The stack is mounted vertically on the optical breadboard at a distance of 635mm from the camera. A rectangular piece of white paper of size 77mm $\times$ 26mm is attached

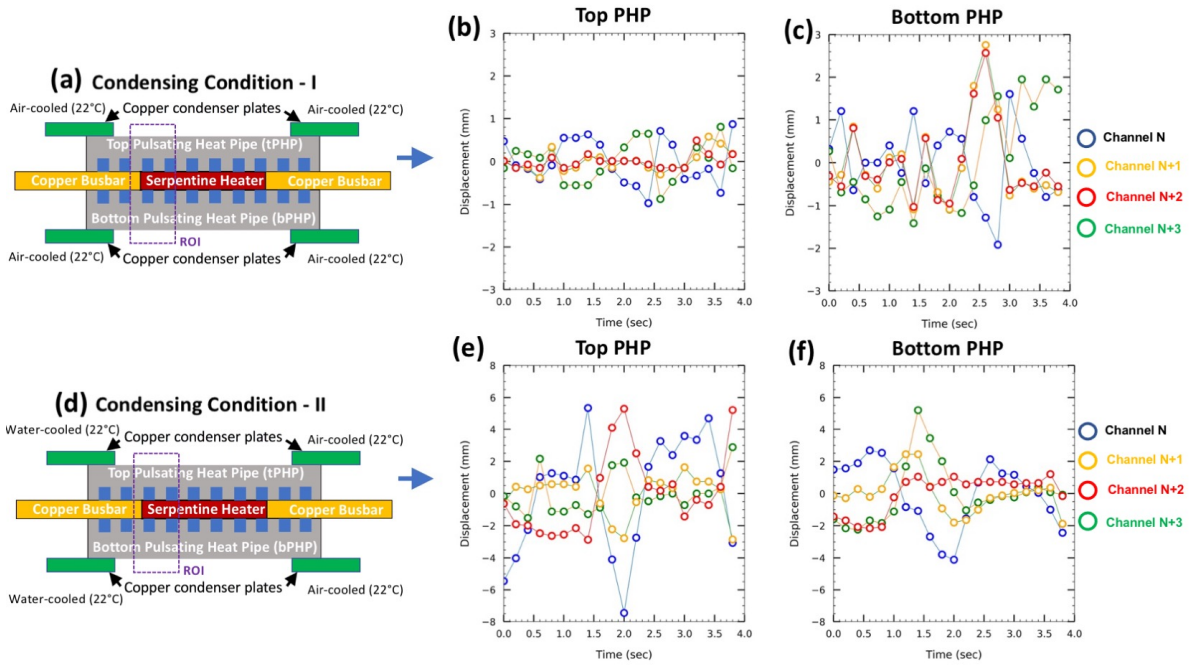

Figure 5.3: Effect of condensing condition on the pulsation motion of liquid slugs inside the channels in the two stacked PHP assembly. Two condensing conditions are tested – i) Both ends are exposed to ambient air (Fig. a), ii) one end is exposed to ambient temperature, and another end is exposed to ambient water (Fig. d). Fig. (c-d) and Fig. (e-f) show the pulsation magnitudes for top, and bottom PHPs at the ROIs outlined in Fig. a and Fig. d, respectively.

on the back side of the back PHP using Kapton tape. Thus, the LED backlight gets absorbed by the paper and diffused over the larger surface, which helps capture important fluid pulsation events in both the PHPs in the 3D-stack.

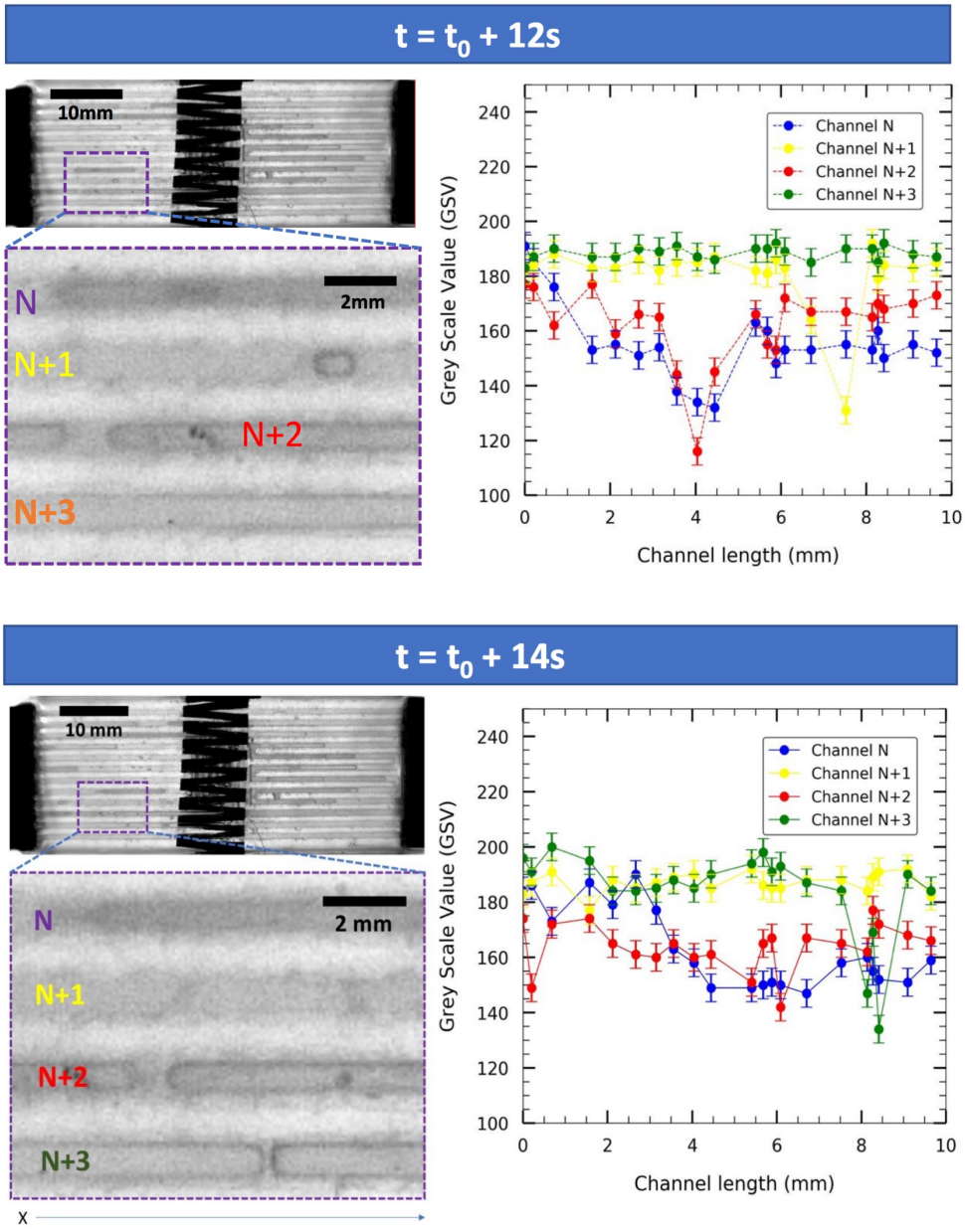

Figure 5.4: Identifying the interface at two different time-stamps ($t = t_0 + 12s$ and $t = t_0 + 14s$): Interface between liquid-slug and vapor-plug are needed to be identified in both the PHPs of the two-stack system. Grey Scale Values, exported from the Phantom program, are used to track these interfaces. Rectangular ROI contains four channels (N, N+1, N+2, N+3), b) Grey Scale Values (GSVs) are plotted as a function X (from 0mm to 10mm) where any drop in the GSV signify the liquid-vapor interface.

Testing Results

Flow kinetics

The liquid inside the PHPs oscillates due to a pressure gradient caused by temperature difference. As illustrated in Fig. 5.3, two conditions are selected to investigate how condensing conditions influence the pulsation motion in both PHPs. Condensing condition-I has air-cooled condensers (22°C) on both ends of the 3D-stack. The condensing condition-II has one condenser air-cooled (22°C) and another one water-cooled (22°C). The pulsation motions are captured at four liquid-vapor interfaces at P = 3W and ΔT = 98 °C . The pulsation magnitude is 1mm (front PHP), whereas this magnitude is three times higher for bottom PHP. For the water-cooled condenser, it is observed that the magnitude of pulsation increased significantly compared to that of the air-cooled condenser. In this case, the front PHP shows a higher pulsation magnitude (8mm) than the back PHP. Based on these flow testing outcomes, it can be said that for both sides to work simultaneously with comparable and consistent pulsation, at least one condenser needs to be water-cooled.

The interfaces between liquid slugs and vapor plugs in different channels are identified using the image grey-scale-analysis. At $t = t_0$ + 12s, it is seen that the channel N+2 and N+1 (ROI in Fig. 5.4) show a large drop of GSV at x = 8mm and 4mm, respectively. At $t = t_0$ + 14s, similar drop of GSV is visible for N+2 and N+3 channels but at different locations, e.g. x = 6mm and 8mm, respectively. These GSV drop determine the location of the liquid-slug interface.

Thermal Characterization

The liquid slug inside the channels near the heat source (evaporator) transports the heat to the heat sink (condenser) using both single and two-phase heat transfer processes. Single-phase heat

transfer mainly involves thermal transport from the PHP walls to the liquid slug. The two-phase heat transfer process consists of evaporating liquid slugs near the heat source and condensing vapor plugs near the copper condensing plates. The start-up condition is called the power at which the two-phase events occur more spontaneously and start to dominate the single-phase component. Different factors that determine and influence this start-up condition are power load, heat flux, condensation condition, working fluid properties, and initial temperature of the working fluid, as

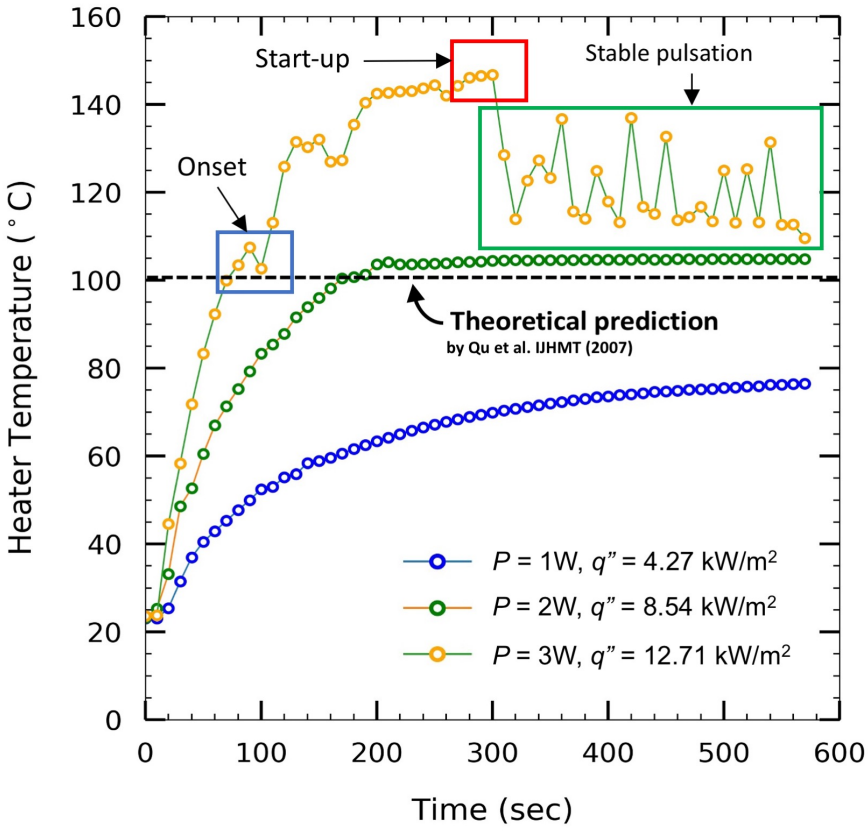

Figure 5.5: Quantifying the thermal start-up condition. Heater temperature fluctuates due to nucleate boiling near the center of the heater at high power loads of 3W, and a drop of 30 °C is visible due to latent heat exchange. Theoretical prediction by Qu et al. (Eq. 5.12) shows that at least 0.51K superheat needed for optimum start-up of the PHPs. The data for all the power loads contain a 1% uncertainty.

discussed by Qu et al. [167]. At 1W, the temperature stably increases with time. The single-phase heat transfer occurs where the heater temperature is stabilized at 80°C. With an increased power load of 2W, the heater reaches the steady-state temperature of 100°C. When the power load is increased from 2W to 3W, small fluctuations in temperature are observed because of the onset of two-phase events (bubble formation).

It is seen from Fig. 5.5a that, from 100s to 300s, the heater temperature increases with minor

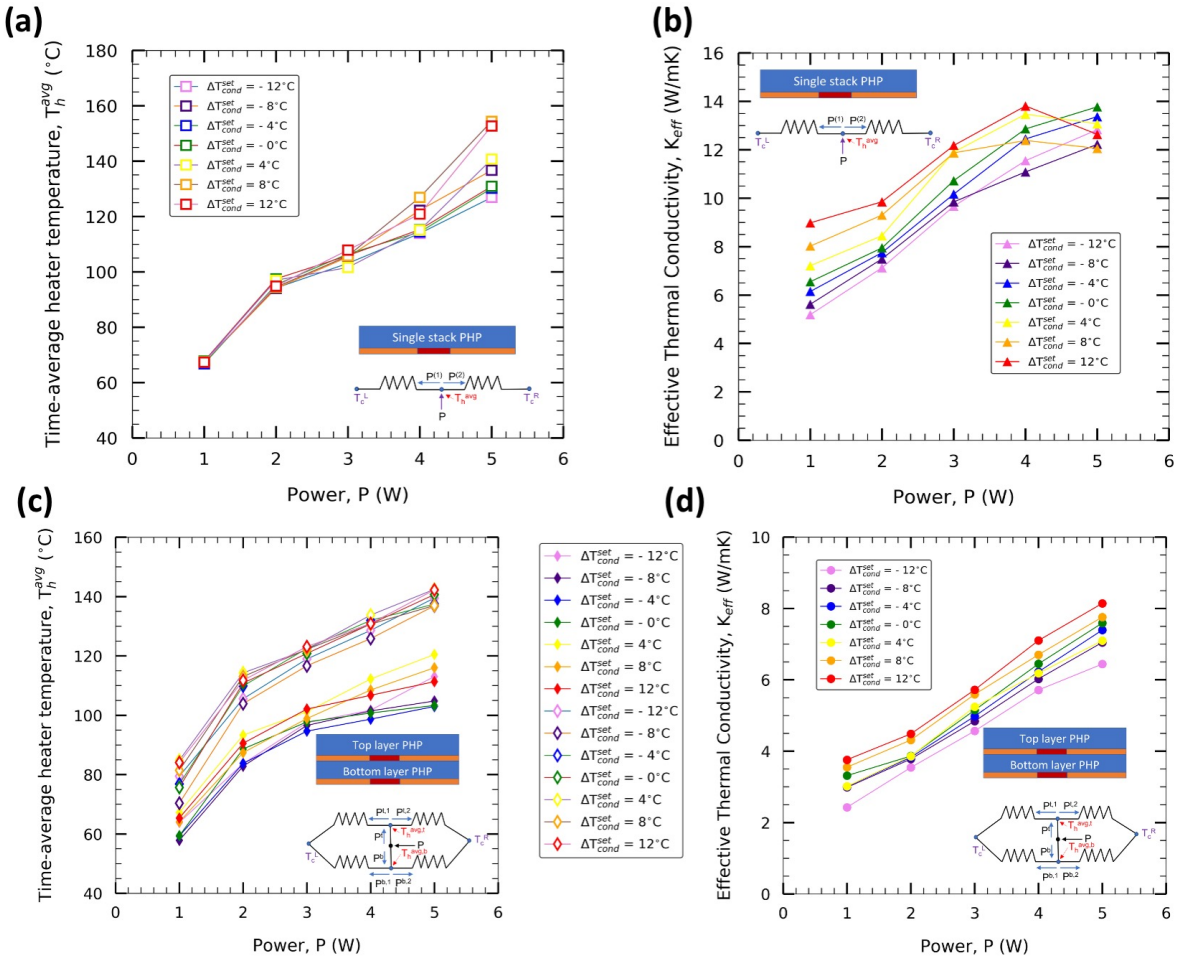

Figure 5.6: Time-average temperature and effective thermal conductivity estimation for planar and 3D-stack-PHP (dual-layer) as a function of condenser temperatures (both top and bottom) and power loads.

fluctuations. In this period, vapor pressure inside the bubbles increases with temperature, which helps the bubble to grow into Taylor bubbles. These Taylor bubbles fill the channels and turn into vapor plugs. This increased pressure in vapor plugs creates a pressure difference between a liquid slug and a vapor plug. When this pressure difference overcomes pressure drop due to friction, the liquid slugs move back and forth. Eventually, the vapor plugs oscillate and condense back to liquid at the copper condensers, which results in a fluctuation of heater temperature within 115°C to 130°C in a stable manner.

Later, two flexible Pulsating Heat Pipes (PHPs), lidded with NOA/heater film, are vertically stacked and aligned in such a way that there are two thermal vias (I/O ports). Two micro thermocouples on the heaters are also embedded in the NOA film to extract local temperatures. It is of significant importance that the majority of the heat generated by the heaters is carried out by the liquid pulsation inside the PHP channels. It is found from the results discussed that liquid-cooled condensers enhance the condensation process, which results in higher magnitudes of liquid pulsations. For this reason, liquid-cooled condenser plates are designed. Essentially, copper tubes are attached with highly conductive copper slabs via soldering. A Polyflow chiller provides chilled water to all the condensers to keep them at a constant temperature. The I/O ports are capped with thermally conductive copper foils to ensure that the liquid inside the channels is in direct contact with the condensers.

Evaporator temperature is crucial to calculate the effective thermal conductivity of both PHP layers in the 3D-stack. Therefore, it is essential to ensure that the temperature readings are accurate. For this reason, the temporal temperature data is calibrated with IR thermal imaging readings. However, it is essential to note that the PHP material (NOA) is not transparent to the IR camera, making it incompatible for thermocouple (TC) calibrations. For this reason, IR transparent Calcium Fluoride (CaF_2) replaced the NOA film for calibration. Before acquiring thermal image data, the pixel location of the TC lead is identified on the ResearchIR max software. Later, the thermocou-

ple data acquired by the DAQ board (via LabVIEW) is compared with the IR camera readings. Supplementary Fig D.9 shows good agreement between the TC and IR readings.

Integration and challenges

A 3D-PHP-stack, made of plastic, is fabricated and integrated with mu-metal heaters and micro-thermocouples. The edge and surface of layers are prepared with primers, and the adhesive (JB-weld) is applied at the edges. PFA films separate PHPs to hold the liquid (water) inside the channels (Fig. 5.7). Later, through-holes are drilled at the ends of the PHP-stack so that the liquid inside the channels interacts directly with the copper condenser plates cooled by a chiller. The stack is closely monitored for any leakages while the PHP is getting charged with water. After the leakage locations are identified and marked, more adhesive is put on those locations. However, two immediate challenges are encountered - i) the degradation of adhesive strength over temperature and time and ii) adhesive wicking into the channels. For these challenges, a simpler PHP design is attempted, which is planar and lidded with IR transparent CaF_2 window. The IR transparent window's purpose is to acquire accurate thermal images using an IR camera at different power loads (0W-2W).

The channels are filled with paraffin wax, as illustrated in Fig 5.7(d-f). It prevents the adhesive from wicking into the channels during the integration process. After the planar PHP test setup is prepared (Fig 5.7d), paraffin wax is flushed off by heating it, which, however, results in leaking from the busbar edges of the test setup. Another design with a new mu-metal heater system is attempted to resolve this problem. In this design, the heaters are placed at the end of the PHP instead of the center. In this design, the 3D-stack contained three PHPs and four mu-metal heaters. The bottom condenser plate of the testbed is replaced with an acrylic vise to clamp the heater end and to minimize the micro gap caused by thick mu-metal heaters. However, leakage is revealed from further thermofluid testing using HSV. For this reason, a dual-stack acrylic PHP with an

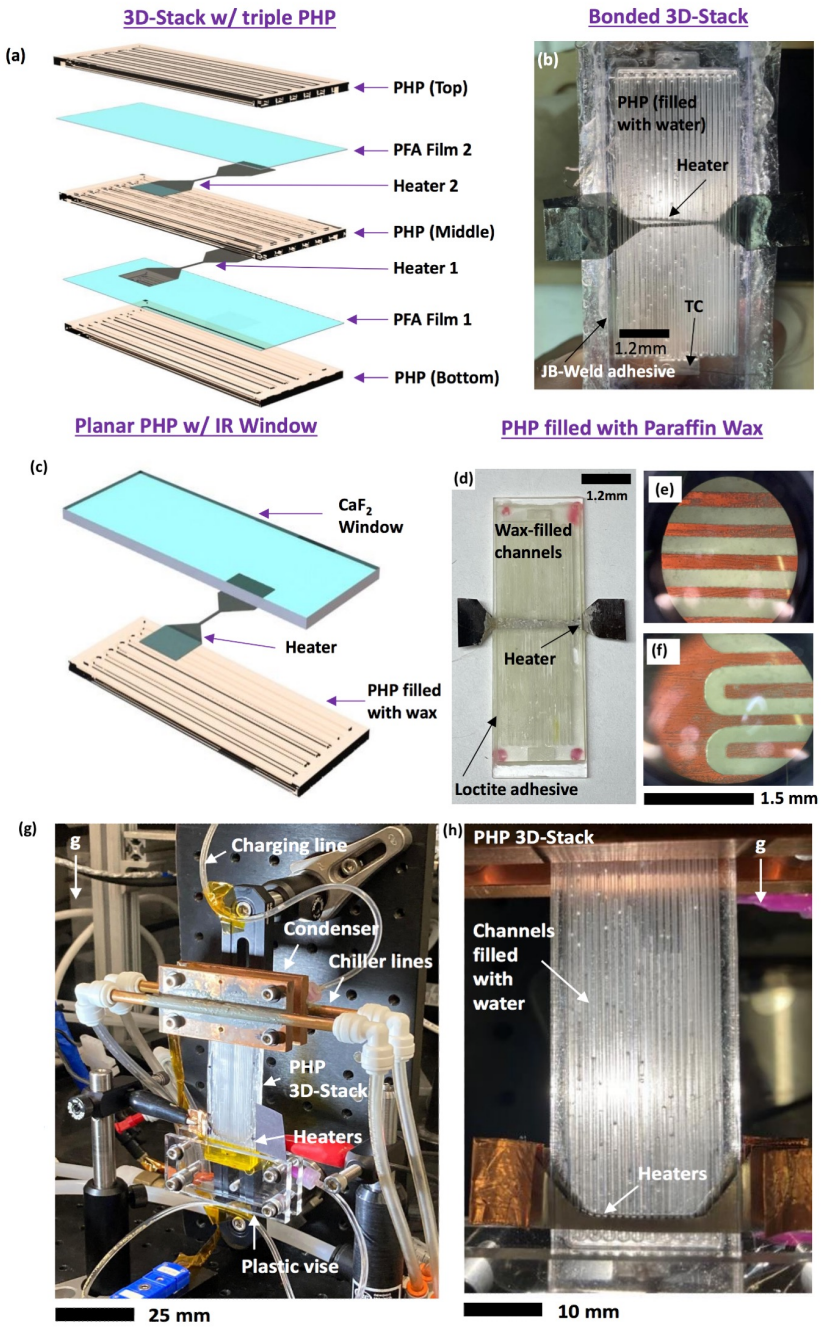

Figure 5.7: Integration and challenges for designing and testing 3D-stack PHPs with different heater designs and locations.

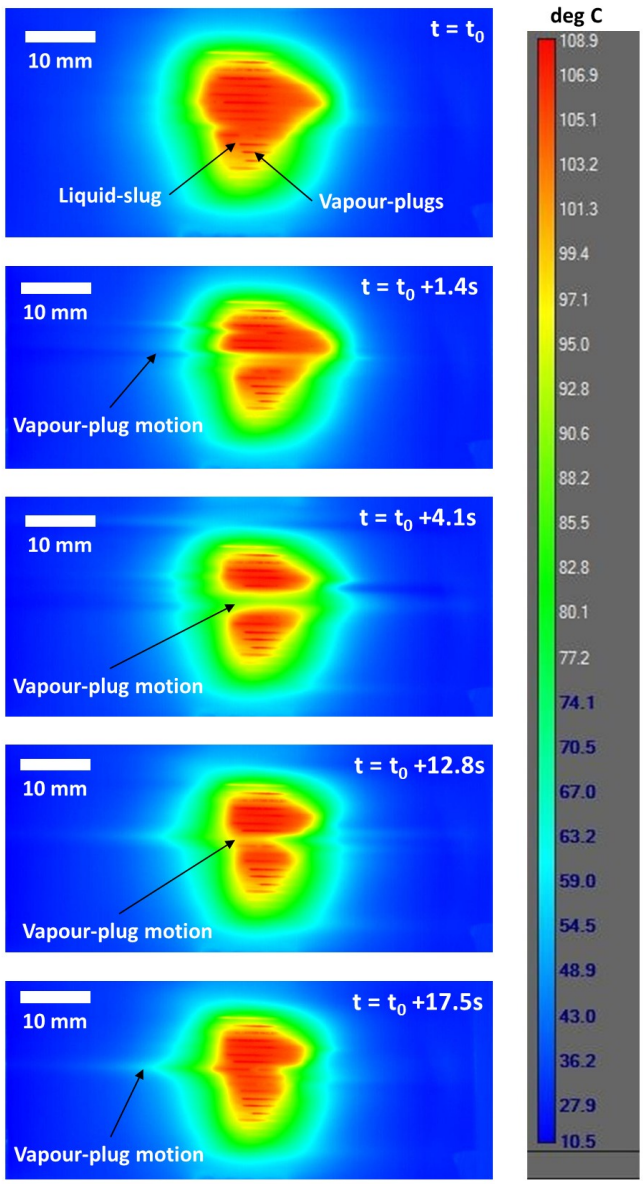

Figure 5.8: Thermal transients revealed by the IR thermal imaging system at condenser temperature of 15 °C and at 2W of power.

embedded heater at the interface is used for IR-thermal testing/validation.

IR thermal transients

The onset of pulsation in the dual-stack system (Fig 5.8) is seen from the IR thermal transients. As the heater's power is increased to 2W, the liquid adjacent to the heater inside the channel boils—the coexistence of liquid slug and vapor plugs inside the PHP is seen in the figure. As the heater temperature is increased, the vapor expands and rushes to the condenser ends, resulting in the relative motion of vapor-plugs and liquid-slugs. The liquid slugs are pushed by these relative motions, coupled with capillary force, into the heater, reducing the temperature. The heater temperature is reduced between t_0 + 4.1s and t_0 + 12.8s due to the stable liquid boiling near the heater. However, the channel's temperature is increased due to a delay in liquid slugs motion from t_0 + 12.8s to t_0 + 17.5s. However, leakages are observed due to the mechanical warpage at the center of PHPs, which immediately reduced the vapor-plug movements.

Summary

Flexible Pulsating Heat Pipes, in recent times, have gained significant attention due to their wide variety of applications. However, the design and fabrication process remains complicated, expensive, and not modular enough for efficient multi-side cooling. Also, the influence of condensation conditions has not been studied experimentally. This chapter addresses these problems and provides solutions on i) innovative design and a more straightforward fabrication process and ii) modular features enabling double-sided cooling and thus providing experimental criteria for start-up conditions in this configuration. An in-house micromachining tool is used to create a Teflon mold. Norland Optical Adhesive is used as the base material of the PHP. For optimum operation, the channel diameter is selected to be 0.7mm with 33 channel-turns in a serpentine shape with dissimilarities in the middle. The availability of the materials and process equipment and the ease of the curing process makes the fabrication steps repeatable with the potential of high volume manufac-

turing. Two self-contained flexible PHPs are stacked on both sides of a single serpentine-shaped heater to address the multi-side cooling problem. To quantify thermal performance, the heater temperature is monitored using a fine-wire-thermocouple. The flow regimes and flow pulsations are identified using a high-speed video camera. It is found that the power needed to start 3D-stack-PHP operation is 3W at superheat of 10K. Modifying the model by Qu et al. [167], it is predicted that at least 0.51K superheat is necessary to reach the start-up condition. A more intricate theoretical model is needed to resolve this discrepancy that considers heat transfer processes in different flow regimes. Moreover, better liquid pulsation is achieved with a water-cooled condenser than with an air-cooled condenser. It is also observed from further thermal performance testing that the effective thermal conductivity of a 3D-stack is smaller than a planar PHP configuration. Moreover, challenges are encountered throughout the integration process because of unreliable adhesive bonding and leakages due to mechanical warpage governed by a thermal gradient at relatively high power load conditions (more than 2W). However, it is still visible from the IR thermal images that active liquid-vapor pulsations exist at a moderate power load (2W).

CHAPTER 6: CONCLUSION

The active and passive liquid cooling based on flow pulsations is addressed in this dissertation from design, fabrication, analytical modeling, and thermal testing perspectives.

Pulsating jet experiments reveal that the maximum heat transfer coefficient increases from 10 kW/m^2K to 14 kW/m^2K when the jet frequency is increased from 7 Hz to 25 Hz. This experimental evidence is validated with a model based on instantaneous heat flux matching. An optimum pulsation frequency of 19 Hz is quantified using Kapitza instability criterion. Moreover, an high-speed thermal mapping technique is developed using Quantum dots. A consistent thermal photoluminescence (PL) coefficient of -0.1 nm/°C is found for 20 successive heating/cooling cycles. Later, a coupled simulation-analytical modeling approach is taken to investigate the combined roles of conduction, convection, and radiation in alumina nanoparticle suspension (up to 5% by volume). A 25% increase in heat transfer coefficient is observed for 1% nanoparticle loading for an impractical wall temperature of 600K. However, such radiation contribution will be close to zero (a maximum of 0.78% increase in thermal conductivity for 1% loading) if wall temperature is realistic in regards to actual applications (20°C-50°C) [87, 88, 89]. Furthermore, it is observed from Pulsating Heat Pipe study that 3W of power is needed for 3D-stack-PHP (dual layer) to start up. It is also found that using a water-cooled condenser ensures a larger liquid pulsation magnitude (8mm) than an air-cooled condenser (4mm). It is also observed that the maximum effective thermal conductivity is 14 W/mK for planar and 8 W/mK for 3D-stack PHP configurations.

For future studies, fabricating planar, flexible, and 3D-PHP with heaters embedded via either lithography or additive manufacturing is recommended to resolve integration challenges. Moreover, shrinking the channels' diameter is recommended to use lower surface tension coolants (ethanol and dielectric fluids) so that the PHPs can be used for safely cooling electronic devices.

APPENDIX A: PULSED LIQUID JET ADDITIONAL INFORMATION

Pulsating Jet: Duty Cycle

A single pulse cycle comprises of an ON and an OFF of the impinging jet (as shown in Fig. A.1). Pulsation frequency is calculated by dividing number of pulse cycles by total cycling time (τ = t_{ON} + t_{OFF}). Such ON/OFF states are created by chopping the free stream jets using low-cost and easy-to-manufacture Aluminum made mechanical chopper wheel. The chopper wheel consists of holes punched at a same radial location but at different distances. The size of these punched holes are chosen in accordance with the required t_{ON} and t_{OFF} for our experiments. The mechanical chopper wheel is coupled to a motor shaft controlled by a DC power supply. The free stream jet needle is aligned in front of the punched holes (shown in Fig. A.1 of manuscript). Changing the angular frequency thus changes the effective t_{ON} and t_{OFF} and therefore the pulsation frequency.

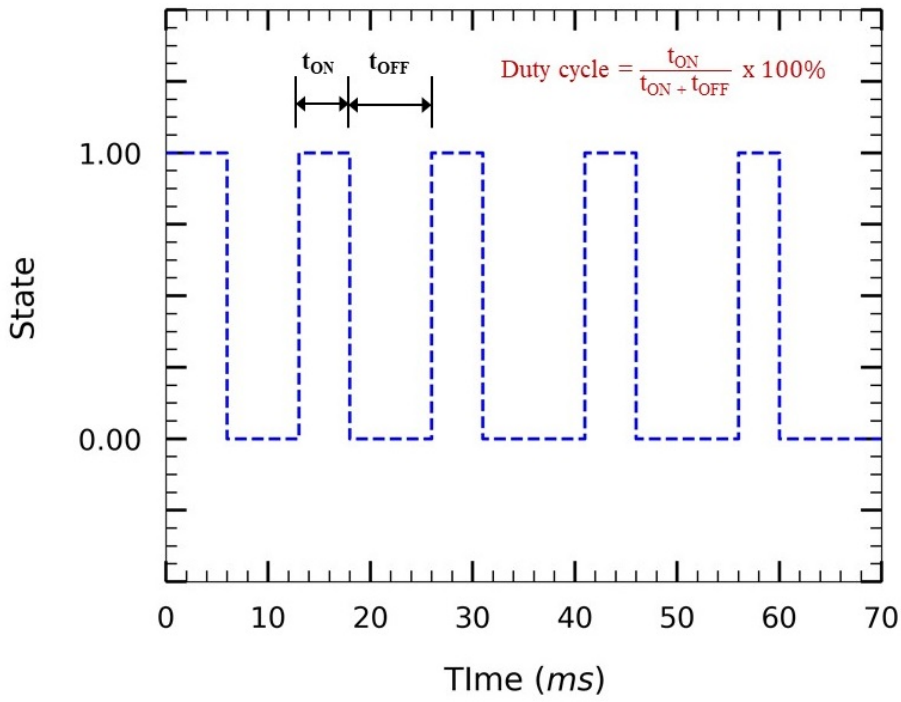

Figure A.1: Sample pulsation profile at frequency of 75 Hz at duty cycle of 25%

The duty cycle is the ratio of t_{ON} to total time period ($\tau = t_{ON} + t_{OFF}$). For example, as shown in figure, 25% duty cycle suggests that the liquid (water) is in contact with the heated surface 25% of the total pulsed time (t_{ON}+t_{OFF}) whereas 100% duty cycle means unpulsed/free stream jets. The duty cycle can be discretely controlled by changing the size and distances between two punched holes in the Aluminum-made mechanical chopper wheel.

Characterization and Calibration

The black paint (coated on Titanium thin film) used for calibration purposes is assumed to be black body. The emissivity is adjusted in the FLIR commercial program to measure the accurate surface temperature. The thin-film of Ti-heater is 99.9% opaque to the IR camera in the MWIR region. According to Mash and Motulevich experiments [3], the refractive-index information calculator shows that, the transmission varies from 0.04% to 0.10% within the ability of our thermal camera's sensitivity (see Fig. A.1c) The calibration of the IR camera is performed by changing the emissivity value of the radiative surface. To test whether the camera is in good working condition, I tried to quantify the emissivity of a known surface (e.g. black paint) by measuring local temperature using IR camera and K-type thermocouple, simultaneously. Therefore, a thin layer of black paint is sprayed on the Ti film. 'Front' refers to optical path from the black paint coating on the sputtered Ti thin-film (i.e. paint/air interface). As indicated by Thermoworks, the emissivity of the black painted Ti surface is atleast 90%. The K-type thermocouple is placed on the black paint side and measured surface temperature (local) by the IR camera on the same side. The temperature values, close to same pixel where thermocouple tip is in direct contact, is captured using the FLIR ResearchIR Max program. The global emissivity value is set to 1 by default and temperature values found from the IR camera did not match with thermocouple reading. The emissivity value is adjusted in the program to match the IR temperature values with thermocouple reading. It

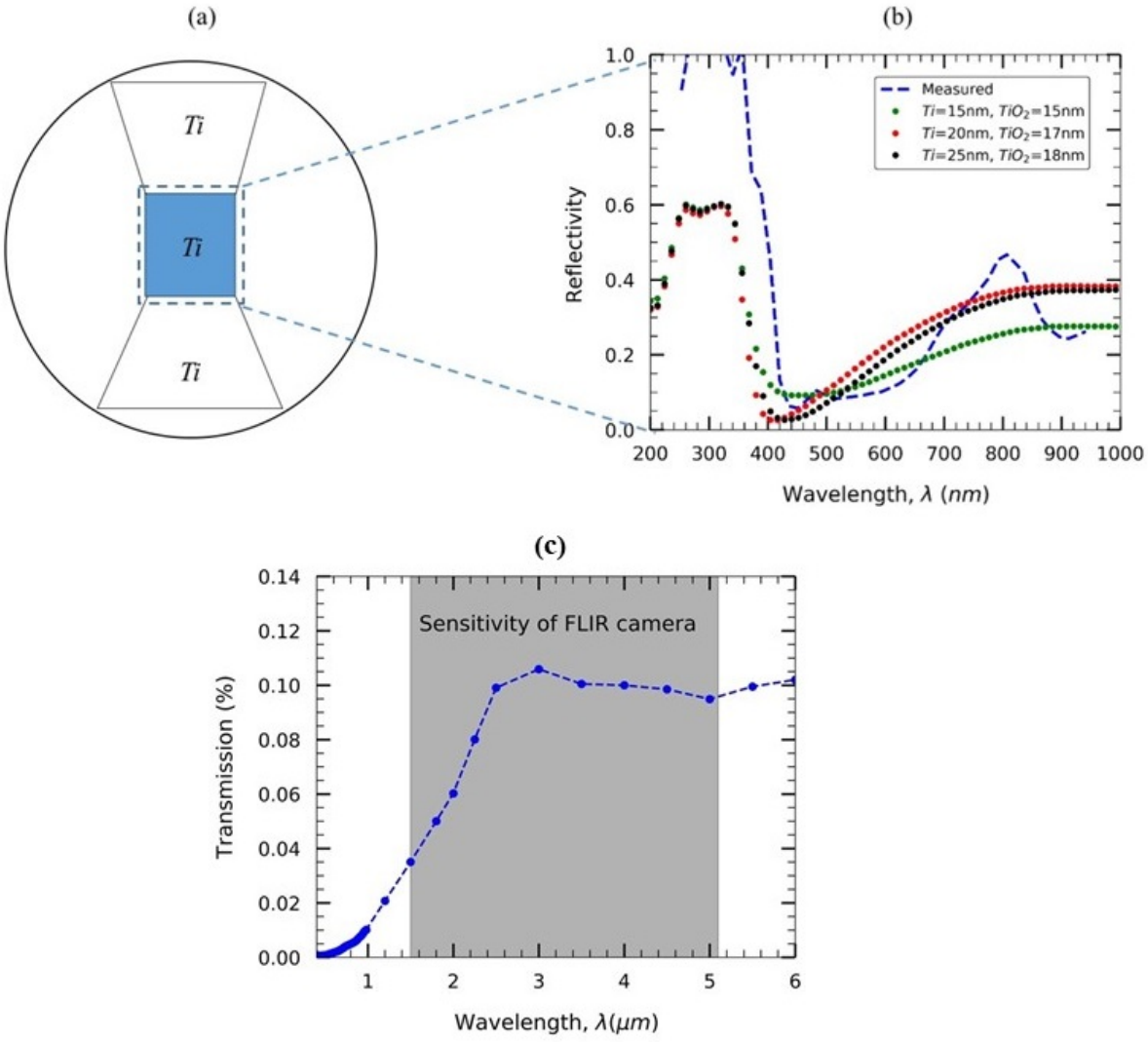

Figure A.2: a) Titanium heater (square) schematic, b) thin film thickness measurement using reflectometry, c) Transmissivity of Ti thin film [3]

is found that the emissivity of 0.9 provides a very good match which certainly means that the thermal camera is in good working condition. However, emissivity value of the Ti/glass interface is still unknown. Now, IR camera is focused on the Ti/glass interface. Hence, the 'Back' refers to the optical path though the glass substrate (Ti/glass interface). The same procedure is followed and adjusted the global emissivity value again (in ResearchIR Max software) to match with the

thermocouple reading. A pixel-by-pixel calibration could not be performed since the program did not allow us to adjust local emissivity values. That's why the area-average temperature values (from IR camera) does not exactly match with the thermocouple readings and points are not aligned in panel 3a and panel 3b to slope 1. Moreover, it is made sure that our thermal camera had the capability to record temperature with uncertainty of 0.3 K. The fluid temperature (T_f) is measured using a K-type thermocouple dipped into the reservoir.

To understand the actual heat flux going into the liquid from the solid-substrate, all the heat

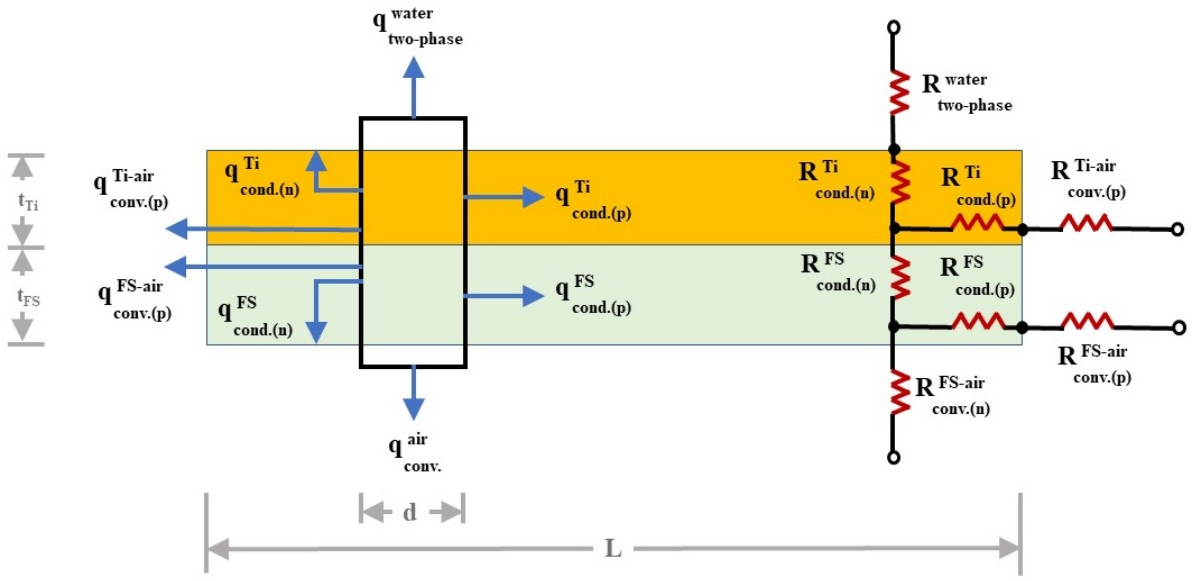

Figure A.3: Heat flow paths in two-dimensional domain and thermal resistance network

losses are needed to accounted for. Calculating the layer-by-layer thermal resistances, this an be understood. This thermal energy generated by Titanium film takes the least resistance path to progress. In our heater/sensor, there are seven ways, the heat can dissipate. They are- i) two-phase/convection from Ti to water ($q^{water}_{two-phase}$) ii) in-plane conduction in Ti ($q^{Ti}_{cond.(p)}$), iii) normal-to-plane conduction in Ti ($q^{Ti}_{cond.(n)}$), iv) in-plane conduction in FS ($q^{FS}_{cond.(p)}$), v) normal-to-plane conduction in FS ($q^{FS}_{cond.(n)}$), vi) convection from FS to air ($q^{air}_{conv} + q^{FS-air}_{conv.(p)}$), and vii) convection

from Ti to air ($q^{Ti-air}_{conv.(p)}$)

Two-phase convective resistance can be estimated as $R^{water}_{two-phase} = 1/(h_{tp}A_{Ti})$. Here, the two-phase heat transfer coefficient, h_{tp} has single phase (h_{sp}) and nucleate boiling components (h_{nb}). Single phase component is essentially a function of Reynolds number and Prandtl number whereas, the nucleate boiling component depends also on heat flux [172]. Assuming a thin thermal boundary layer and correlation provided by Tawfek et al. [173] (for h_{sp}) and Li et al. [174] (for h_{nb}), the two-phase heat transfer coefficient, h_{tp} = $\sqrt{h_{sp} + h_{nb}}$ is 12.9 kW/m^{2}K which is very close to what is achieved experimentally (17.2 - 18 kW/m^{2}K) for heat flux of 60 W/cm^2. Conductive thermal resistance can be calculated by disintegrating the length into n number of control volumes. Thus, normal-to-plane thermal resistance in Titanium thin film and FS substrate is estimated as $R^{Ti}_{cond.(n)} = L/(K_{Ti} \times n \times d \times t_{Ti})$ and $R^{FS}_{cond.(n)} = L/(K_{Ti} \times n \times d \times t_{FS})$, respectively. Moreover, in-plane thermal resistance in Titanium thin film and FS substrate is estimated as $R^{Ti}_{cond.(p)} = n \times d/(K_{Ti} \times L \times t_{Ti})$ and $R^{FS}_{cond.(p)} = n \times d/(K_{Ti} * L * t_{FS})$, respectively [28]

Assuming the ambient condition at T_{air} = 20C and h_{air} = 50 W/m^{2}k [172], the thermal resistance can be calculated from FS substrate to air ($R^{FS-air}_{cond.(n)}$+ $R^{FS-air}_{cond.(p)}$) and Ti to air ($R^{Ti-air}_{cond.(p)}$). The lateral (in-plane) thermal resistance is very large (5.81 $\times$ 10^6 K/W). Additionally, the thermal time constant (τ_s) can be calculated by assuming a lumped system. It is found that $\tau_s = \rho_{Ti} \times A_{Ti} \times t_{Ti} \times Cp_{Ti}/(h_{tp} \times A_{Ti})$ = 12.6 μ s led to diffusion length of l_d = $\sqrt{(\alpha_{Ti} \times \tau_s)}$ = 1.45 μ m. Due to this extreme thinness of the Ti film ($t_{Ti} << l_d$), the thermal inertial effect is neglected.

Table A.1: Thermal resistances at different layers/regions of the heater/sensor

Layers/Regions	Thermal resistance (K/W)
Water (two-phase)	3.0504
Ti (normal)	6.67×10^{-6}
Ti (in-plane)	5.81×10^{6}
FS (normal)	26.67
FS (in-plane)	15.8
FS to air	170.8
Ti to air	84.2×10^{6}

Error propagation analysis

The heat flux ($q^{''}$), surface temperature at the stagnation zone are measured using IR thermal camera, (T_s^{stag}), and fluid temperature using K-type thermocouple (T_f) with uncertainties of $\delta q^{''}$, δT_s^{stag}, and δT_f, respectively. The purpose of this is to determine maximum heat transfer coefficient (HTC_{max}) which is a function of $q^{''}$, T_s^{stag}, and T_f. This is given by Newton's law of cooling-

$$HTC_{max} = \frac{q^{''}}{T_s^{stag} - T_f} \tag{A.1}$$

The uncertainty in HTC_{max} is-

$$\delta HTC_{max} = \sqrt{(\frac{\partial HTC_{max}}{\partial q^{''}}\delta q^{''})^2 + (\frac{\partial HTC_{max}}{\partial T_s^{stag}}\delta T_s^{stag})^2 + (\frac{\partial HTC_{max}}{\partial T_f}\delta T_f)^2} \tag{A.2}$$

The partial derivatives are-

$$\frac{\partial HTC_{max}}{\partial q^{''}} = \frac{1}{T_s^{stag} - T_f}, \frac{\partial HTC_{max}}{\partial T_s^{stag}} = \frac{-q^{''}}{(T_s^{stag} - T_f)^2}, \frac{\partial HTC_{max}}{\partial T_f} = \frac{q^{''}}{(T_s^{stag} - T_f)^2} \tag{A.3}$$

Here, voltage/current measurement errors result in $\pm 3\%$ uncertainty in heat flux calculation ($\delta q^{''}$). Calibration curve in Fig. 2.3 of manuscript provides uncertainties in surface temperature in the stagnation zone using IR thermal camera recording (δT_s^{stag}). Uncertainty in fluid temperature measurement (δT_f) is caused by thermocouple's reading error of $\pm 1.1°$C.

Accuracy of Thermal Camera Reading

The accuracy of temperature values may change with focusing distance. However, this is only true for higher working distance and is mainly due to the atmospheric attenuation. Depending on the thermal camera's ability, some attenuation can be highly significant within few meters to kilometers of distance between the object and thermal imaging camera [175]. Before installation and implementation of the thermal imaging camera, it is made sure that it is setup at a distance from where temperature information could be captured accurately. FLIR SC7650 thermal imaging camera had a horizontal Field of View (FOV) of 24 degree, a resolution of 640 x 512 pixels, and needs a minimum working distance of 0.5m. Thus, the Instantanous Field of View (IFOV) is (24/640)*(pi/180) = 0.60 mrad. Since the heater size is 1cm x 1cm, the distance from the object is L_{FLIR} = 1x10^{-2}/(0.60x$10^{-}3$)= 16.67m. This is the distance up to which temperature can be measure accurately. In our thermal imaging experiments, the camera is setup at L_{exp}= 0.8m from the heater so that 0.5m $< L_{exp} < L_{FLIR}$ and thus the accurate reading is ensured.

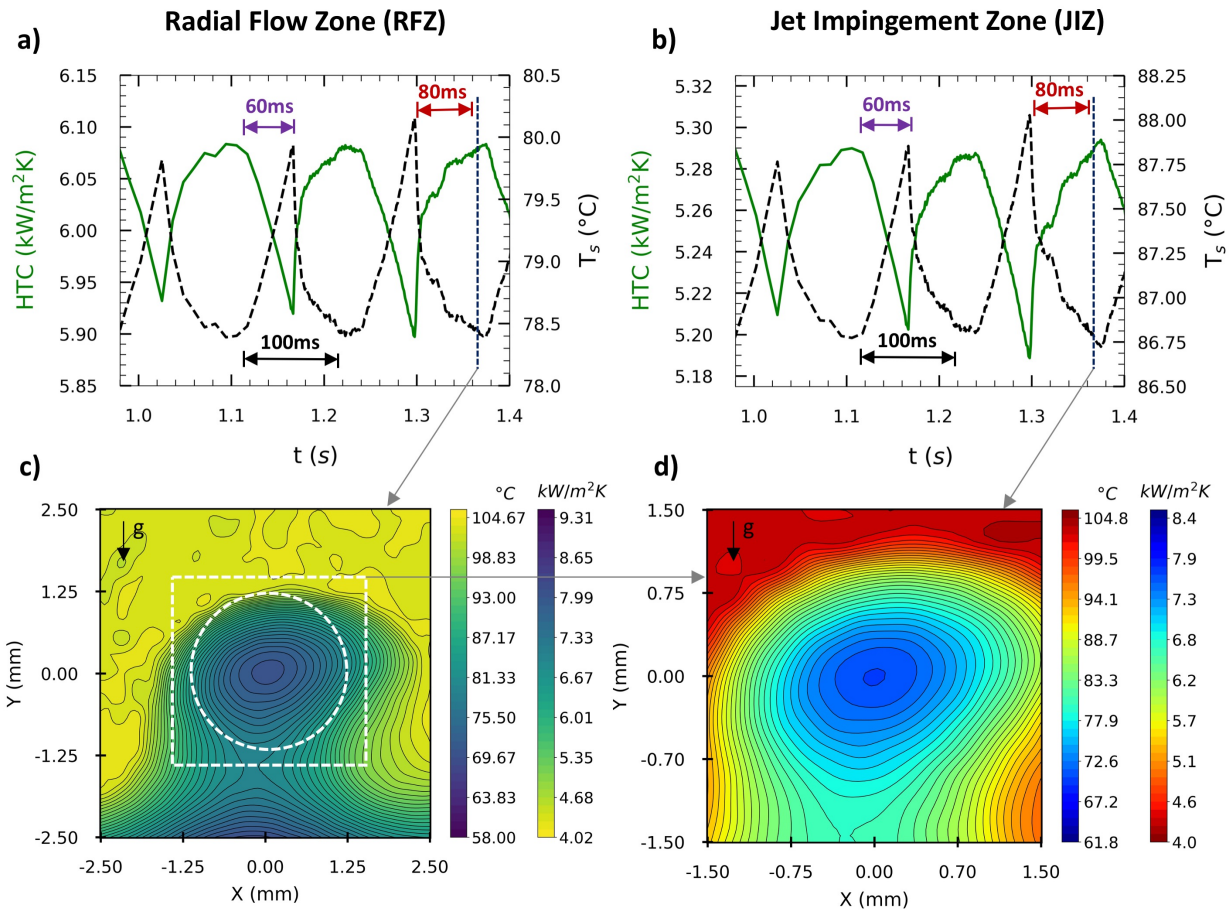

Figure A.4: Overview of key spatiotemporal temperature and HTC data for pulsed jet cooling using IR thermography. (a) Temporal HTC [left-axis] the Ti thin-film (wall/interface) temperature [right-axis]. The data corresponds to area-averaged values within the Radial Flow Zone (RFZ). (b) Temporal HTC [left-axis] the Ti thin-film (wall/interface) temperature [right-axis]. The data corresponds to area-averaged values within the Jet Impingement Zone (JIZ). (c) IR temperature map and corresponding HTC distribution at $t \approx 1.38$ seconds. (d) Zoom-view of the radial-flow-zone (RFZ) and corresponding jet impingement zone (JIZ) within it. Experimental details: $t \approx 1.38$ s (relative to the start of IR data acquisition), $q'' = 34 \pm 2$ W/cm^2, f_p=7.99$\pm$0.77 Hz, $T_{jet} \approx 22.5$°C, $D_{jet} \approx 410\mu$m, $G \approx 795$ kg/m^{2}s, Re ≈ 970, St ≈ 0.002, $H/D \approx 200$, and $z > 0$ into the page/images.

Through series of high heat flux experiments, cyclic boiling events are observed at radial locations of the pulsating jet. The cyclic boiling event consists of three major phases - i) bubble growth,

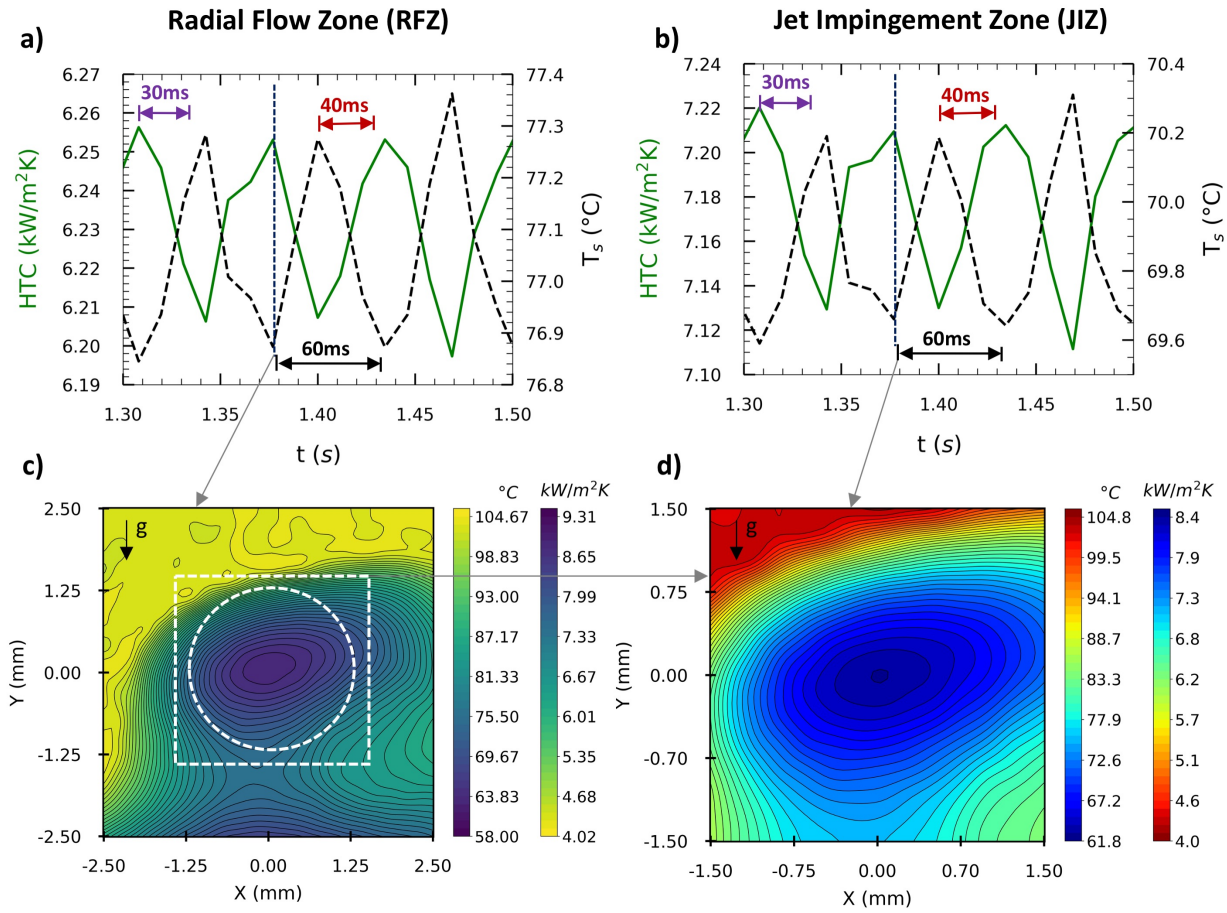

Figure A.5: Overview of key spatiotemporal temperature and HTC data for pulsed jet cooling using IR thermography. (a) Temporal HTC [left-axis] the Ti thin-film (wall/interface) temperature [right-axis]. The data corresponds to area-averaged values within the Radial Flow Zone (RFZ). (b) Temporal HTC [left-axis] the Ti thin-film (wall/interface) temperature [right-axis]. The data corresponds to area-averaged values within the Jet Impingement Zone (JIZ). (c) IR temperature map and corresponding HTC distribution at $t \approx 1.38$ seconds. (d) Zoom-view of the radial-flow-zone (RFZ) and corresponding jet impingement zone (JIZ) within it. Experimental details: $t \approx 1.38$ s (relative to the start of IR data acquisition), $q'' = 34 \pm 2$ W/cm^2, $f_p = 14.95 \pm 0.97$ Hz, $T_{jet} \approx 22.5$°C, $D_{jet} \approx 410 \mu$m, $G \approx 795$ kg/m^{2}s, Re ≈ 970, St ≈ 0.003, $H/D \approx 200$, and $z > 0$ into the page/images.

ii) bubble collapse/dry-out, iii) rewetting. It is important to understand the physical mechanism and role of each phases. The heated Titanium surface carries numerous microscale cavities, faults due to fabrication process (sputtering and thermal oxidation). According to the Bankoff's popular

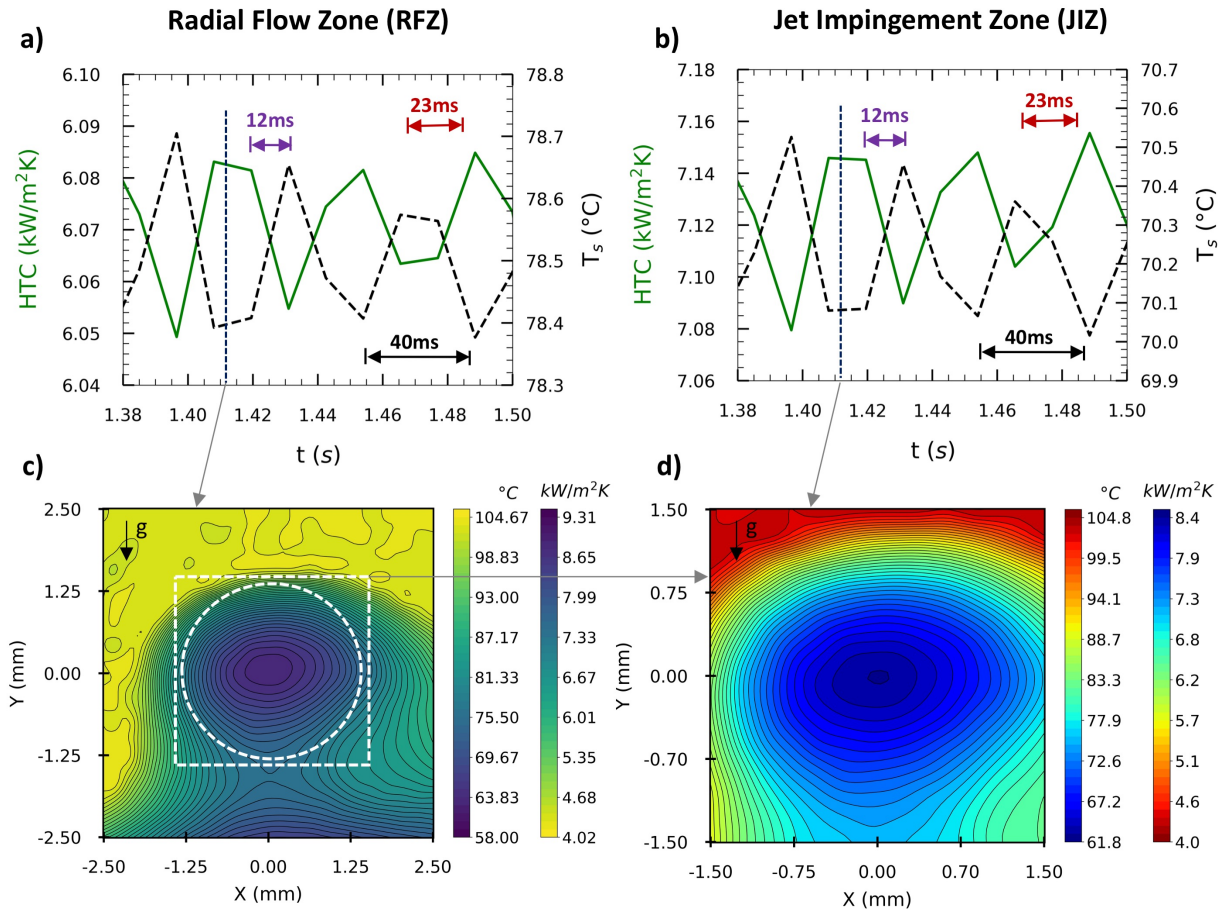

Figure A.6: Overview of key spatiotemporal temperature and HTC data for pulsed jet cooling using IR thermography. (a) Temporal HTC [left-axis] the Ti thin-film (wall/interface) temperature [right-axis]. The data corresponds to area-averaged values within the Radial Flow Zone (RFZ). (b) Temporal HTC [left-axis] the Ti thin-film (wall/interface) temperature [right-axis]. The data corresponds to area-averaged values within the Jet Impingement Zone (JIZ). (c) IR temperature map and corresponding HTC distribution at $t \approx 1.41$ seconds. (d) Zoom-view of the radial-flow-zone (RFZ) and corresponding jet impingement zone (JIZ) within it. Experimental details: $t \approx 1.41$ s (relative to the start of IR data acquisition), $q'' = 34 \pm 2$ W/cm^2, f_p=25.21$\pm$2.81 Hz, $T_{jet} \approx 22.5$°C, $D_{jet} \approx 410\mu$m, $G \approx 795$ kg/m^{2}s, Re ≈ 970, St ≈ 0.0045, $H/D \approx 200$, and $z > 0$ into the page/images.

Vapor Entrapment Theory [176], these cavities trap vapor and are called as nucleations sites. Depending on the factors that control ebullition, these nucleation sites can be classified as active and dormant. These nucleation sites, being randomly distributed on the surface, promotes two-phase

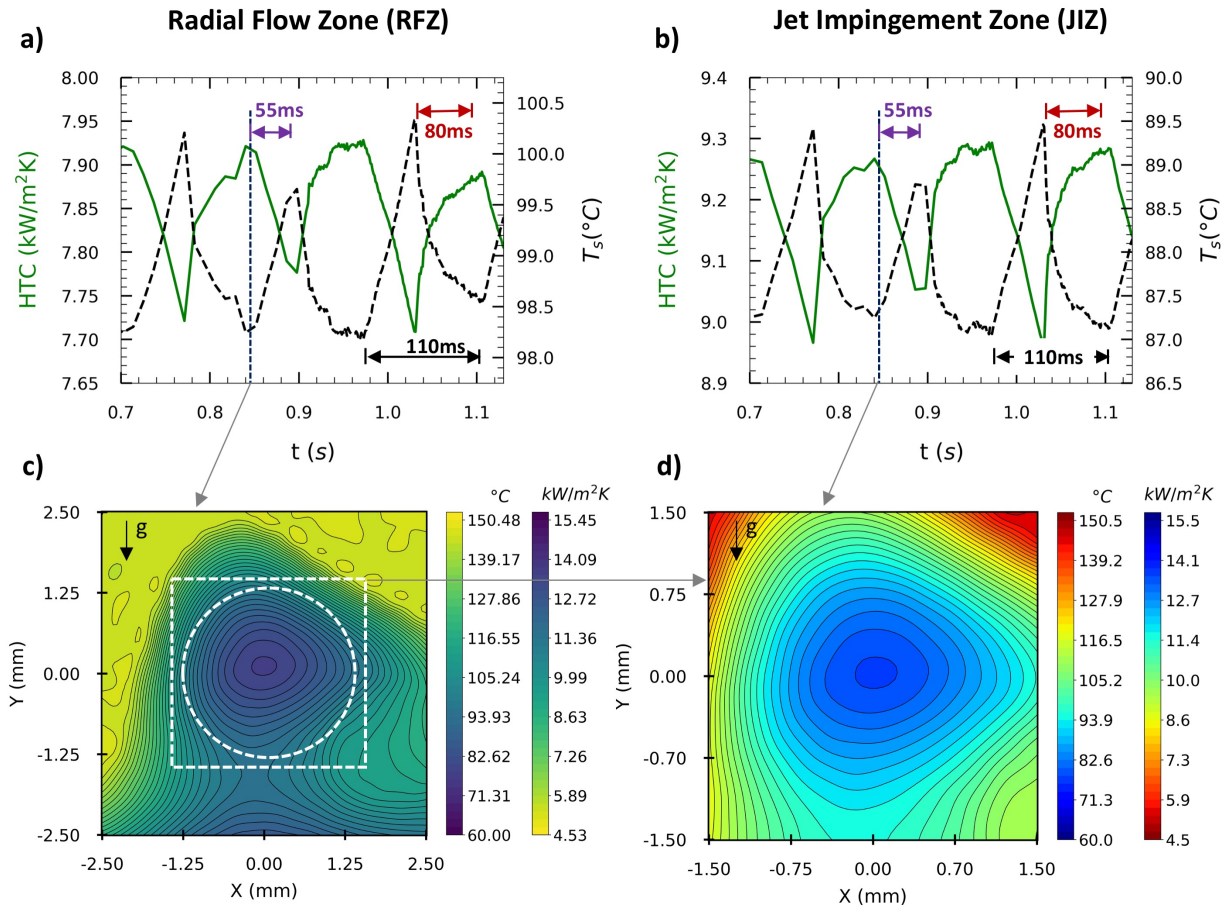

Figure A.7: Overview of key spatiotemporal temperature and HTC data for pulsed jet cooling using IR thermography. (a) Temporal HTC [left-axis] the Ti thin-film (wall/interface) temperature [right-axis]. The data corresponds to area-averaged values within the Radial Flow Zone (RFZ). (b) Temporal HTC [left-axis] the Ti thin-film (wall/interface) temperature [right-axis]. The data corresponds to area-averaged values within the Jet Impingement Zone (JIZ). (c) IR temperature map and corresponding HTC distribution at $t \approx 0.87$ second. (d) Zoom-view of the radial-flow-zone (RFZ) and corresponding jet impingement zone (JIZ) within it. Experimental details: $t \approx 0.87$ s (relative to the start of IR data acquisition), $q'' = 60 \pm 2$ W/cm^2, f_p=7.99$\pm$0.77 Hz, $T_{jet} \approx 22.5$°C, $D_{jet} \approx 410\mu$m, $G \approx 795$ kg/m^{2}s, Re ≈ 970, St ≈ 0.002, $H/D \approx 200$, and $z > 0$ into the page/images.

events. Essentially, such nucleation is influenced by surface tension of the liquid, inertia force and pressure difference between the trapped vapor layer and surrounding liquid. In the subcooled regime, inside pressure of these vapor traps is larger than the surrounding working fluid and bub-

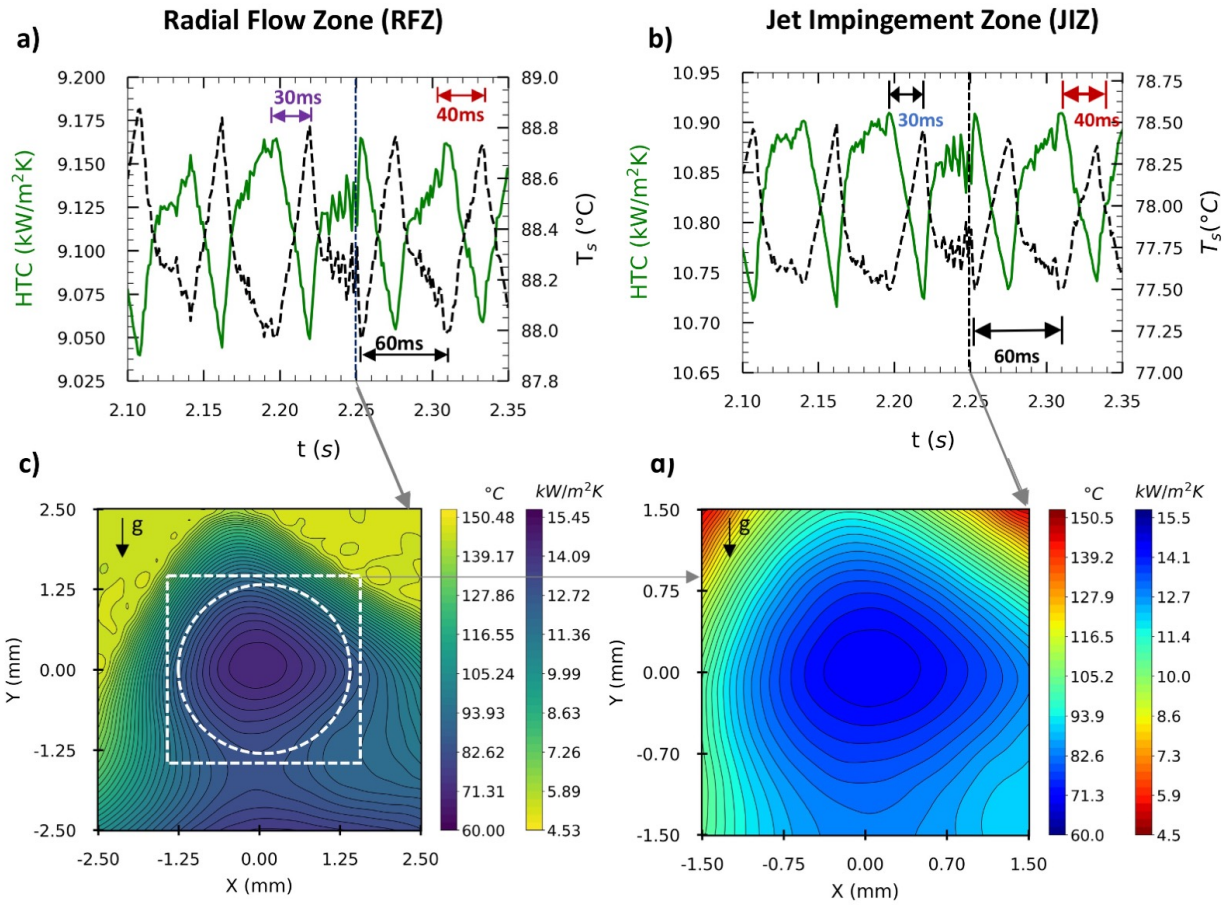

Figure A.8: Overview of key spatiotemporal temperature and HTC data for pulsed jet cooling using IR thermography. (a) Temporal HTC [left-axis] the Ti thin-film (wall/interface) temperature [right-axis]. The data corresponds to area-averaged values within the Radial Flow Zone (RFZ). (b) Temporal HTC [left-axis] the Ti thin-film (wall/interface) temperature [right-axis]. The data corresponds to area-averaged values within the Jet Impingement Zone (JIZ). (c) IR temperature map and corresponding HTC distribution at $t \approx 1.19$ seconds. (d) Zoom-view of the radial-flow-zone (RFZ) and corresponding jet impingement zone (JIZ) within it. Experimental details: $t \approx$ 2.25 s (relative to the start of IR data acquisition), $q'' = 60 \pm 2$ W/cm^2, $f_p = 14.95 \pm 0.97$ Hz, $T_{jet} \approx 22.5$°C, $D_{jet} \approx 410\mu$m, $G \approx 795$ kg/m^{2}s, Re ≈ 970, St ≈ 0.003, $H/D \approx 200$, and $z > 0$ into the page/images.

ble does not grow. Therefore, at lower input heat flux (20 W/cm^2), no bubble growth is observed experimentally. However, as the heat flux increases from 20 W/cm^2 to 60 W/cm^2, the surrounding working fluid (in our case, water) at radial locations reaches saturation condition, and eventually

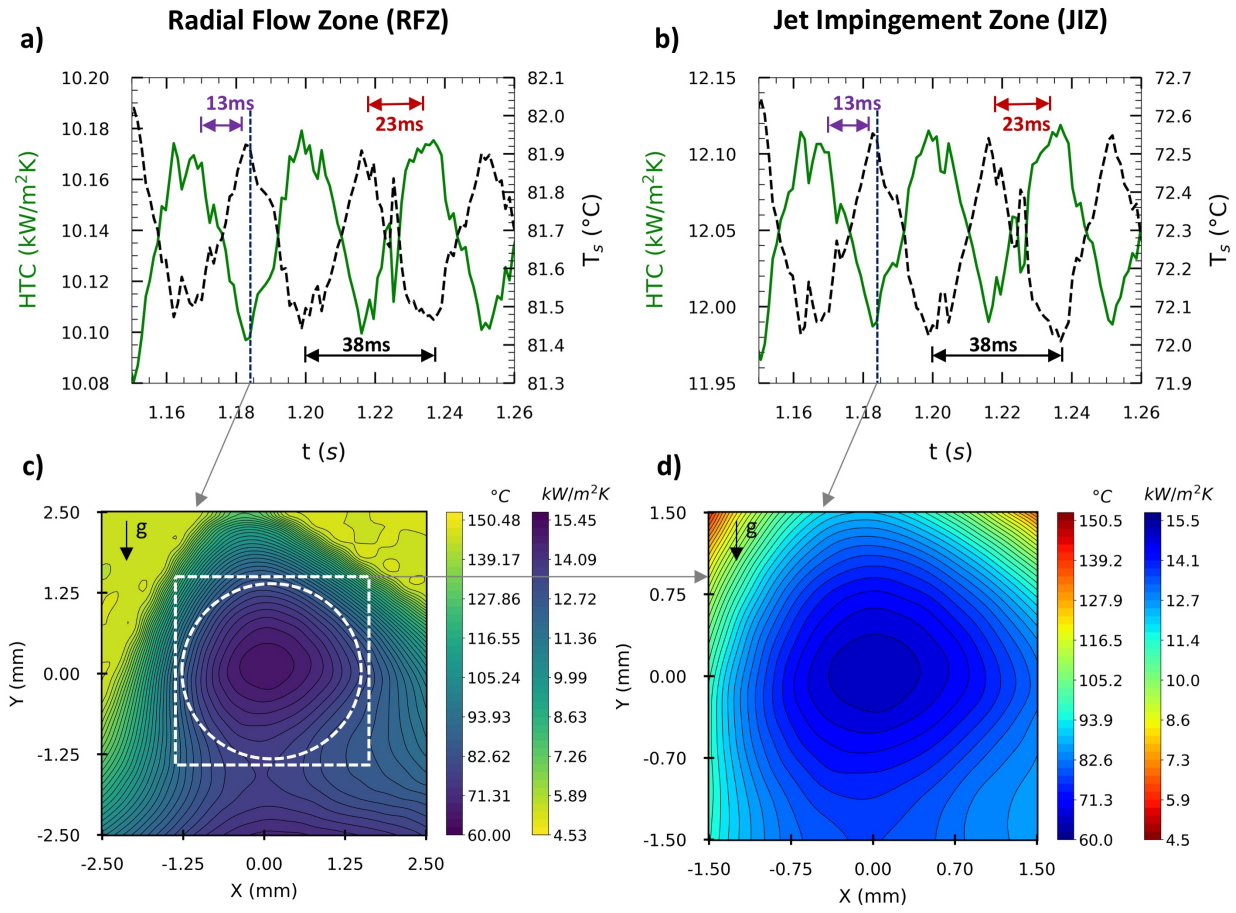

Figure A.9: Overview of key spatiotemporal temperature and HTC data for pulsed jet cooling using IR thermography. (a) Temporal HTC [left-axis] the Ti thin-film (wall/interface) temperature [right-axis]. The data corresponds to area-averaged values within the Radial Flow Zone (RFZ). (b) Temporal HTC [left-axis] the Ti thin-film (wall/interface) temperature [right-axis]. The data corresponds to area-averaged values within the Jet Impingement Zone (JIZ). (c) IR temperature map and corresponding HTC distribution at $t \approx 1.19$ seconds. (d) Zoom-view of the radial-flow-zone (RFZ) and corresponding jet impingement zone (JIZ) within it. Experimental details: $t \approx 1.19$ s (relative to the start of IR data acquisition), $q'' = 60 \pm 2$ W/cm^2, f_p=25.21$\pm$2.81 Hz, $T_{jet} \approx 22.5$°C, $D_{jet} \approx 410\mu$m, $G \approx 795$ kg/m^{2}s, Re ≈ 970, St ≈ 0.0045, $H/D \approx 200$, and $z > 0$ into the page/images.

becomes superheated. For this reason, the pressure inside the vapor bubble becomes larger than the surrounding water. Thus the nucleation starts and bubble starts to grow. This is thermal diffusion controlled growth [177]. Griffith [178] observed that when the chemical potential is similar to that of vapor, nucleation happened. They combined Calusias-Capyron model with Young-laplace equation to quantify this condition. Further bubble growth depends on wall superheat and wetting characteristics. By performing force balance between surface tension force and buoyancy force at

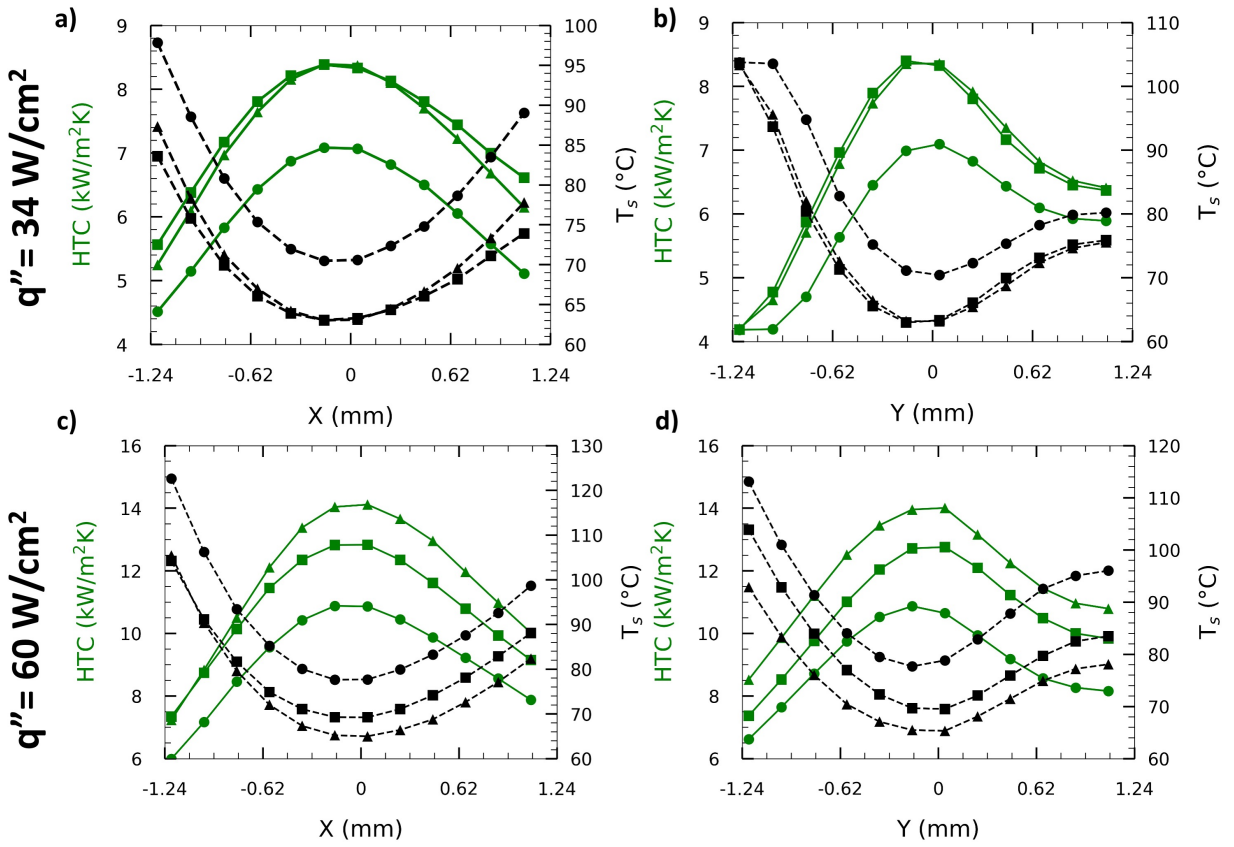

Figure A.10: Spatiotemporal temperature (right axis) and HTC distribution (left axis) for pulsed jet cooling using IR thermography for heat flux of $q^{''} = 60\pm2$ W/cm^2 (a,b), and $q^{''} = 60\pm2$ W/cm^2 (c,d). Here black dashed lines and green solid lines correspond to temperature profile, and HTC profile, respectively. Moreover, symbols of circle, square, and triangle, represent pulsation frequencies of 7.99±0.77 Hz, 14.95±0.97 Hz and 25.21±2.81 Hz, respectively at $T_{jet} \approx 22.5$°C, $D_{jet} \approx 410\mu$m, $G \approx 795$ kg/m^{2}s, Re ≈ 970, $H/D \approx 200$.

the solid-liquid interface, maximum bubble diameter can be derived. Using Fritz correlation and Bond length [179], maximum diameter of these bubbles at the radial locations of the heater are found to be between 0.7 mm to 5 mm. If semi-infinite conduction into the thermal boundary layer is assumed, it will be found that the time required for a bubble to collapse is 206 ms. Analytical value is overestimated as it considers micro-layer evaporation [8]. This micro-layer evaporation causes the wall superheat to decrease which eventually increases the departure/collapse time. Due to this collapse, dry-spot zones appear. These dry-spots, essentially, have two options - i) to expand or ii) to contract. These two mechanisms can be described by the force imbalances among static pressure force (due to gravity), capillary force (due to surface tension), and inertia force (due to impacting jet). Assuming a mean liquid film thickness of 100 μ m, the critical radius of these dry-spots are 0.2 mm [180]. At the radial locations, the static pressure force gets dominated by the capillary and inertia force. Thus the dry-spot zones diminish and the cycle repeats. Experimentally, it is observed tha the bubble growth, collapse and rewetting timescale corresponds to 12.5 Hz which is interestingly very close to the our experimentally-observed optimum pulsation frequency (16.7Hz). These cyclic boiling events only appear at higher heat fluxes where surface temperature is higher (e.g. 109C) than saturation temperature of water (see thermal maps in supplementary Fig 6, 7).

Thermo-Capillary Breakdown

As liquid droplet (generated by pulsating jets) comes in contact with the surface, a stable liquid film tries to develop. Since the surface mimics a heat flux boundary condition, the subcooled liquid film gets sensibly heated up. When the heat flux is greater than the breakdown heat flux [181], thermal transport into the liquid film introduces lateral surface tension gradients. When the surface tension force exceeds the hydrodynamic forces, bulk-fluid motion occurs [182] and

breakdown results. Another reason behind these breakdowns are evaporation in the thin film and nucleate boiling [181]. Such breakdowns end up forming thermocapillary structures [183, 184] on the heated surface which, eventually, destabilizes the system [185].

Optimum Pulsation Frequency and HTC

Equations (3)-(7) take the suppression of instability into account which leads to minimum mean liquid film thickness (due to pulsation). Minimum heated liquid film thickness (due to heat transfer from a heated surface) can be scaled to maximum heat transfer co-efficient (HTC_{max}) [50]. This leads us to find the optimum pulsation frequency (fka) for maximum heat transfer co-efficient. Moreover, section C is meant to compare the natural wave formation frequency with the forced wave formation frequency that arises in pulsated flows. The optimization comes from the fact that the waves created "naturally" will have time to cause dry out, inducing phase change, but no additional time to heat up once dry, as the new "forced" wave immediately re-wets the area. This way of looking at the frequencies necessitates that equations (3) and (7) in the main manuscript be used in tandem. The roll off is predicted as a consequence, since faster pulsation frequencies become redundant with regards to re-wetting dried out areas. Since the Marangoni Number is a dimensionless quantity, the use of different fluids should be irrelevant to validity of the final equations. Zaitsev et al. [186] also performed tests with pure water as well. In the work of Lel et al. [187] the Marangoni number is not addressed in this way, but Fig. 2.5 demonstrates that the wave structures of the silicone oils operate on the same non-dimensional scales as water.

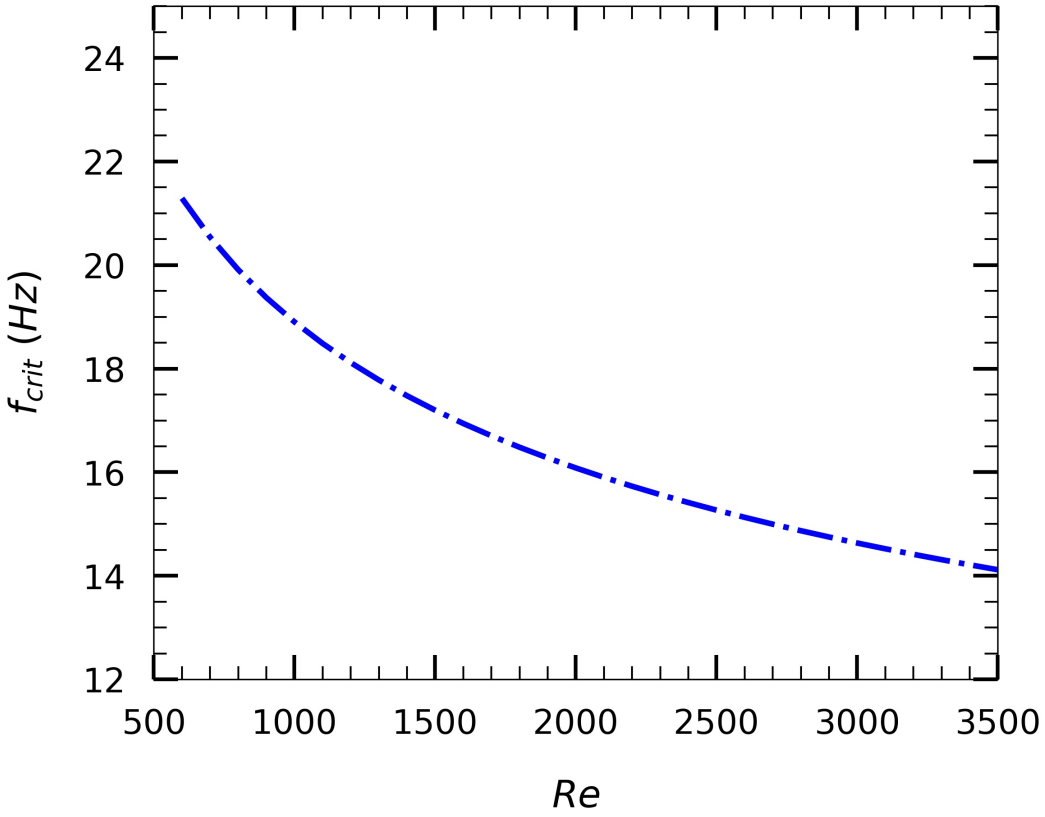

Figure A.11: The effect of Re on dominant perturbation frequency or mean critical pulsation frequency for gravity driven falling liquid film

Influence of Reynolds Number

The Reynolds number (Re) number influences jet performance in heat transfer augmentation. For instance, [188] observed 120% enhancement in single-phase Nusselt number (stagnation zone) when Re is increased from 34000 to 78000 at pulsation frequency of 200 Hz. Moreover, even higher enhancement is observed with synthetic jets by [14]. They observed 180% average Nusselt number enhancement as Reynolds numbers is varied from 1150 to 4180. As indicated by our discussions, optimum pulsation frequency dictates maximum heat transfer co-efficient (and Nusselt number). Therefore, it is important to understand how Reynolds number (Re) can influence

optimum pulsation frequency. The supplementary Fig.A.11 illustrates such a relationship between critical pulsation frequency and Re. Here, Eqns. 3-5 of manuscript is employed to calculate theoretical critical/optimum pulsation frequencies for Re = 250 - 2000. However, experiments are only performed at Re = 970 for this current study and therefore, experimental studies (with range of Re) with two-phase pulsating jet must be performed to justify such understanding in future investigation. The reason behind choosing Re = 970 is that it keeps external perturbation near the stagnation zone ($<$0.8 mm) of the jet. Using downstream flow model proposed by Lienhard [189], it is found the radius (r_o) at which the viscous layer reaches the liquid film is 0.71 mm. Moreover, the impact of jet at Reynolds number of 970 does not overwhelm the liquid film far away from the stagnation zone. This, effectively, reduces the chance of flooding (or rising of liquid sheet) which has been a recent concern in free surface single-phase jet impingement cooling [190, 191].

APPENDIX B: THERMAL MAPPING ADDITIONAL INFORMATION

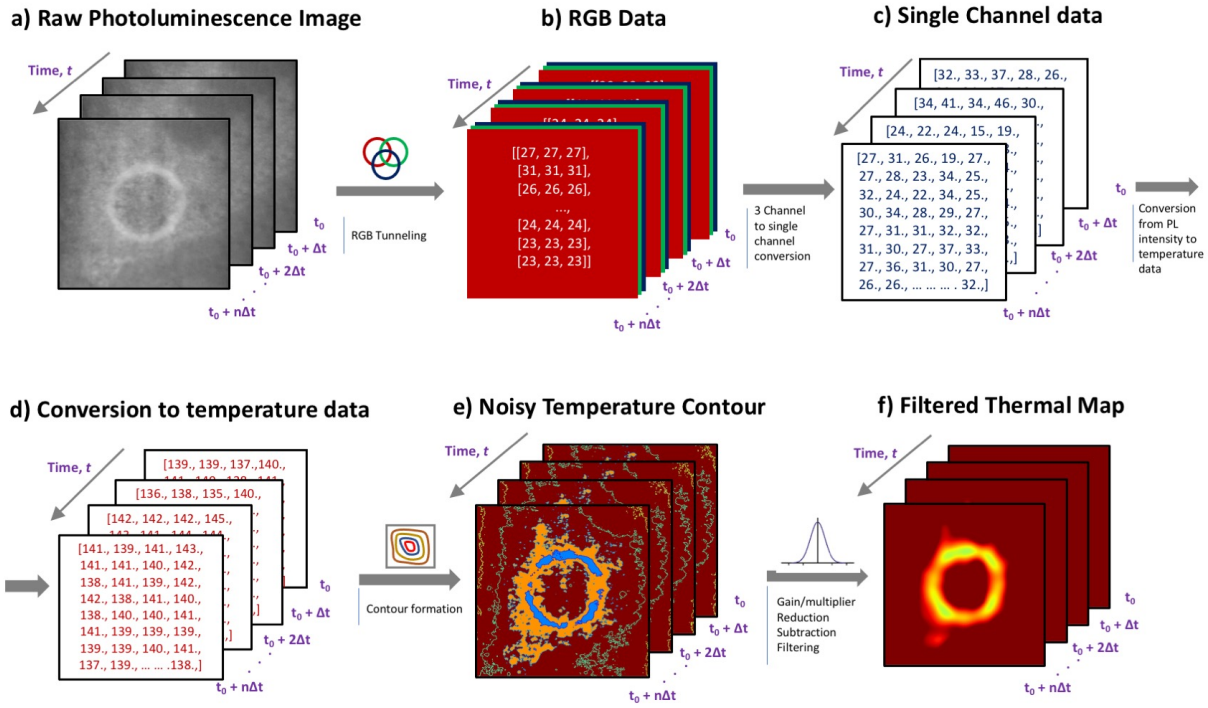

Figure B.1: The post processing of PL images. a) Raw Photoluminescence (PL) images are extracted from the high speed camera for number of frames, b) RGB values are extracted pixel-by-pixel, c) 3 channel values are converted to single channel value (Gray scale), d) Gray scale values are converted to temperature data using the calibration line, e) Contours are formed using the temperature values which include noise, f) Gaussian filter and gain are used to reveal the transient thermal maps.

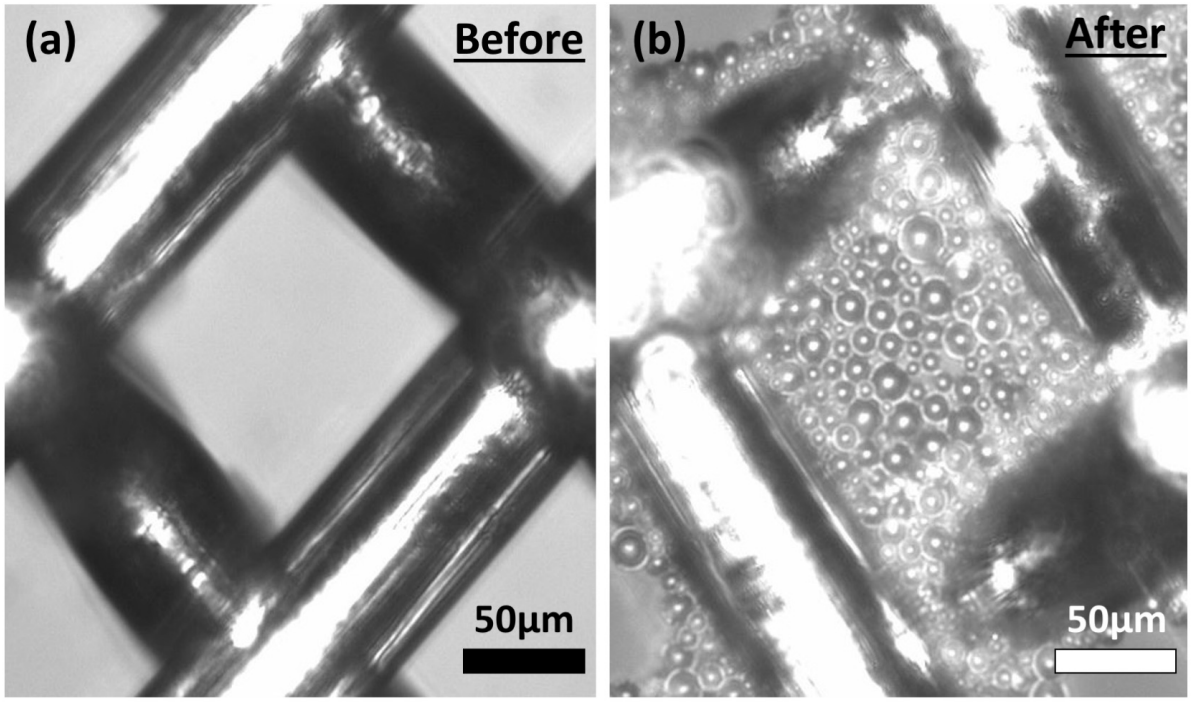

Figure B.2: The entrapment of micro beads in metallic meshes. a) 50μm sized copper mesh with rectangular void space, b) after performing controlled dipping of copper mesh in micro-bead solution, the uniform entrapment is found which is caused by capillary forces acted at the interfaces.

APPENDIX C: NANOPARTICLE SUSPENSIONS ADDITIONAL INFORMATION

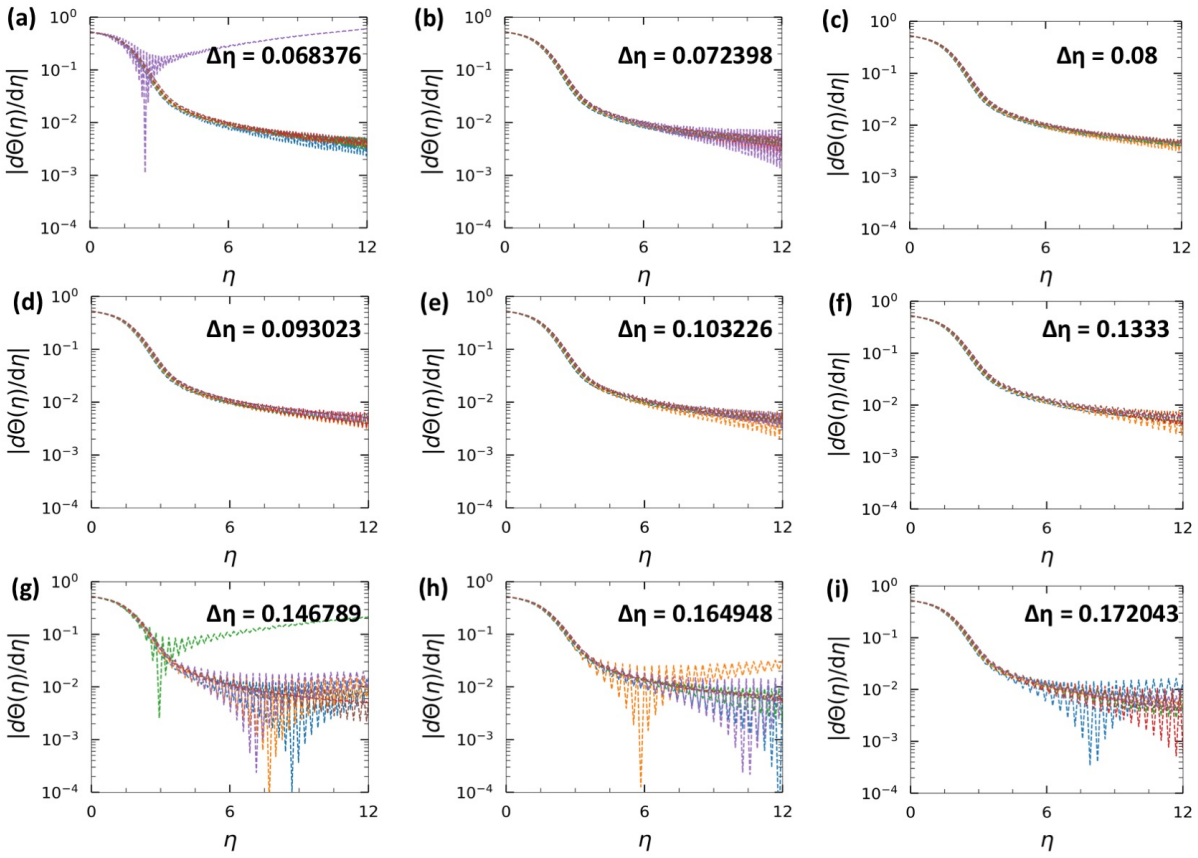

Figure C.1: (a-b) shows the influence of step of η on the profile of temperature gradient.

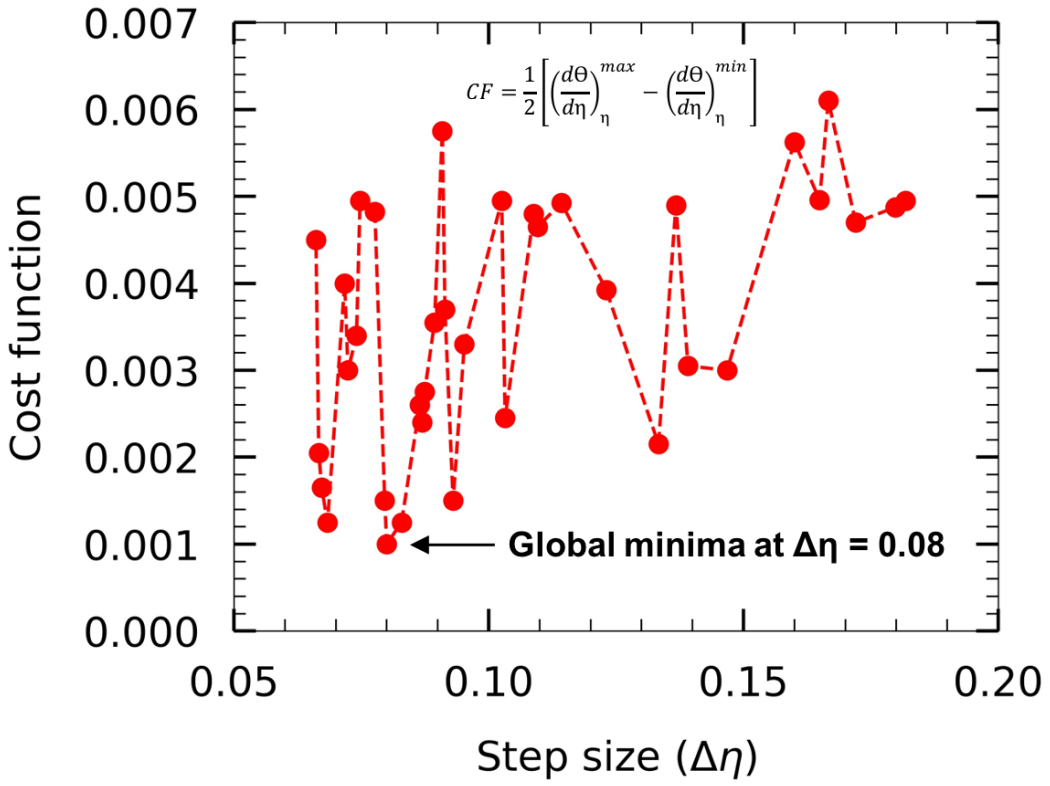

Figure C.2: Cost function (CF): The CF profile as a function of step size of η shows the global minima at $\delta\eta = 0.08$.

APPENDIX D: PHP DESIGN ADDITIONAL INFORMATION

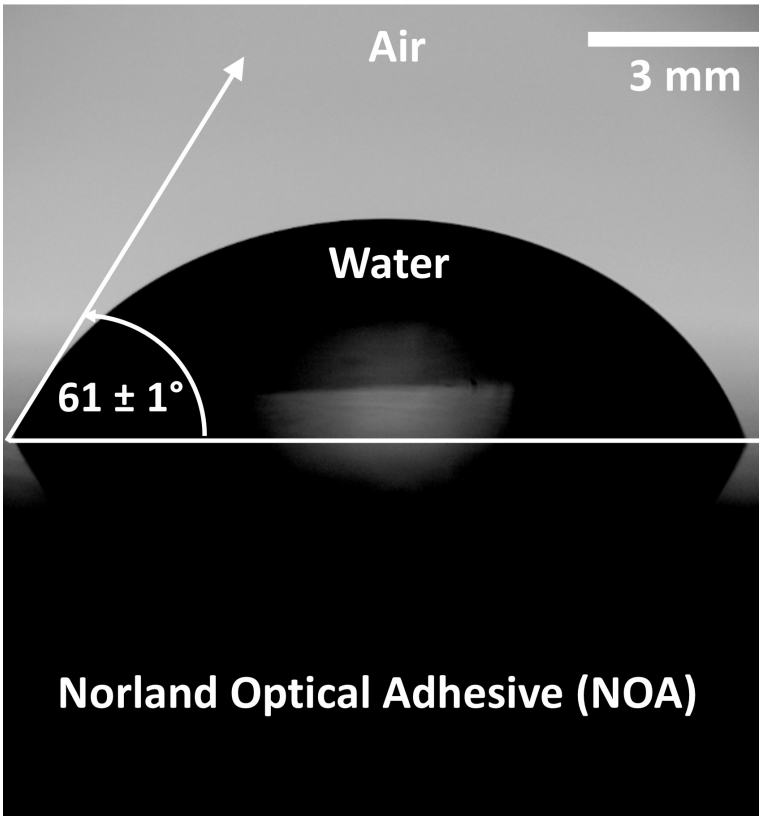

Figure D.1: Contact angle measurement: A water droplet (diameter = 10.88mm) is put on the flat and cleaned surface of Norland Optical Adhesive which is exposed to air in laboratory environment (24°C room temperature, 43% RH). Several measurements are made using Phantom HSV with 5X objective lens (13.71um/px resolution) at different locations of the solid surface and found consistency. Therefore others are not included in the figure to avoid redundancy. Each measurements show consistent contact angle values with an uncertainty value of 1°C. This measurement show that the surface is hydrophilic since the contact angle is below 90°C. This makes it a suitable material for heat transfer applications where surface wettability is important.

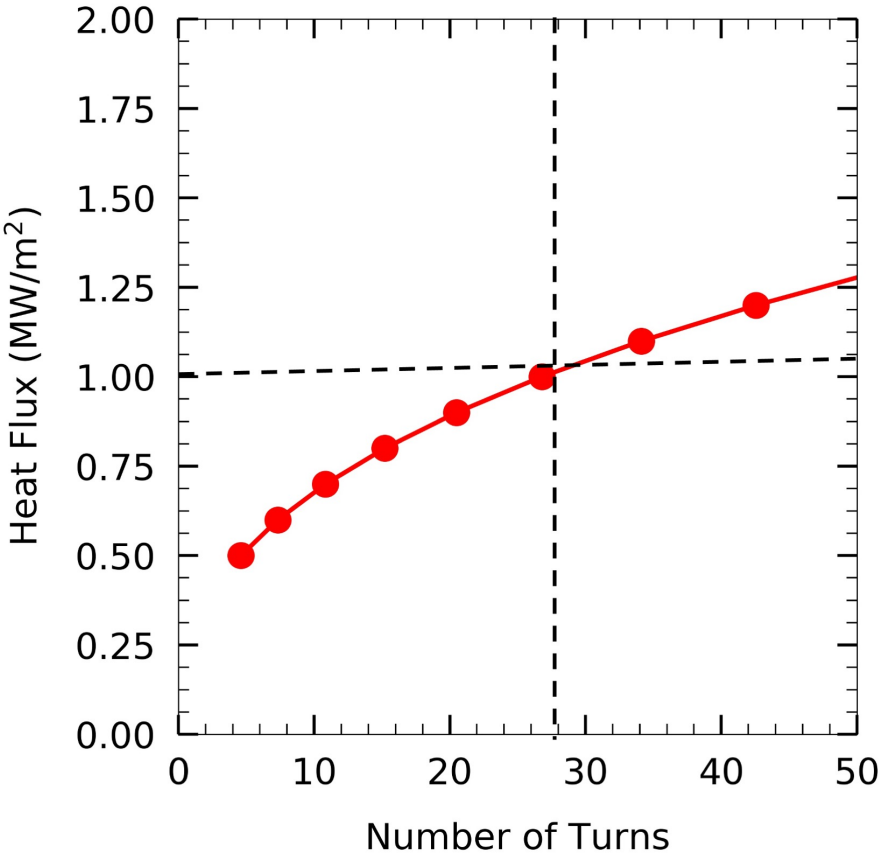

Figure D.2: Influence of number of turns on heat flux: The idea is to design a flexible pulsating heat pipe which has a potential of removing large amount of heat from a local heated section. To do that both single phase and two-phase heat transfer process need to be enhanced. The higher the number of turns in a PHP, the better the flow mixing and overall heat removal rate. According to the model provided by Kammuang et al. [1s], to remove at least 1MW/cm^2 heat, the PHP needs to have at least 28 number of turns. The corresponding Kuatelatze number, diameter of the channel, and critical vapor velocity plugged into the model are 0.12, 0.7mm, and 0.0022m/s, respectively. Obeying to these, PHPs of 33 number of turns are designed and fabricated for this investigation.

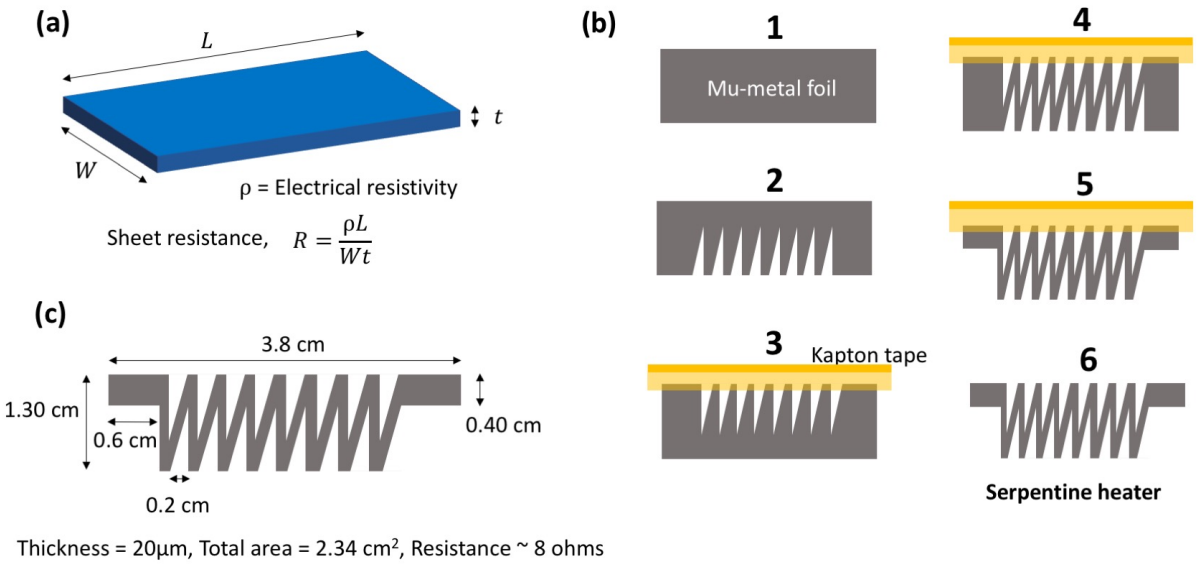

Figure D.3: Heater design and fabrication: Heaters should be of high resistance to provide higher heat fluxes. To achieve this, in foil heaters, the length needs to be increased and width needs to be decreased, as shown in (a). For this reason, the mu-metal foil heater (thickness, 20μm) is made in serpentine shape and cut using the step-by-step process mentioned in (b) using precise ceaser. This way the surface area could be reduced from 4.84cm^2 to 2.34cm^2, thus allowing more input heat fluxes and increasing the resistance from 2 ohms to 8 ohms. c) This shows the appropriate dimensions of the final serpentine shaped heater.

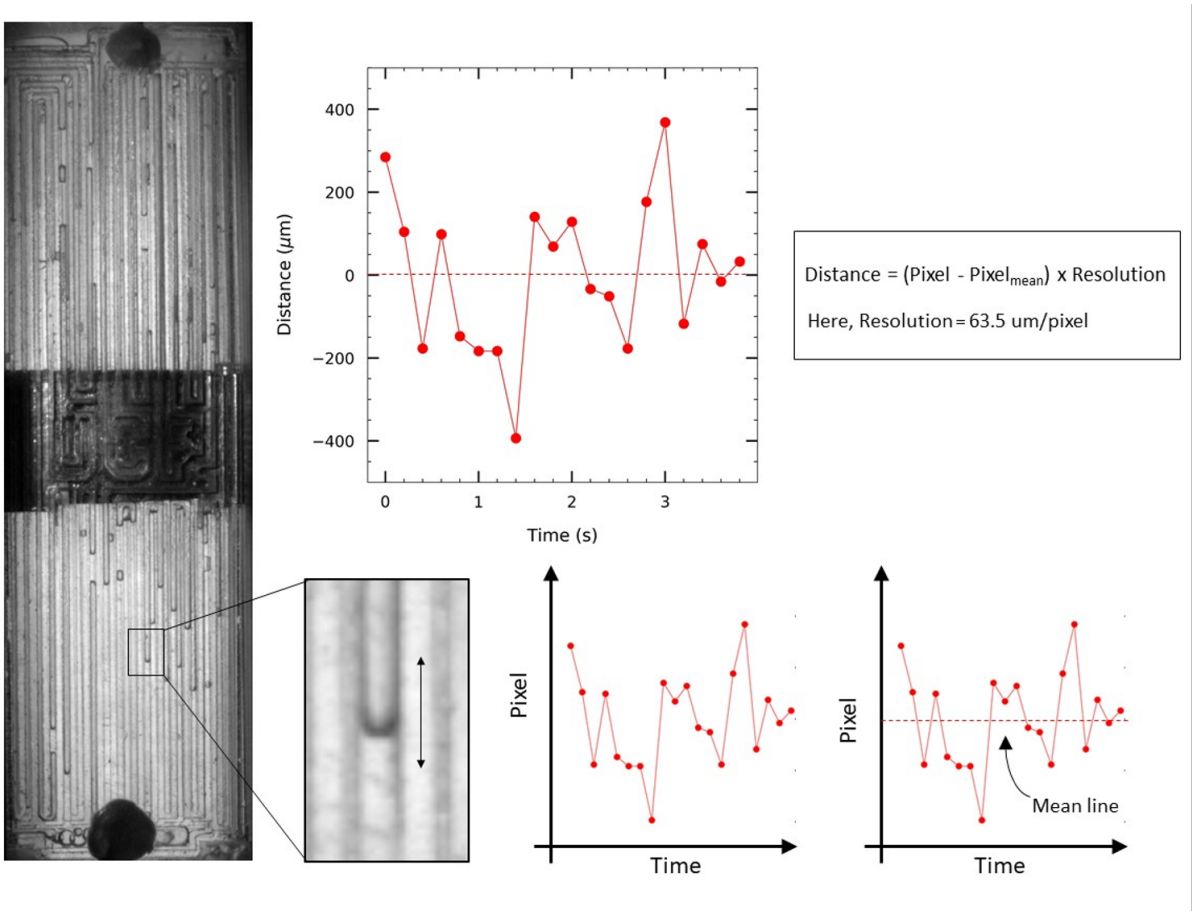

Figure D.4: Quantifying the pulsation magnitudes: Using the Phantom Cine Viewer program, going frame by frame for a particular liquid-vapor interface gives the change in pixel values over a period of time. Later these pixel values are averaged (geometric mean) for that period of time and relative pixel values are found assuming the mean line as the 'zero line'. Using the camera resolution of 63.5μm/pixel, the distance traveled by a liquid slug in a single channel in either top or bottom PHP is found, temporally. This process is performed for all the Regions of Interests (ROIs) for both the PHPs for a comparative illustration for different condensing conditions.

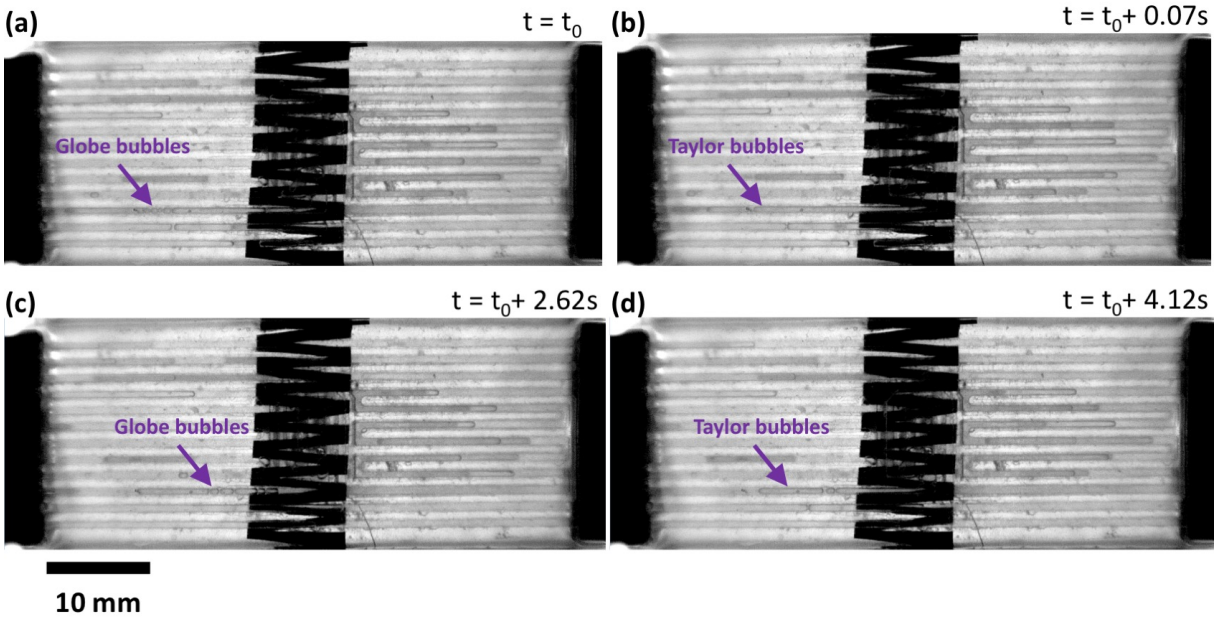

Figure D.5: Bubble formation during PHP operation: (a-b) shows pulsation mechanism for two-stack system from t_0 to t_0+ 4.12s. Globe bubbles form at the onset of nucleate boiling. Spontaneous heating causes these bubbles to grow and turn into larger Taylor bubbles. In all the snapshots, the liquid slugs and vapor plugs are visible in both the PHPs of the two-stack system.

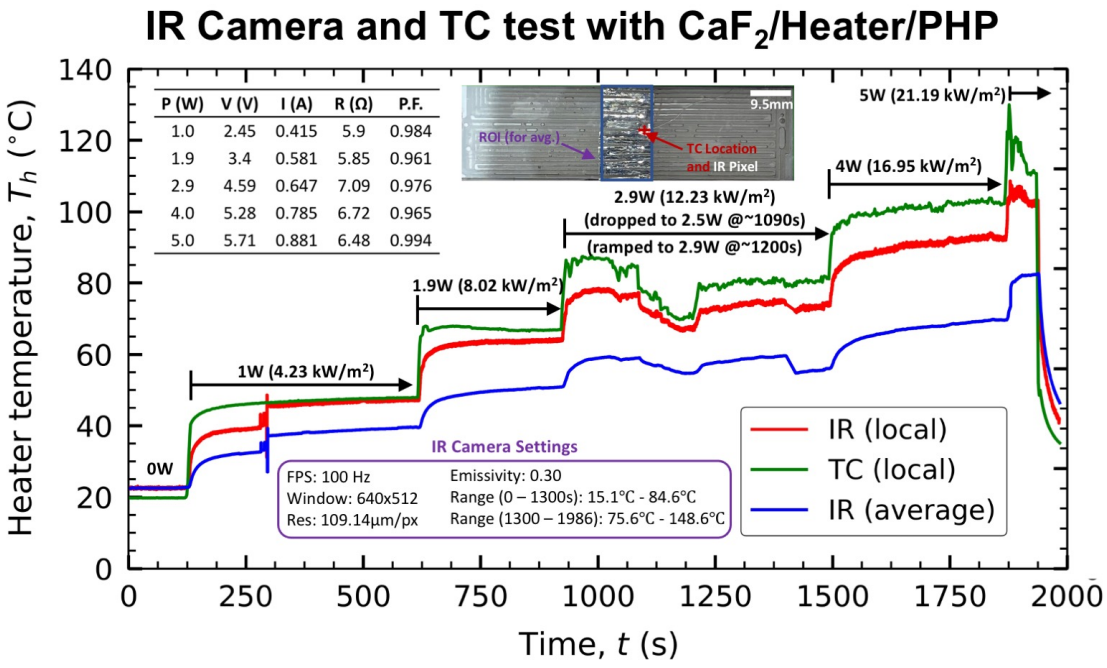

Figure D.6: Thermocouple calibration with IR thermal imaging using CaF_2 window.

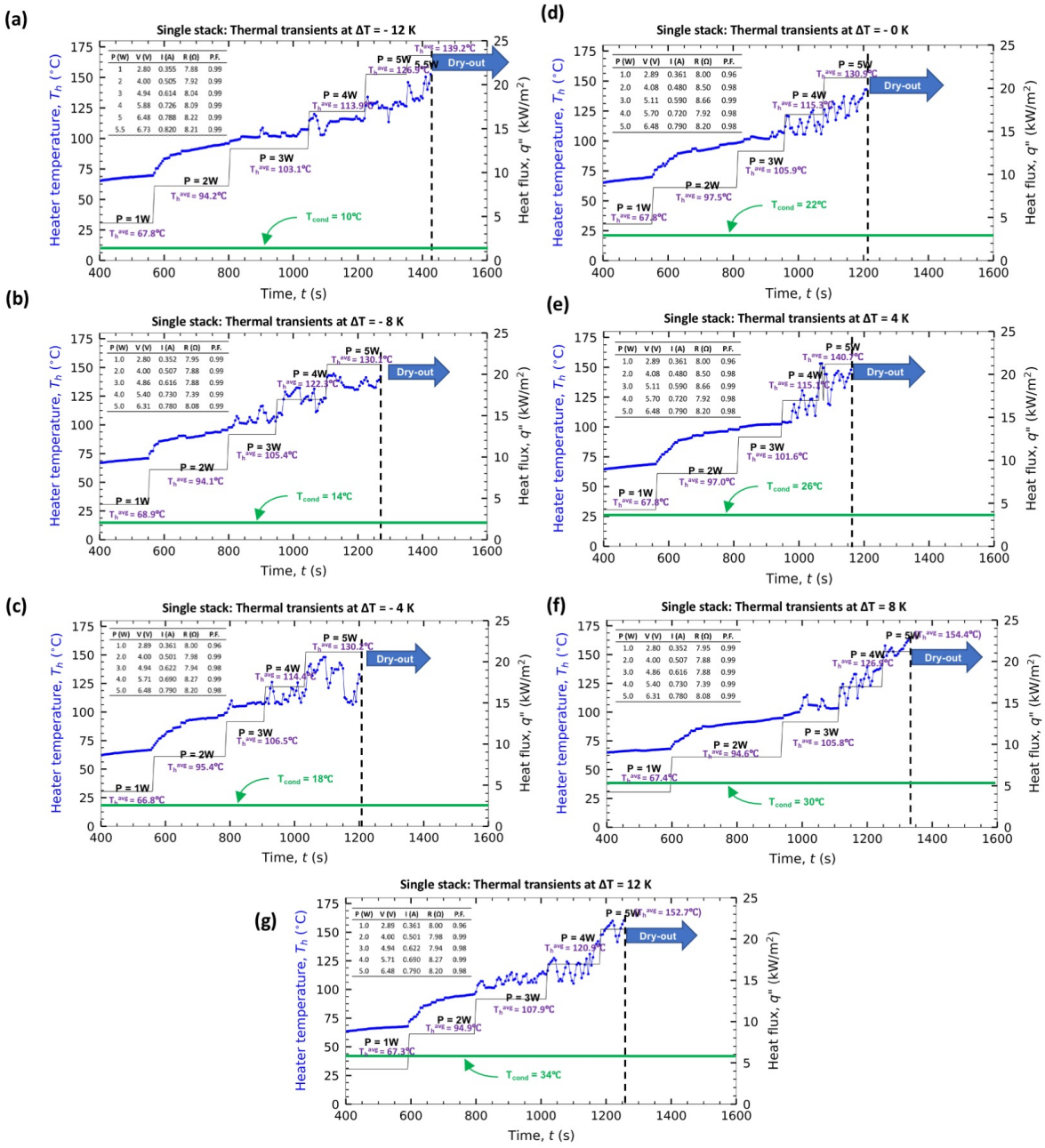

Figure D.7: Thermal transient data for single-layer PHP as a function of condenser temperatures (both top and bottom) and power loads.

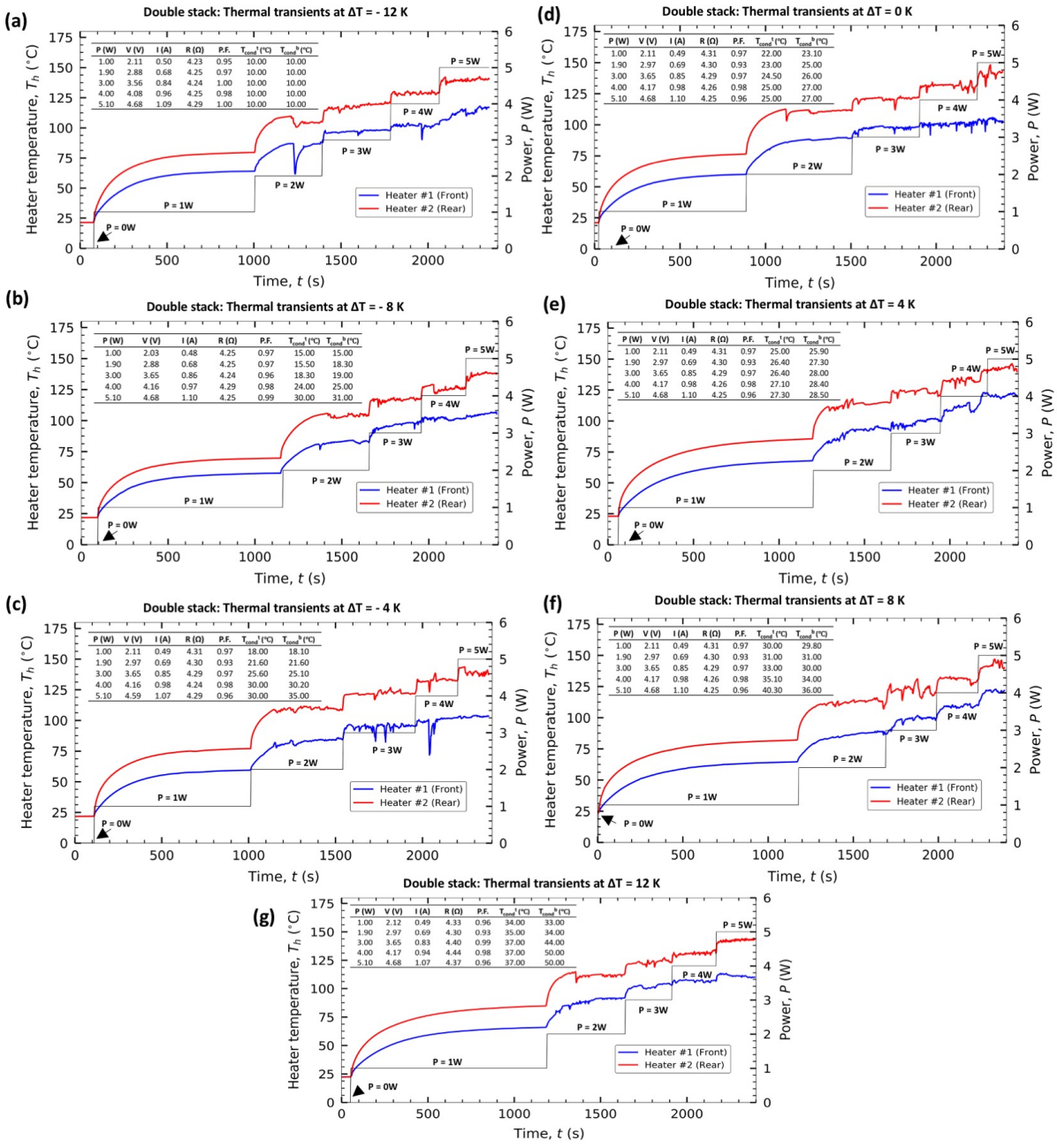

Figure D.8: Thermal transient data for double-layer PHP as a function of condenser temperatures (both top and bottom) and power loads.

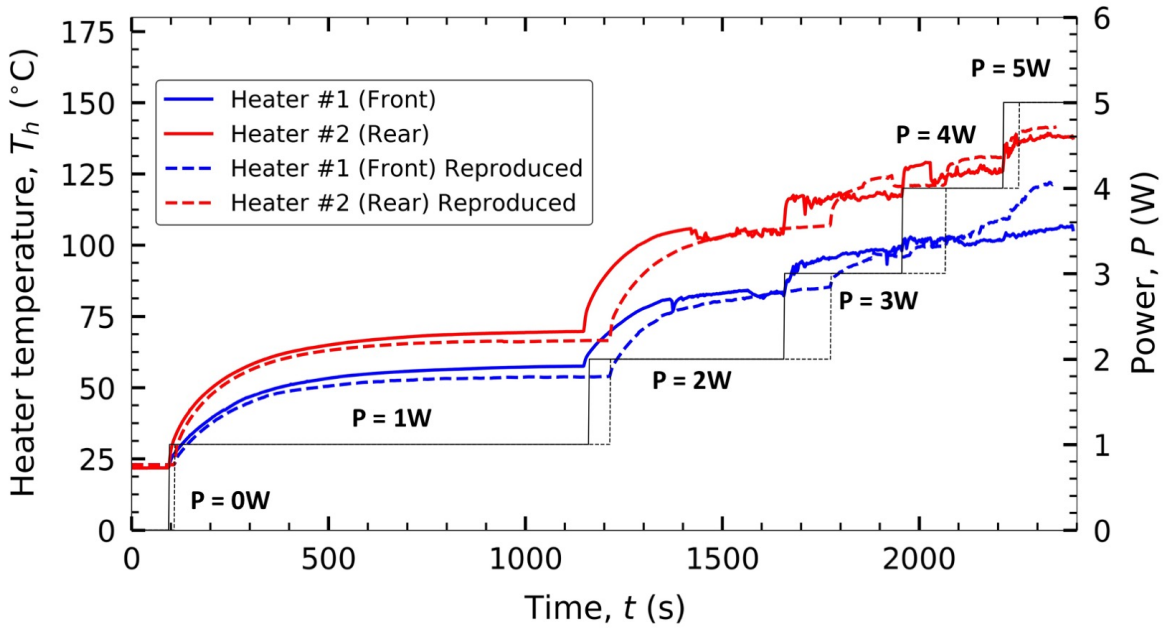

Figure D.9: Reproducing effort for 3D-stack PHP (double-layer).

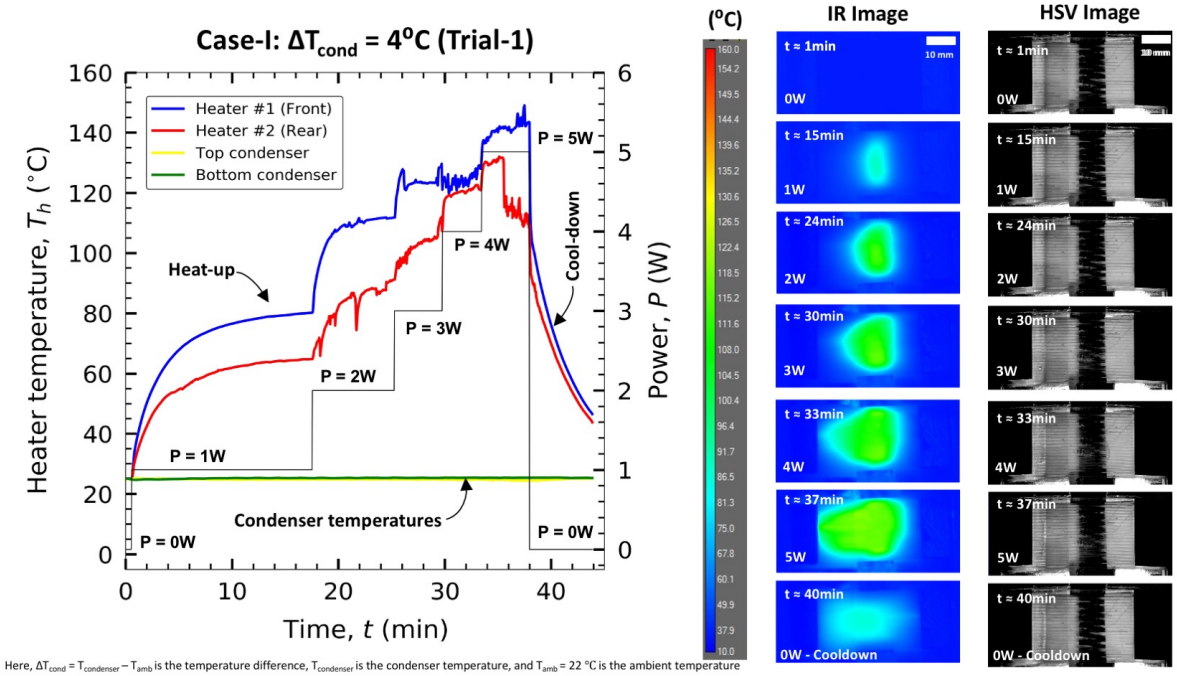

Figure D.10: Reproducing effort for 3D-stack PHP (double-layer) for relative condenser temperature of 4K (trial-1) along with IR and HSV snapshots.

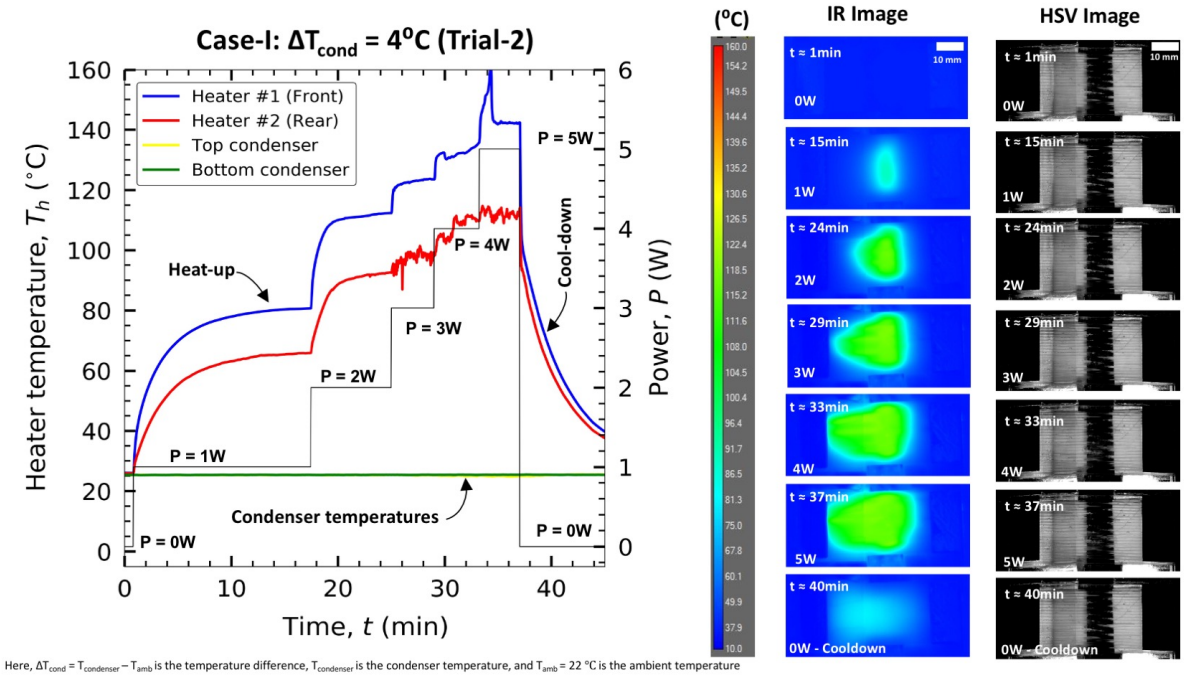

Figure D.11: Reproducing effort dataset for 3D-stack PHP (double-layer) for relative condenser temperature of 4K (trial-2) along with IR and HSV snapshots.

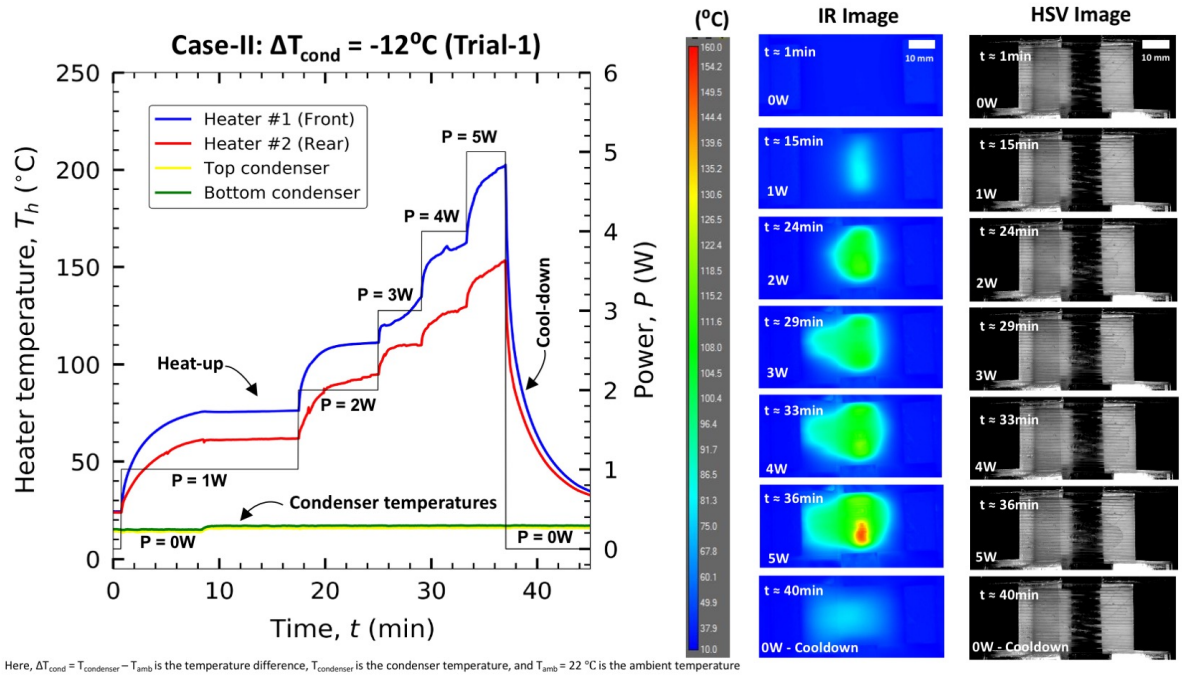

Figure D.12: Reproducing effort for 3D-stack PHP (double-layer) for relative condenser temperature of -12K (trial-1) along with IR and HSV snapshots.

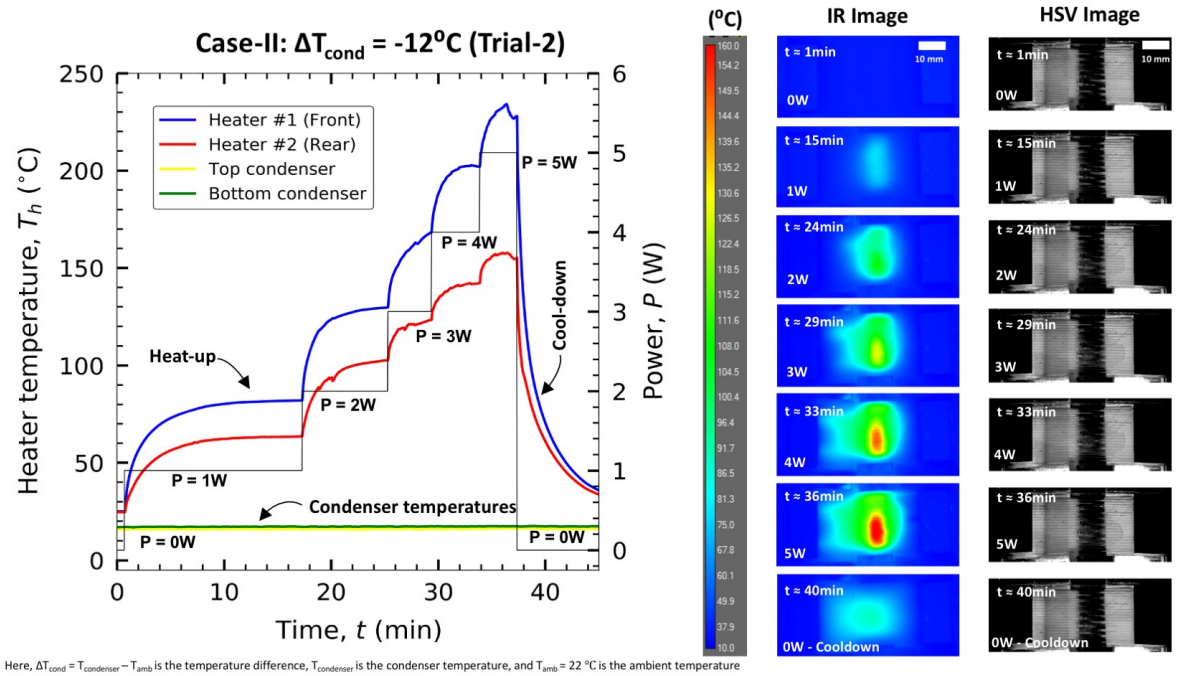

Figure D.13: Reproducing effort for 3D-stack PHP (double-layer) for relative condenser temperature of -12K (trial-2) along with IR and HSV snapshots.

APPENDIX E: COPYRIGHT PERMISSIONS

American Physical Society
Reuse and Permissions License

17-Sep-2021

This license agreement between the American Physical Society ("APS") and Khan Mohammad Rabbi ("You") consists of your license details and the terms and conditions provided by the American Physical Society and SciPris.

Licensed Content Information

License Number:	**RNP/21/SEP/044625**
License date:	17-Sep-2021
DOI:	10.1103/PhysRevFluids.5.094003
Title:	Understanding pulsed jet impingement cooling by instantaneous heat flux matching at solid-liquid interfaces
Author:	Khan Md. Rabbi, Jake Carter, and Shawn A. Putnam
Publication:	Physical Review Fluids
Publisher:	American Physical Society
Cost:	USD $ 0.00

Request Details

Does your reuse require significant modifications: No

Specify intended distribution locations:	United States
Reuse Category:	Reuse in a thesis/dissertation
Requestor Type:	Author of requested content
Items for Reuse:	Whole Article
Format for Reuse:	Electronic

Information about New Publication:

University/Publisher:	University of Central Florida
Title of dissertation/thesis:	A Novel Flexible Cooling System for Future Generation Electronic Devices
Author(s):	Khan Mohammad Rabbi
Expected completion date:	Dec. 2021

License Requestor Information

Name:	Khan Mohammad Rabbi
Affiliation:	Individual
Email Id:	khan.rabbi@knights.ucf.edu
Country:	United States

Figure E.1: The copyright permission for journal Physical Review Fluids (PRFluids) published by American Physical Society (APS).

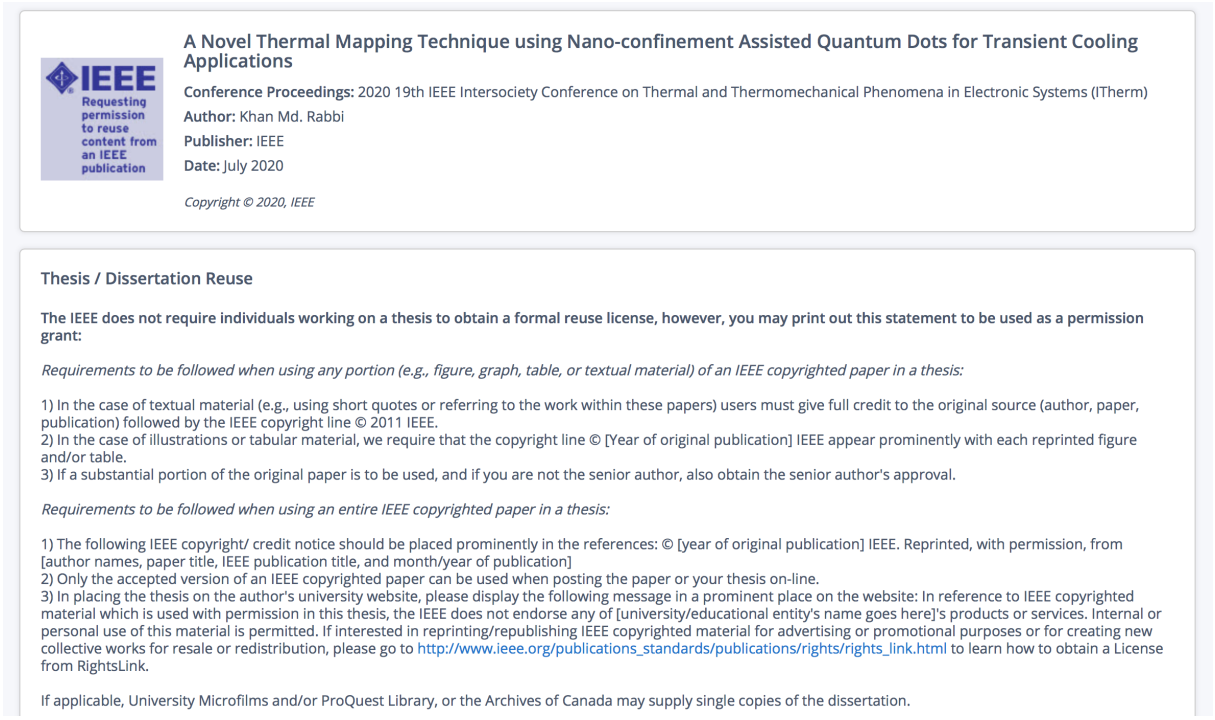

A Novel Thermal Mapping Technique using Nano-confinement Assisted Quantum Dots for Transient Cooling Applications

Conference Proceedings: 2020 19th IEEE Intersociety Conference on Thermal and Thermomechanical Phenomena in Electronic Systems (ITherm)

Author: Khan Md. Rabbi

Publisher: IEEE

Date: July 2020

Figure E.2: The copyright permission for IEEE ITherm Conference 2020

Submission of Final Extended Abstract (Due August 31, 2019)

Revise the Extended Abstract by taking into account the comments from reviewers, if any, and submit the final version of Extended Abstract for inclusion in the proceedings.

All contributors must upload the Final Extended Abstract for inclusion in the proceedings, even if there is no modification from the initial Extended Abstract.

The final version of the extended abstract that does not conform to the correct format will not be included in the proceedings. There will be no opportunity to alter it after the submission of the final version.

Note: The PRTEC2019 will provide a book of extended abstracts in an electronic form (distributed to registrants via the website) only. Authors of the extended abstracts are not required to transfer copyright for their articles to PRTEC2019. Therefore, the authors can submit the contents of their own extended abstract to an appropriate journal with self-responsibility.

Important: Each accepted extended abstract must have at least one paid regular or student registration before August 31, 2019 to ensure that their presentation is included in the conference program and the book of extended abstract.

Figure E.3: The copyright permission for Pacific Rim Thermal Engineering Conference (PRTEC) 2019

LIST OF REFERENCES

[1] Thomas Germain, Chance Brewer, James Scott, and Shawn A Putnam. Scalable stamp printing and fabrication of hemiwicking surfaces. *JoVE (Journal of Visualized Experiments)*, (142):e58546, 2018.

[2] Shawn A Putnam. Thermal probes of nanoparticle interfaces: Thermodiffusion and thermal conductivity of nanoparticle suspensions. *Thesis (Ph.D.)*, 2007.

[3] ID Mash and GP Motulevich. Optical constants and electronic characteristics of titanium. *Soviet Physics JETP*, 36(3), 1973.

[4] Khan Md Rabbi, Jake Carter, and Shawn A Putnam. Understanding pulsed jet impingement cooling by instantaneous heat flux matching at solid-liquid interfaces. *Physical Review Fluids*, 5(9):094003, 2020.

[5] MA Ebadian and CX Lin. A review of high-heat-flux heat removal technologies. *Journal of Heat Transfer*, 133(11):110801, 2011.

[6] Satish G Kandlikar and Akhilesh V Bapat. Evaluation of jet impingement, spray and microchannel chip cooling options for high heat flux removal. *Heat Transfer Engineering*, 28(11):911–923, 2007.

[7] Jungho Kim. Spray cooling heat transfer: the state of the art. *International Journal of Heat and Fluid Flow*, 28(4):753–767, 2007.

[8] Jungho Kim. Review of nucleate pool boiling bubble heat transfer mechanisms. *International Journal of Multiphase Flow*, 35(12):1067–1076, 2009.

[9] Poh-Seng Lee and Suresh V Garimella. Saturated flow boiling heat transfer and pressure drop in silicon microchannel arrays. *International Journal of Heat and Mass Transfer*, 51(3-4):789–806, 2008.

[10] K. Jambunathan, E. Lai, M. A. Moss, and B. L. Button. A review of heat transfer data for single circular jet impingement. *International Journal of Heat and Fluid Flow*, 13(2):106–115, 1992.

[11] D. H. Wolf, F. P. Incropera, and R. Viskanta. Jet impingement boiling. *Advances in Heat Transfer*, 23:1–132, 1993.

[12] RG Nevins and HD Ball. Heat transfer between a flat plate and a pulsating impinging jet. In *Proceedings of the National Heat Transfer Conference*, volume 60, pages 510–516, 1961.

[13] H. M. Hofmann, D. L. Movileanu, M. Kind, and H. Martin. Influence of a pulsation on heat transfer and flow structure in submerged impinging jets. *International Journal of Heat and Mass Transfer*, 50:3638–3648, 2007.

[14] Mangesh Chaudhari, Bhalchandra Puranik, and Amit Agrawal. Heat transfer characteristics of synthetic jet impingement cooling. *International Journal of Heat and Mass Transfer*, 53(5-6):1057–1069, 2010.

[15] Y. W. Lyu, J. Z. Zhang, X. C. Liu, and Y. Shan. Experimental investigation of impinging heat transfer of the pulsed chevron jet on a semicylindrical concave plate. *Journal of Heat Transfer*, 141(3):032201, 2019.

[16] M. R. Zargarabadi, E. Rezaei, and B. Yousefi-Lafouraki. Numerical analysis of turbulent flow and heat transfer of sinusoidal pulsed jet impinging on an asymmetrical concave surface. *Applied Thermal Engineering*, 128:578–585, 2018.

[17] Sina Ghadi, Kazem Esmailpour, SM Hosseinalipour, and Arun Mujumdar. Experimental study of formation and development of coherent vortical structures in pulsed turbulent impinging jet. *Experimental Thermal and Fluid Science*, 74:382–389, 2016.

[18] CM Hsu, WC Jhan, and YY Chang. Flow and heat transfer characteristics of a pulsed jet impinging on a flat plate. *Heat and Mass Transfer*, pages 1–18, 2019.

[19] Mehran Rajabi Zargarabadi, Ehsan Rezaei, and Babak Yousefi-Lafouraki. Numerical analysis of turbulent flow and heat transfer of sinusoidal pulsed jet impinging on an asymmetrical concave surface. *Applied Thermal Engineering*, 128:578–585, 2018.

[20] Chan Tang, Jing-Zhou Zhang, Yuan-Wei Lyu, and Xiao-Ming Tan. Convective heat transfer on a flat target surface impinged by pulsating jet with an additional transmission chamber. *Heat and Mass Transfer*, pages 1–23, 2019.

[21] Kazem Esmailpour, Behnam Bozorgmehr, Seyed Mostafa Hosseinalipour, and Arun S Mujumdar. Entropy generation and second law analysis of pulsed impinging jet. *International Journal of Numerical Methods for Heat & Fluid Flow*, 25(5):1089–1106, 2015.

[22] Harekrishna Yadav, Amit Agrawal, and Atul Srivastava. Mixing and entrainment characteristics of a pulse jet. *International Journal of Heat and Fluid Flow*, 61:749–761, 2016.

[23] Z Trávníček and T Vít. Impingement heat/mass transfer to hybrid synthetic jets and other reversible pulsating jets. *International Journal of Heat and Mass Transfer*, 85:473–487, 2015.

[24] Yanyao Zhang, Ping Li, and Yonghui Xie. Numerical investigation of heat transfer characteristics of impinging synthetic jets with different waveforms. *International Journal of Heat and Mass Transfer*, 125:1017–1027, 2018.

[25] Xi Xia and Kamran Mohseni. Transitional region of a round synthetic jet. *Physical Review Fluids*, 3(1):011901, 2018.

[26] Sina Ghadi, Kazem Esmailpour, Mostafa Hosseinalipour, and Mehrdad Kalantar. Dynamical study of pulsed impinging jet with time varying heat flux boundary condition. *Heat Transfer—Asian Research*, 45(1):85–100, 2016.

[27] H. Bostanci, B. He, and L. C. Chow. Spray cooling with ammonium hydroxide. *International Journal of Heat and Mass Transfer*, 107:45–52, 2017.

[28] Navdeep Singh Dhillon, Jacopo Buongiorno, and Kripa K Varanasi. Critical heat flux maxima during boiling crisis on textured surfaces. *Nature Communications*, 6:8247, 2015.

[29] AN Pavlenko, AM Matsekh, NI Pecherkin, R Kneer, VV Lel, and AS Surtaev. Heat transfer and crisis phenomena with intense boiling in the falling wave liquid films. *Thermophysics and Aeromechanics*, 13(1):85–96, 2006.

[30] W. Meng. *A Study on Characteristics of a Thin Liquid Film Flowing down a Uniformly Heated Plate with Constant Heat Flux*. KTH, School of Science, 2018.

[31] Dionysios Skamnakis and Kyriakos Papailiou. Flow stability analysis and excitation using pulsating jets. *Comptes Rendus Mecanique*, 333(8):628–635, 2005.

[32] Harekrishna Yadav and Amit Agrawal. Effect of pulsation on the near flow field of a submerged water jet. *Sādhanā*, 43(3):44, 2018.

[33] Valery L Okulov, Igor V Naumov, Robert F Mikkelsen, Ivan K Kabardin, and Jens N Sørensen. A regular strouhal number for large-scale instability in the far wake of a rotor. *Journal of Fluid Mechanics*, 747:369–380, 2014.

[34] SJ Leib and ME Goldstein. Convective and absolute instability of a viscous liquid jet. *The Physics of fluids*, 29(4):952–954, 1986.

[35] V Struhal. Uebereinebesondere art der tonerregung (on an unusual sort of sound excitation). *Annalen der Physik und Chemie*, 3:216–251, 1878.

[36] G. Lavalle, Y. Li, S. Mergui, N. Grenier, and G. F. Dietze. Suppression of the kapitza instability in confined falling liquid films. *Journal of Fluid Mechanics*, 860:608–639, 2019.

[37] G. F. Dietze. On the kapitza instability and the generation of capillary waves. *Journal of Fluid Mechanics*, 789:368–401, 2016.

[38] D. V. E. Zaitsev, O. A. Kabov, V. V. Cheverda, and N. S. Bufetov. The effect of wave formation and wetting angle on the thermocapillary breakdown of a falling liquid film. *High Temperature*, 42(3):450–456, 2004.

[39] G.F. Dietze. On the kapitza instability and the generation of capillary waves. *Journal of Fluid Mechanics*, 789:368–401, 2016.

[40] Lord (John William Strutt) Rayleigh. *Investigation of the character of the equilibrium of an incompressible heavy fluid of variable density*. Proceedings of the London Mathematical Society, 1883.

[41] V. Lel, H. Stadler, A. Pavlenko, and R. Kneer. Evolution of metastable quasi-regular structures in heated wavy liquid films. *Heat and Mass transfer*, 43(11):1121–1132, 2007.

[42] Walter Ambrosini, Nicola Forgione, and Francesco Oriolo. Statistical characteristics of a water film falling down a flat plate at different inclinations and temperatures. *International Journal of Multiphase Flow*, 28(9):1521–1540, 2002.

[43] Mehrdad Mehrvand and Shawn A Putnam. Transient and local two-phase heat transport at macro-scales to nano-scales. *Communications Physics*, 1(1):21, 2018.

[44] E R G Eckert and Robert M Jr. Drake. *Analysis of Heat and Mass Transfer*. McGraw-Hill Inc., New York, 1972.

[45] Xin Liu, L A Gabour, and J H Lienhard V. Stagnation-point heat transfer during impingement of laminar liquid jets: Analysis including surface tension. *ASME Journal of Heat Transfer*, 115:99–105, 1993.

[46] Adrian Bejan. *Convection Heat Transfer*. John Wiley and Sons, Inc., Hoboken NJ, 4 edition, 2013.

[47] Khan Md Rabbi, Christopher Borden, and Shawn A Putnam. A novel thermal mapping technique using nano-confinement assisted quantum dots for transient cooling applications. In *2020 19th IEEE Intersociety Conference on Thermal and Thermomechanical Phenomena in Electronic Systems (ITherm)*, pages 926–931. IEEE, 2020.

[48] Khan Md Rabbi, Jake Carter, Juan Sanchez, and Shawn A Putnam. Laser-scanning fluorescence thermography for thermofluid heat transfer. In *2nd Pacific Rim Thermal Engineering Conference*, 2019.

[49] Andrew Richenderfer, Artyom Kossolapov, Jee Hyun Seong, Giacomo Saccone, Etienne Demarly, Ravikishore Kommajosyula, Emilio Baglietto, Jacopo Buongiorno, and Matteo Bucci. Investigation of subcooled flow boiling and chf using high-resolution diagnostics. *Experimental Thermal and Fluid Science*, 99:35–58, 2018.

[50] Mehrdad Mehrvand and Shawn A Putnam. Transient and local two-phase heat transport at macro-scales to nano-scales. *Communications Physics*, 1(1):1–13, 2018.

[51] Emanuel Peinke, Tobias Sattler, Guilherme Monteiro Torelly, Joël Bleuse, Julien Claudon, Willem L Vos, and Jean-Michel Gérard. Generation of ultrashort (˜ 10ps) spontaneous emission pulses by quantum dots in a switched optical microcavity. *arXiv preprint arXiv:1910.10518*, 2019.

[52] Laura M Maestro, Carlos Jacinto, Ueslen R Silva, Fiorenzo Vetrone, John A Capobianco, Daniel Jaque, and José García Solé. Cdte quantum dots as nanothermometers: towards highly sensitive thermal imaging. *Small*, 7(13):1774–1778, 2011.

[53] Laura Martinez Maestro, Emma Martín Rodríguez, Francisco Sanz Rodríguez, MC Iglesias-de la Cruz, Angeles Juarranz, Rafik Naccache, Fiorenzo Vetrone, Daniel Jaque, John A Capobianco, and José García Solé. Cdse quantum dots for two-photon fluorescence thermal imaging. *Nano letters*, 10(12):5109–5115, 2010.

[54] Sha Li, Kai Zhang, Jui-Ming Yang, Liwei Lin, and Haw Yang. Single quantum dots as local temperature markers. *Nano Letters*, 7(10):3102–3105, 2007.

[55] P Haro-González, L Martínez-Maestro, IR Martín, J García-Solé, and D Jaque. High-sensitivity fluorescence lifetime thermal sensing based on cdte quantum dots. *Small*, 8(17):2652–2658, 2012.

[56] Sean Keuleyan, Emmanuel Lhuillier, Vuk Brajuskovic, and Philippe Guyot-Sionnest. Mid-infrared hgte colloidal quantum dot photodetectors. *Nature Photonics*, 5(8):489, 2011.

[57] CF Chapman, Y Liu, GJ Sonek, and BJ Tromberg. The use of exogenous fluorescent probes for temperature measurements in single living cells. *Photochemistry and Photobiology*, 62(3):416–425, 1995.

[58] David J Norris. Multispectral quantum-dot photodetectors. *Nature Photonics*, 13(4):230, 2019.

[59] Jun Yang, Zheng Ling, Ben Q Li, Rongheng Li, and Xuesong Mei. Nanoscale 3d temperature gradient measurement based on fluorescence spectral characteristics of the cdte quantum dot probe. *Optics Express*, 27(5):6770–6791, 2019.

[60] Yatendra Pal Varshni. Temperature dependence of the energy gap in semiconductors. *Physica*, 34(1):149–154, 1967.

[61] Jungchul Kim, Myoung-Woon Moon, and Ho-Young Kim. Dynamics of hemiwicking. *Journal of Fluid Mechanics*, 800:57–71, 2016.

[62] Beom Seok Kim, Geehong Choi, Dong Il Shim, Kyung Min Kim, and Hyung Hee Cho. Surface roughening for hemi-wicking and its impact on convective boiling heat transfer. *International Journal of Heat and Mass Transfer*, 102:1100–1107, 2016.

[63] J. Buongiorno, DC. Venerus, N. Prabhat, T. McKrell, J. Townsend, R. Christianson, YV. Tolmachev, et al. A benchmark study on the thermal conductivity of nanofluids. *Journal of Applied Physics*, 106(9):p.094312, 2009.

[64] S Zeinali Heris, S Gh Etemad, and M Nasr Esfahany. Experimental investigation of oxide nanofluids laminar flow convective heat transfer. *International Communications in Heat and Mass Transfer*, 33(4):529–535, 2006.

[65] SM Fotukian and M Nasr Esfahany. Experimental study of turbulent convective heat transfer and pressure drop of dilute cuo/water nanofluid inside a circular tube. *International Communications in Heat and Mass Transfer*, 37(2):214–219, 2010.

[66] AA Abbasian Arani and J Amani. Experimental investigation of diameter effect on heat transfer performance and pressure drop of tio2–water nanofluid. *Experimental Thermal and Fluid Science*, 44:520–533, 2013.

[67] Pawel Keblinski, Jeffrey A Eastman, and David G Cahill. Nanofluids for thermal transport. *Materials today*, 8(6):36–44, 2005.

[68] Xiang-Qi Wang and Arun S Mujumdar. Heat transfer characteristics of nanofluids: a review. *International Journal of Thermal Sciences*, 46(1):1–19, 2007.

[69] Sezer Özerinç, Sadık Kakaç, and Almıla Güvenç Yazıcıoğlu. Enhanced thermal conductivity of nanofluids: a state-of-the-art review. *Microfluidics and Nanofluidics*, 8(2):145–170, 2010.

[70] La rus Godson, B Raja, D Mohan Lal, and S Wongwises. Enhancement of heat transfer using nanofluids—an overview. *Renewable and Sustainable Energy Reviews*, 14(2):629–641, 2010.

[71] Jing Fan and Liqiu Wang. Review of heat conduction in nanofluids. *Journal of Heat Transfer*, 133(4):040801, 2011.

[72] Pawel Keblinski, Ravi Prasher, and Jacob Eapen. Thermal conductance of nanofluids: is the controversy over? *Journal of Nanoparticle research*, 10(7):1089–1097, 2008.

[73] Yanhong Wang and Jingzhi Wu. Radiative heat transfer between nanoparticles enhanced by intermediate particle. *AIP Advances*, 6(2):025104, 2016.

[74] Gilberto Domingues, Sebastian Volz, Karl Joulain, and Jean-Jacques Greffet. Heat transfer between two nanoparticles through near field interaction. *Physical Review Letters*, 94(8):085901, 2005.

[75] Sebastian Volz and Gilberto Domingues. Near-field heat transfer percolation in nanoparticles based composite media. *arXiv preprint arXiv:0806.1619*, 2008.

[76] William Evans, Jacob Fish, and Pawel Keblinski. Role of brownian motion hydrodynamics on nanofluid thermal conductivity. *Applied Physics Letters*, 88(9):093116, 2006.

[77] Seok Pil Jang and Stephen US Choi. Role of brownian motion in the enhanced thermal conductivity of nanofluids. *Applied Physics Letters*, 84(21):4316–4318, 2004.

[78] Sanjeeva Witharana, Chris Hodges, Dan Xu, Xiaojun Lai, and Yulong Ding. Aggregation and settling in aqueous polydisperse alumina nanoparticle suspensions. *Journal of Nanoparticle Research*, 14(5):851, 2012.

[79] Ravi Prasher, William Evans, Paul Meakin, Jacob Fish, Patrick Phelan, and Pawel Keblinski. Effect of aggregation on thermal conduction in colloidal nanofluids. *Applied Physics Letters*, 89(14):143119, 2006.

[80] W Yu and SUS Choi. The role of interfacial layers in the enhanced thermal conductivity of nanofluids: a renovated hamilton–crosser model. *Journal of Nanoparticle Research*, 6(4):355–361, 2004.

[81] C-J Yu, AG Richter, A Datta, MK Durbin, and Pulak Dutta. Molecular layering in a liquid on a solid substrate: an x-ray reflectivity study. *Physica B: Condensed Matter*, 283(1-3):27–31, 2000.

[82] James Clerk Maxwell. A treatise on electricity and magnetism. In *A Treatise on Electricity and Magnetism*. Clarendon, Oxford, 1892.

[83] Shawn A Putnam, David G Cahill, Benjamin J Ash, and Linda S Schadler. High-precision thermal conductivity measurements as a probe of polymer/nanoparticle interfaces. *Journal of Applied Physics*, 94(10):6785–6788, 2003.

[84] S Kakac, RK Shah, and W Aung. *Handbook of single-phase convective heat transfer*. John Wiley and Sons Inc., 1987.

[85] MN Özişik. *Radiative transfer and interactions with conduction and convection*. John Wiley and Sons Inc., 1973.

[86] DRVSRK Sastry, ASN Murti, and T Poorna Kantha. The effect of heat transfer on mhd marangoni boundary layer flow past a flat plate in nanofluid. *International Journal of Engineering Mathematics*, 2013, 2013.

[87] Kevin Apmann, Ryan Fulmer, Alberto Soto, and Saeid Vafaei. Thermal conductivity and viscosity: Review and optimization of effects of nanoparticles. *Materials*, 14(5):1291, 2021.

[88] Bernardo Buonomo, Laura Colla, Laura Fedele, Oronzio Manca, and Lorenzo Marinelli. A comparison of nanofluid thermal conductivity measurements by flash and hot disk techniques. In *Journal of Physics: Conference Series*, volume 547, page 012046. IOP Publishing, 2014.

[89] Asirinaidu Dunga, Ramji Koona, and SV Naidu. Experimental investigation of thermal conductivity of alumina (al2o3)-multi-walled carbon nanotubes (mwcnt) in water-ethylene glycol hybrid nanofluid. *Journal of Nanofluids*, 11(1):58–73, 2022.

[90] Ravi Prasher, Patrick E Phelan, and Prajesh Bhattacharya. Effect of aggregation kinetics on the thermal conductivity of nanoscale colloidal solutions (nanofluid). *Nano Letters*, 6(7):1529–1534, 2006.

[91] Jonggan Hong and Dongsik Kim. Effects of aggregation on the thermal conductivity of alumina/water nanofluids. *Thermochimica Acta*, 542:28–32, 2012.

[92] Niels H Juul. Diffuse radiation configuration view factors between two spheres, and their limits. *Letters in Heat and Mass Transfer*, 3(3):205–211, 1976.

[93] Matthew J Kelly, Douglas E Wolfe, Jogender Singh, Jeff Eldridge, Dong-Ming Zhu, and Robert Miller. Thermal barrier coatings design with increased reflectivity and lower thermal conductivity for high-temperature turbine applications. *International Journal of Applied Ceramic Technology*, 3(2):81–93, 2006.

[94] SMS Murshed, KC Leong, and C Yang. Investigations of thermal conductivity and viscosity of nanofluids. *International Journal of Thermal Sciences*, 47(5):560–568, 2008.

[95] Thakleaw Yiamsawasd, Ahmet Selim Dalkilic, and Somchai Wongwises. Measurement of the thermal conductivity of titania and alumina nanofluids. *Thermochimica Acta*, 545:48–56, 2012.

[96] Bock Choon Pak and Young I Cho. Hydrodynamic and heat transfer study of dispersed fluids with submicron metallic oxide particles. *Experimental Heat Transfer an International Journal*, 11(2):151–170, 1998.

[97] Elena V Timofeeva, Alexei N Gavrilov, James M McCloskey, Yuriy V Tolmachev, Samuel Sprunt, Lena M Lopatina, and Jonathan V Selinger. Thermal conductivity and particle agglomeration in alumina nanofluids: experiment and theory. *Physical Review E*, 76(6):061203, 2007.

[98] D Kwek, A Crivoi, and Fei Duan. Effects of temperature and particle size on the thermal property measurements of al2o3- water nanofluids. *Journal of Chemical & Engineering Data*, 55(12):5690–5695, 2010.

[99] Mohammad Hemmat Esfe, Seyfolah Saedodin, Omid Mahian, and Somchai Wongwises. Thermal conductivity of al2o3/water nanofluids. *Journal of Thermal Analysis and Calorimetry*, 117(2):675–681, 2014.

[100] Benigno Barbés, Ricardo Páramo, Eduardo Blanco, María José Pastoriza-Gallego, Manuel M Pineiro, José Luis Legido, and Carlos Casanova. Thermal conductivity and specific heat capacity measurements of al 2 o 3 nanofluids. *Journal of Thermal Analysis and Calorimetry*, 111(2):1615–1625, 2013.

[101] Jeffrey A Eastman, SUS Choi, Sheng Li, W Yu, and LJ Thompson. Anomalously increased effective thermal conductivities of ethylene glycol-based nanofluids containing copper nanoparticles. *Applied Physics Letters*, 78(6):718–720, 2001.

[102] Honorine Angue Mintsa, Gilles Roy, Cong Tam Nguyen, and Dominique Doucet. New temperature dependent thermal conductivity data for water-based nanofluids. *International Journal of Thermal Sciences*, 48(2):363–371, 2009.

[103] Sarit K Das, Nandy Putra, and Wilfried Roetzel. Pool boiling of nano-fluids on horizontal narrow tubes. *International Journal of Multiphase Flow*, 29(8):1237–1247, 2003.

[104] Hrishikesh E Patel, T Sundararajan, and Sarit K Das. An experimental investigation into the thermal conductivity enhancement in oxide and metallic nanofluids. *Journal of Nanoparticle Research*, 12(3):1015–1031, 2010.

[105] Hidetoshi Masuda, Akira Ebata, and Kazumari Teramae. Alteration of thermal conductivity and viscosity of liquid by dispersing ultra-fine particles. dispersion of al2o3, sio2 and tio2 ultra-fine particles. *Netsu Bussei*, 1993.

[106] Morteza Ghanbarpour, E Bitaraf Haghigi, and Rahmatollah Khodabandeh. Thermal properties and rheological behavior of water based al2o3 nanofluid as a heat transfer fluid. *Experimental Thermal and Fluid Science*, 53:227–235, 2014.

[107] Dae-Hwang Yoo, KS Hong, TE Hong, JA Eastman, and Ho-Soon Yang. Thermal conductivity of al2o3/water nanofluids. *Journal of the Korean Physical Society*, 51(12):S84–S87, 2007.

[108] S Lee, SUS Choi, S Li, and JA Eastman. Measuring thermal conductivity of fluids containing oxide nanoparticles. *Journal of Heat transfer*, 121(2):280–289, 1999.

[109] Sarit Kumar Das, Nandy Putra, Peter Thiesen, and Wilfried Roetzel. Temperature dependence of thermal conductivity enhancement for nanofluids. *Journal of Heat Transfer*, 125(4):567–574, 2003.

[110] MI Pryazhnikov, AV Minakov, V Ya Rudyak, and DV Guzei. Thermal conductivity measurements of nanofluids. *International Journal of Heat and Mass Transfer*, 104:1275–1282, 2017.

[111] MM Heyhat, F Kowsary, AM Rashidi, MH Momenpour, and A Amrollahi. Experimental investigation of laminar convective heat transfer and pressure drop of water-based al2o3 nanofluids in fully developed flow regime. *Experimental Thermal and Fluid Science*, 44:483–489, 2013.

[112] Dongsheng Wen and Yulong Ding. Experimental investigation into convective heat transfer of nanofluids at the entrance region under laminar flow conditions. *International Journal of Heat and Mass Transfer*, 47(24):5181–5188, 2004.

[113] S Krishnamurthy, Phelan Bhattacharya, PE Phelan, and RS Prasher. Enhanced mass transport in nanofluids. *Nano Letters*, 6(3):419–423, 2006.

[114] Huaqing Xie, Jinchang Wang, Tonggeng Xi, Yan Liu, Fei Ai, and Qingren Wu. Thermal conductivity enhancement of suspensions containing nanosized alumina particles. *Journal of Applied Physics*, 91(7):4568–4572, 2002.

[115] Calvin H Li and GP Peterson. Experimental investigation of temperature and volume fraction variations on the effective thermal conductivity of nanoparticle suspensions (nanofluids). *Journal of Applied Physics*, 99(8):084314, 2006.

[116] Dong-Wook Oh, Ankur Jain, John K Eaton, Kenneth E Goodson, and Joon Sik Lee. Thermal conductivity measurement and sedimentation detection of aluminum oxide nanofluids by

using the 3ω method. *International Journal of Heat and Fluid Flow*, 29(5):1456–1461, 2008.

[117] Dae-Hwang Yoo, KS Hong, and Ho-Soon Yang. Study of thermal conductivity of nanofluids for the application of heat transfer fluids. *Thermochimica Acta*, 455(1-2):66–69, 2007.

[118] KB Anoop, T Sundararajan, and Sarit K Das. Effect of particle size on the convective heat transfer in nanofluid in the developing region. *International Journal of Heat and Mass Transfer*, 52(9-10):2189–2195, 2009.

[119] M Chandrasekar, S Suresh, and A Chandra Bose. Experimental investigations and theoretical determination of thermal conductivity and viscosity of al2o3/water nanofluid. *Experimental Thermal and Fluid Science*, 34(2):210–216, 2010.

[120] MA Serebryakova, SV Dimov, SP Bardakhanov, and SA Novopashin. Thermal conductivity, viscosity and rheology of a suspension based on al2o3 nanoparticles and mixture of 90% ethylene glycol and 10% water. *International Journal of Heat and Mass Transfer*, 83:187–191, 2015.

[121] Michael P Beck, Yanhui Yuan, Pramod Warrier, and Amyn S Teja. The effect of particle size on the thermal conductivity of alumina nanofluids. *Journal of Nanoparticle research*, 11(5):1129–1136, 2009.

[122] Wesley Williams, Jacopo Buongiorno, and Lin-Wen Hu. Experimental investigation of turbulent convective heat transfer and pressure loss of alumina/water and zirconia/water nanoparticle colloids (nanofluids) in horizontal tubes. *Journal of Heat Transfer*, 130(4), 2008.

[123] Ravi Agarwal, Kamalesh Verma, Narendra Kumar Agrawal, and Ramvir Singh. Sensitivity of thermal conductivity for al2o3 nanofluids. *Experimental Thermal and Fluid Science*, 80:19–26, 2017.

[124] Georgia J Tertsinidou, Chrysi M Tsolakidou, Maria Pantzali, Marc J Assael, Laura Colla, Laura Fedele, Sergio Bobbo, and William A Wakeham. New measurements of the apparent thermal conductivity of nanofluids and investigation of their heat transfer capabilities. *Journal of Chemical & Engineering Data*, 62(1):491–507, 2017.

[125] Seokwon Kim, Chongyoup Kim, Wook-Hyun Lee, and Seong-Ryong Park. Rheological properties of alumina nanofluids and their implication to the heat transfer enhancement mechanism. *Journal of Applied Physics*, 110(3):034316, 2011.

[126] Kau-Fui Wong and Tarun Bhshkar. Transport properties of alumina nanofluids. In *ASME International Mechanical Engineering Congress and Exposition*, volume 47640, pages 251–260, 2006.

[127] Adi T Utomo, Heiko Poth, Phillip T Robbins, and Andrzej W Pacek. Experimental and theoretical studies of thermal conductivity, viscosity and heat transfer coefficient of titania and alumina nanofluids. *International Journal of Heat and Mass Transfer*, 55(25-26):7772–7781, 2012.

[128] Calvin H Li and GP Peterson. The effect of particle size on the effective thermal conductivity of al 2 o 3-water nanofluids. *Journal of Applied Physics*, 101(4):044312, 2007.

[129] Omer A Alawi, Nor Azwadi Che Sidik, Hong Wei Xian, Tung Hao Kean, and Salim Newaz Kazi. Thermal conductivity and viscosity models of metallic oxides nanofluids. *International Journal of Heat and Mass Transfer*, 116:1314–1325, 2018.

[130] I Tavman and A Turgut. An investigation on thermal conductivity and viscosity of water based nanofluids. In *Microfluidics Based Microsystems*, pages 139–162. Springer, 2010.

[131] Zid Said, Mohammad H Sajid, Mohammad A Alim, Rahman Saidur, and Nasrudin A Rahim. Experimental investigation of the thermophysical properties of al2o3-nanofluid and its effect on a flat plate solar collector. *International Communications in Heat and Mass Transfer*, 48:99–107, 2013.

[132] WH Azmi, KV Sharma, Rizalman Mamat, ABS Alias, and Izan Izwan Misnon. Correlations for thermal conductivity and viscosity of water based nanofluids. In *IOP Conference Series: Materials Science and Engineering*, volume 36, page 012029. IOP Publishing, 2012.

[133] Georgiana Madalina Moldoveanu, Gabriela Huminic, Alina Adriana Minea, and Angel Huminic. Experimental study on thermal conductivity of stabilized al2o3 and sio2 nanofluids and their hybrid. *International Journal of Heat and Mass Transfer*, 127:450–457, 2018.

[134] Sidi El Becaye Maiga, Samy Joseph Palm, Cong Tam Nguyen, Gilles Roy, and Nicolas Galanis. Heat transfer enhancement by using nanofluids in forced convection flows. *International Journal of Heat and Fluid Flow*, 26(4):530–546, 2005.

[135] G Paul, M Chopkar, I Manna, and PK Das. Techniques for measuring the thermal conductivity of nanofluids: a review. *Renewable and Sustainable Energy Reviews*, 14(7):1913–1924, 2010.

[136] Y Ding, H Chen, L Wang, CY Yang, Y Hel, W Yang, WP Lee, L Zhang, and R Huo. Heat transfer intensification using nanofluids, kona powder part. *KONA Powder and Particle*, 25:23–28, 2007.

[137] DPH Hasselman. Can the temperature dependence of the heat transfer coefficient of the wire–nanofluid interface explain the "anomalous" thermal conductivity of nanofluids measured by the hot-wire method? *International Journal of Thermophysics*, 39(9):109, 2018.

[138] Marc J Assael and William A Wakeham. Comments on "can the temperature dependence of the heat transfer coefficient of the wire–nanofluid interface explain the "anomalous" thermal conductivity of nanofluids measured by the hot-wire method?". *International Journal of Thermophysics*, 40(6):59, 2019.

[139] DPH Hasselman. Response to comments by mj assael and wa wakeham on: Dph hasselman,"can the temperature dependence of the heat transfer coefficient of the wire–nanofluid interface explain the 'anomalous' thermal conductivity of nanofluids measured by the hot-wire method?". *International Journal of Thermophysics*, 40(6):60, 2019.

[140] MG Sobamowo. Combined effects of thermal radiation and nanoparticles on free convection flow and heat transfer of casson fluid over a vertical plate. *International Journal of Chemical Engineering*, 2018, 2018.

[141] Richard J Murdock, Shawn A Putnam, Soumen Das, Ankur Gupta, Elyse DZ Chase, and Sudipta Seal. High-throughput, protein-targeted biomolecular detection using frequency-domain faraday rotation spectroscopy. *Small*, 13(12):1602862, 2017.

[142] Thomas J Rieger. On the emissivity of alumina/aluminum composite particles. *Journal of Spacecraft and Rockets*, 16(6):438–439, 1979.

[143] Kaihua Zhang, Kun Yu, Yufang Liu, and Yuejin Zhao. An improved algorithm for spectral emissivity measurements at low temperatures based on the multi-temperature calibration method. *International Journal of Heat and Mass Transfer*, 114:1037–1044, 2017.

[144] John Mathew and Shankar Krishnan. A review on transient thermal management of electronic devices. *Journal of Electronic Packaging*, 2021.

[145] John S Glaser, Assaad Helou, Muskan Sharma, Robert Strittmatter, and Michael de Rooij. Simple high-performance thermal management of chip-scale gan fets. In *2021 IEEE Applied Power Electronics Conference and Exposition (APEC)*, pages 44–49. IEEE, 2021.

[146] Gilberto Moreno, Sreekant Narumanchi, Xuhui Feng, Paul Anschel, Steve Myers, and Phil Keller. Electric-drive vehicle power electronics thermal management: Current status, challenges, and future directions. *Journal of Electronic Packaging*, 2021.

[147] H Akachi. Structure of a heat pipe. *USA Patent*, 4921041, 1996.

[148] Daniele Mangini, Mauro Mameli, Anastasios Georgoulas, Luciano Araneo, Sauro Filippeschi, and Marco Marengo. A pulsating heat pipe for space applications: Ground and microgravity experiments. *International Journal of Thermal Sciences*, 95:53–63, 2015.

[149] Anselmo Cecere, Davide De Cristofaro, Raffaele Savino, Vincent Ayel, Thibaud Sole-Agostinelli, Marco Marengo, Cyril Romestant, and Yves Bertin. Experimental analysis of a flat plate pulsating heat pipe with self-rewetting fluids during a parabolic flight campaign. *Acta Astronautica*, 147:454–461, 2018.

[150] Luca Pagliarini, Luca Cattani, Fabio Bozzoli, Mauro Mameli, Sauro Filippeschi, Sara Rainieri, and Marco Marengo. Thermal characterization of a multi-turn pulsating heat pipe in microgravity conditions: Statistical approach to the local wall-to-fluid heat flux. *International Journal of Heat and Mass Transfer*, 169:120930, 2021.

[151] Rafael Beicker Barbosa de Oliveira, Sergio Gradella Villalva, Luiz Paulo Rodrigues Filho, Fernando Luiz Windlin, Guilherme Henrique Mayer Alegre, and Rogério Gonçalves do San-

tos. Pulsating heat pipe automotive application. Technical report, SAE Technical Paper, 2020.

[152] Ri-Guang Chi, Won-Sik Chung, and Seok-Ho Rhi. Thermal characteristics of an oscillating heat pipe cooling system for electric vehicle li-ion batteries. *Energies*, 11(3):655, 2018.

[153] Marco Bernagozzi, Anastasios Georgoulas, Nicolas Miché, Cedric Rouaud, and Marco Marengo. Novel battery thermal management system for electric vehicles with a loop heat pipe and graphite sheet inserts. *Applied Thermal Engineering*, 194:117061, 2021.

[154] MB Shafii, A Faghri, and Yuwen Zhang. Analysis of heat transfer in unlooped and looped pulsating heat pipes. *International Journal of Numerical Methods for Heat & Fluid Flow*, 2002.

[155] Durga Bastakoti, Hongna Zhang, Da Li, Weihua Cai, and Fengchen Li. An overview on the developing trend of pulsating heat pipe and its performance. *Applied Thermal Engineering*, 141:305–332, 2018.

[156] Jiansheng Wang, Yu Pan, and Xueling Liu. Investigation on start-up and thermal performance of the single-loop pulsating heat pipe with variable diameter. *International Journal of Heat and Mass Transfer*, 180:121811, 2021.

[157] Latif Aref, Rasoul Fallahzadeh, Seyed Reza Shabanian, and Mojtaba Hosseinzadeh. A novel dual-diameter closed-loop pulsating heat pipe for a flat plate solar collector. *Energy*, 230:120751, 2021.

[158] Jian Qu, Xiaojun Li, Yingying Cui, and Qian Wang. Design and experimental study on a hybrid flexible oscillating heat pipe. *International Journal of Heat and Mass Transfer*, 107:640–645, 2017.

[159] Chuljae Jung, Jonghyun Lim, and Sung Jin Kim. Fabrication and evaluation of a high-performance flexible pulsating heat pipe hermetically sealed with metal. *International Journal of Heat and Mass Transfer*, 149:119180, 2020.

[160] Jonghyun Lim and Sung Jin Kim. A channel layout of a micro pulsating heat pipe for an excessively localized heating condition. *Applied Thermal Engineering*, 196:117266, 2021.

[161] Manfred Groll and S Khandekar. Pulsating heat pipes: a challenge and still unsolved problem in heat pipe science. *Archives of Thermodynamics*, 23(4):17–28, 2002.

[162] Wookyoung Kim and Sung Jin Kim. Fundamental issues and technical problems about pulsating heat pipes. *Journal of Heat Transfer*, 2021.

[163] Yuwen Zhang and Amir Faghri. Advances and unsolved issues in pulsating heat pipes. *Heat transfer engineering*, 29(1):20–44, 2008.

[164] Zichen Zhang, Jiaxiang Zhang, Jiayu Xu, Khai DT Ngo, Guo-Quan Lu, Emily Cousineau, Paul Paret, and Sreekant Narumanchi. Packaging of an 8-kv silicon carbide diode module with double-side cooling and sintered-silver joints. In *2021 IEEE Electric Ship Technologies Symposium (ESTS)*, pages 1–7. IEEE, 2021.

[165] HB Ma, MA Hanlon, and Chung-Lung Chen. An investigation of oscillating motions in a miniature pulsating heat pipe. *Microfluidics and Nanofluidics*, 2(2):171–179, 2006.

[166] Hongbin Ma. *Oscillating heat pipes*. Springer, 2015.

[167] Wei Qu and HB Ma. Theoretical analysis of startup of a pulsating heat pipe. *International Journal of Heat and Mass Transfer*, 50(11-12):2309–2316, 2007.

[168] M Hosoda, S Nishio, and R Shirakashi. Meandering closed loop pulsating heat transport tube. In *Proceeding of 5th ASME/JSME Thermal Engineering Joint Conference*, 1999.

[169] Peter A Kew and Keith Cornwell. Correlations for the prediction of boiling heat transfer in small-diameter channels. *Applied Thermal Engineering*, 17(8-10):705–715, 1997.

[170] Oguzhan Der, Ali Ahmed Alqahtani, Marco Marengo, and Volfango Bertola. Characterization of polypropylene pulsating heat stripes: Effects of orientation, heat transfer fluid, and loop geometry. *Applied Thermal Engineering*, 184:116304, 2021.

[171] Niti Kammuang-Lue, Phrut Sakulchangsatjatai, Pradit Terdtoon, and D Joseph Mook. Correlation to predict the maximum heat flux of a vertical closed-loop pulsating heat pipe. *Heat Transfer Engineering*, 30(12):961–972, 2009.

[172] Frank P Incropera, Adrienne S Lavine, Theodore L Bergman, and David P DeWitt. *Fundamentals of heat and mass transfer*. Wiley, 2007.

[173] AA Tawfek. Heat transfer and pressure distributions of an impinging jet on a flat surface. *Heat and Mass Transfer*, 32(1-2):49–54, 1996.

[174] Yuan-Yang Li, Yan-Jun Chen, and Zhen-Hua Liu. Correlations for boiling heat transfer characteristics of high-velocity circular jet impingement on the nano-characteristic stagnation zone. *International Journal of Heat and Mass Transfer*, 72:177–185, 2014.

[175] W Minkina and D Klecha. Atmospheric transmission coefficient modelling in the infrared for thermovision measurements. *Journal of Sensors and Sensor Systems*, 5(1):17, 2016.

[176] SG Bankoff. Entrapment of gas in the spreading of a liquid over a rough surface. *AIChE journal*, 4(1):24–26, 1958.

[177] BB Mikic, WM Rohsenow, and P Griffith. On bubble growth rates. *International Journal of Heat and Mass Transfer*, 13(4):657–666, 1970.

[178] Peter Griffith and John D Wallis. The role of surface conditions in nucleate boiling. Technical report, Cambridge, Mass.: Massachusetts Institute of Technology, Division of . . . , 1958.

[179] W Fritz and W Ende. Maximum volume of vapor bubbles, phys, 1936.

[180] LI Maltsev, Yu S Podzharov, and OA Kabov. Dry spot growth criterion for isothermal liquid films on a horizontal substrate. *Thermophysics and Aeromechanics*, 24(3):383–387, 2017.

[181] Frederick F Simon and Yih-Yun Hsu. *Thermocapillary induced breakdown of a falling liquid film*. National Aeronautics and Space Administration, 1970.

[182] Veniamin G Levich. Physicochemical hydrodynamics prentice-hall. *Englewood Cliffs, NJ*, 115, 1962.

[183] YY Hsu, JF Lad, and FF Simon. Destruction of a thin liquid film flowing over a heating surface. *Chemical Engineering Progress Symposium Series*, 61(61):139–152, 1965.

[184] Evgeny A Chinnov. Formation of the unsteady thermocapillary structures in the residual layer of three-dimensional waves. *International Journal of Heat and Mass Transfer*, 108:2053–2059, 2017.

[185] Stephen H Davis. Thermocapillary instabilities. *Annual Review of Fluid Mechanics*, 19(1):403–435, 1987.

[186] Dmitrii Valer'evich Zaitsev, Oleg Alexandrovich Kabov, Vyacheslav Vladimirovich Cheverda, and Nikolai Sergeevich Bufetov. The effect of wave formation and wetting angle on the thermocapillary breakdown of a falling liquid film. *High Temperature*, 42(3):450–456, 2004.

[187] V Lel, H Stadler, A Pavlenko, and R Kneer. Evolution of metastable quasi-regular structures in heated wavy liquid films. *Heat and Mass Transfer*, 43(11):1121–1132, 2007.

[188] Herbert Martin Hofmann, Daniela Luminita Movileanu, Matthias Kind, and Holger Martin. Influence of a pulsation on heat transfer and flow structure in submerged impinging jets. *International Journal of Heat and Mass Transfer*, 50(17-18):3638–3648, 2007.

[189] John H Lienhard. Heat transfer by impingement of circular free-surface liquid jets. In *18th National and 7th ISHMT-ASME, Heat and Mass Transfer Conference, Guwahati, India*, 2006.

[190] Xuan Gao, Lingjian Kong, Ri Li, and Jitian Han. Heat transfer of single drop impact on a film flow cooling a hot surface. *International Journal of Heat and Mass Transfer*, 108:1068–1077, 2017.

[191] H Leocadio, CWM Van Der Geld, and Júlio C Passos. Rewetting and boiling in jet impingement on high temperature steel surface. *Physics of Fluids*, 30(12):122102, 2018.